Studying the Effects of Siloxanes on Solid Oxide Fuel Cell Performance

by

Milica Zivak

Submitted in Partial Fulfillment of the Requirements

for the Degree of

Master of Science

in the

Chemistry

Program

YOUNGSTOWN STATE UNIVERSITY

May 2020

Studying the Effects of Siloxanes on Solid Oxide Fuel Cell Performance

Milica Zivak

I hereby release this thesis to the public. I understand that this thesis will be made available from the OhioLINK ETD Center and the Maag Library Circulation Desk for public access. I also authorize the University or other individuals to make copies of this thesis as needed for scholarly research.

Signature:

Milica Zivak, Student Date

Approvals:

Dr. Clovis A. Linkous, Thesis Advisor Date

Dr. Allen D. Hunter, Committee Member Date

Dr. Brian D. Leskiw, Committee Member Date

Dr. Salvatore A. Sanders, Dean of Graduate Studies Date

ABSTRACT

Solid oxide fuel cells (SOFCs) are a promising technology for converting landfill gas into electricity, simultaneously providing a renewable source of energy. However, the contaminants present in landfill gas pose an obstacle to using it for energy generation. The research objective was to examine the effect siloxanes in landfill gas have on the performance of Ni-YSZ/Hionic™/LSM SOFCs, particularly through silica deposition on the Ni-YSZ anode. This was accomplished with voltammetric experiments using the ProboStat™ and anode surface analysis using scanning electron microscopy (SEM) and energy-dispersive X-ray spectroscopy (EDS).

To establish whether siloxanes can be detrimental to SOFC operation, hydrogen spiked with varying concentrations of decamethylcyclopentasiloxane (D5), a representative siloxane, was used as a fuel gas. Compared to operation under pure H_2, which reliably gives a steady state output, the cell showed a 10% loss in voltage after 3 hours each at 1 ppmv D5 and 5 ppmv D5. Another cell operated on H_2 gas containing 10 ppmv D5 experienced a 13% loss in voltage output after 6 hours, and SEM/EDS analysis showed the presence of silica deposits on the cell anodes. This was viewed as water generated via electrochemical reaction hydrolyzing siloxanes to silica and poisoning the SOFC anode. However, when humidified methane, a better landfill gas analogue, was spiked with D5, the cell's voltage output was stable, and silica was not detected on the anode; instead D5 was deposited as silica on surfaces inside the ProboStat™. Thus, the necessity of humidifying the hydrocarbon fuel also provided a protection against anode poisoning by siloxanes. Nevertheless, experiments with humidified Mahoning Landfill gas failed to reach the expected voltage and current output. It was not clear from

SEM/EDS analysis what contaminants were responsible for the decreased cell performance; more surface-sensitive techniques are recommended for further studies.

ACKNOWLEDGEMENTS

I would like to thank my advisor, Dr. Clovis Linkous, for the opportunity to work on this project. Thank you so much for your knowledge, guidance, and especially patience. Despite having a large group of research students, you always made time to answer questions and demonstrate lab techniques. I have tremendous appreciation for your level-headedness during the occasional crises I encountered in this project. I think everything that could have gone wrong went wrong at some point, but you got me through it!

This research would have been incredibly difficult to complete without Mr. Raymond Hoff. Thank you everything you've done for me – from showing me how to use the electron microscope to hauling gas tanks from the landfill. Your knowledge of instrumentation is limitless, even more so than your stash of compression fittings and various supplies I've had to borrow!

Thank you, Dr. Allan Hunter and Dr. Brian Leskiw for serving on my thesis committee. Your encouragement and feedback on this project were invaluable.

To the crew at the Mahoning Landfill, thank you for giving me a tour of the energy generation facility and allowing me to collect samples for my research.

Thank you to the entire YSU Chemistry Department. I am grateful for your help and support.

I'd like to thank my friends. To the past and present students in Dr. Linkous's research group – you made long days in the lab not only tolerable but enjoyable. I will miss working with and learning from all of you. Finally, a big thanks to my family, who supported, encouraged, and tolerated me throughout this entire process.

TABLE OF CONTENTS

LIST OF FIGURES

LIST OF TABLES

CHAPTER 1: INTRODUCTION

PART I: Landfill Gas as Renewable Energy

Trends in Global Fossil Fuel Consumption

As the global population continues growing, one of the few certainties the world faces is the increasing need for resources, including food and fuel. Thus far, fossil fuels such as oil, coal, and natural gas have supplied most the world's energy requirements. However, as finite and non-renewable sources of energy, fossil fuels will eventually disappear, and although the timeline for this disappearance is unclear, the need for alternate renewable energy sources is not. With the demand for fossil fuels increasing and the supply diminishing, one solution to the impending energy crisis is research into renewable sources of energy.

According to Höök and Tang, based on data provided by the International Energy Agency (IEA), fossil fuels presently account for approximately 80% of the world's energy sources. A further breakdown shows that natural gas contributes 20.9%, coal contributes 27.2%, and oil contributes 32.8% to the global energy usage.[1] Figure 1.1, taken from the World Energy Council's 2013 survey of world energy resources, further illustrates this reliance on fossil fuels, with projections indicating that fossil fuels will still comprise approximately 76% of global energy sources by 2020.[2]

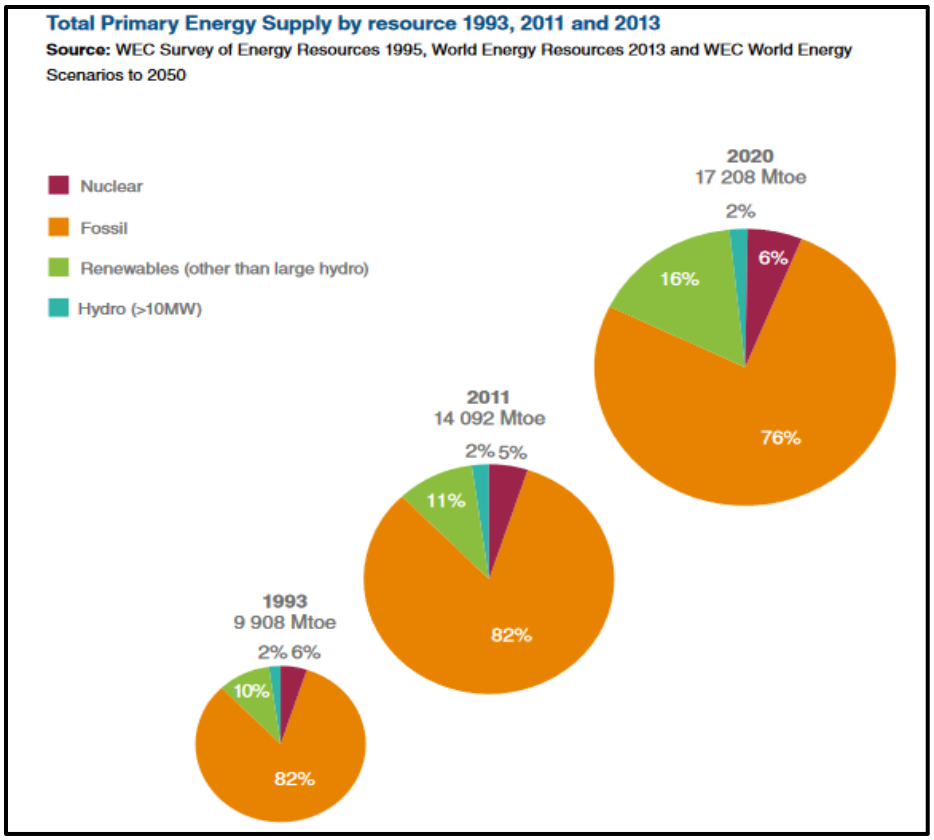

Figure 1.1: Global energy sources, 1993, 2011, and 2020 [2]

Additionally, the Fifth Assessment Report by the Intergovernmental Panel on Climate Change (IPCC) named power generation as the motivating factor behind increasing global fossil fuel usage, with coal accounting for 40.58% and gas accounting for 22.25% of total electricity generation.[3] Figure 1.2, taken from the U.S. Energy Information Administration's (IEA) Monthly Energy Review for August 2019, shows that in 2018, natural gas and coal were still the leading sources of electricity generation in the United States, respectively generating 1,366 and 1,139 billion kilowatthours of electricity.[4]

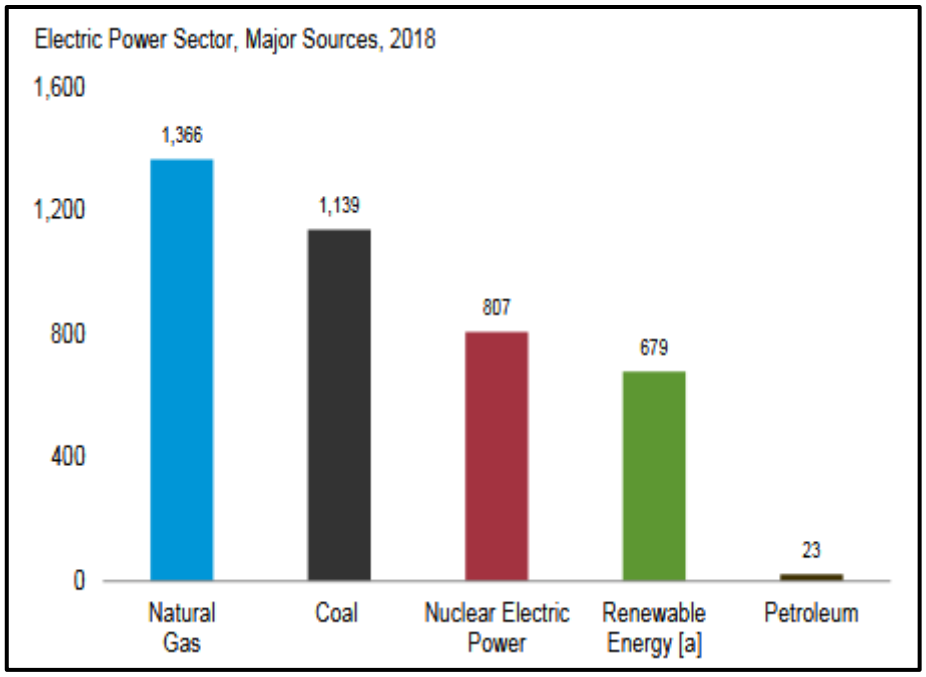

Figure 1.2: Sources of electricity in billions of kilowatthours, U.S. 2016 [4]

In the Fifth Assessment Report, the IPCC emphasized the growing demand for energy, citing a 27% global increase in the total primary energy supply between 2000 and 2010, a figure that the IPCC expects to grow along with the population.[3] Research published by Höök and Tang supported this trend of increasing fossil fuel usage, stating the global use of fossil fuels will double between 2010 and 2040.[1]

If current trends hold, fossil fuels satisfying most of the world's energy requirements guarantees that demand will outpace supply. While fossil fuels need millions of years to form, reports suggest that the global fossil fuel reserves will be exhausted within a century. A study conducted by Shafiee and Topal at the University of Queensland used different models to predict the time remaining until the global reserves of oil, coal, and gas are depleted. One conservative model used the average ratio of consumption to reserves in 2006 to estimate that oil will be depleted in 40 years, coal in 200 years, and gas in 70 years. A model developed by Donald Klass gave these depletion

times as 34, 106, and 36 years.[5] In either case, the supply of fossil fuels is decreasing, while the demand for them is increasing, making our current situation an unsustainable one.

Fossil Fuels and Climate Change

In addition to being non-renewable sources of energy, fossil fuels are destructive to the environment, as they contribute to the greenhouse effect, the process by which gases in the Earth's atmosphere trap solar radiation, increasing the Earth's temperature. Data published by the IEA in 2010 showed fossil fuels contributing to climate change by accounting for 62% of greenhouse gas emissions in the form of carbon dioxide.[1] Furthermore, measurements of atmospheric carbon dioxide at Mauna Loa Observatory in Hawaii indicate a steady increase in atmospheric carbon dioxide concentration, with each year since 2005 marking a new record high value of carbon dioxide in parts per million. Figure 1.3, provided by NASA, illustrates this trend.[6]

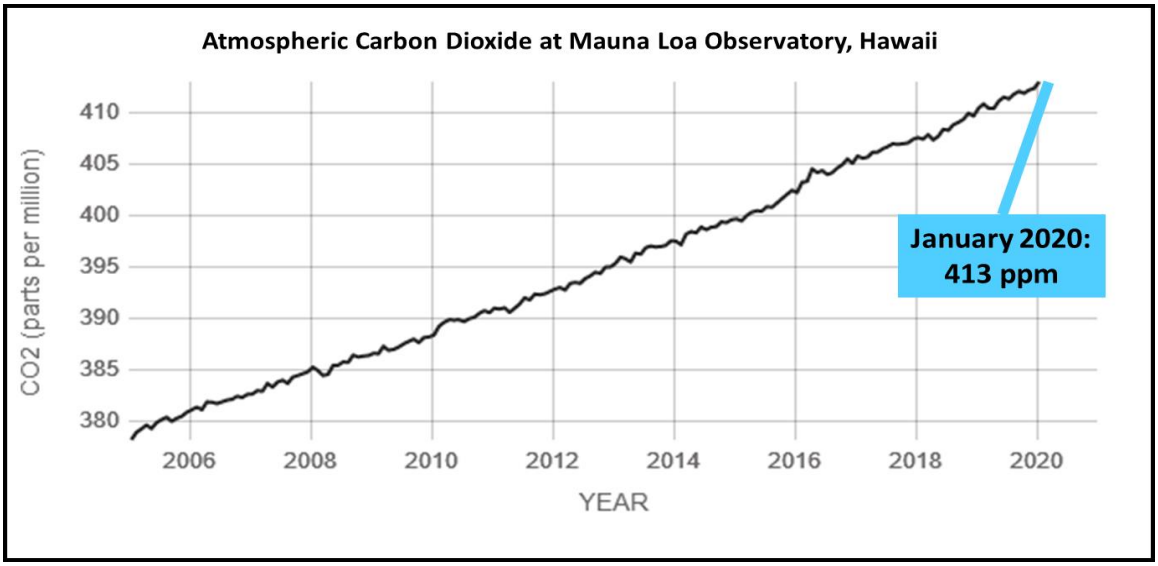

Figure 1.3: Direct measurement of atmospheric carbon dioxide at Mauna Loa, 2005-2020 [6]

An IPCC assessment of climate change in 2013 cited carbon dioxide emissions as a key factor in climate change, leading to increased average global temperatures, rising sea levels, and changes in precipitation patterns. Underscoring the gravity of climate change, this assessment also modelled the probability of extreme climate events, with the likelihood terms "virtually certain" representing 99-100% probability, "very likely" representing 90-100% probability, and "likely" representing 66-100% probability. If current greenhouse gas emission trends continue, higher minimum and maximum temperatures are virtually certain, increases in sea level are likely, and precipitation extremes are very likely by 2100.[7]

Although many factors contribute to climate change, the consumption of fossil fuels by the energy sector is the leading cause of greenhouse gas emissions, producing 49% of greenhouse gases in 2010, a substantial increase from 22% in 1970, per the IPCC's Fifth Assessment Report. Of these emissions by the energy sector, 75% resulted from the production of electricity and heat, a sector that has historically grown along with the Earth's population.[2] Considering the shrinking supply of fossil fuels as well as their damaging effects on the environment, the need for sustainable and cleaner sources of energy is an urgent one.

Landfill Gas: A Greenhouse Gas and a Renewable Energy Source

The research discussed earlier demonstrates the energy sector's overreliance on fossil fuels and the subsequent effects on the environment, with greenhouse gas emissions being a key concern. However, waste generated by agriculture, the food industry, and individual households is also a contributing factor to greenhouse gases in the Earth's atmosphere, according to a paper published by Duerr et al. As this waste

collects in landfills, bacteria digest the organic components in four stages, producing biogas. This biogas, called landfill gas, consists of greenhouse gases such as methane and carbon dioxide.[8] Figure 1.4, taken from the EPA's *Landfill Gas Energy Project Development Handbook*, depicts the four phases of landfill gas synthesis and its typical composition at each phase.[9]

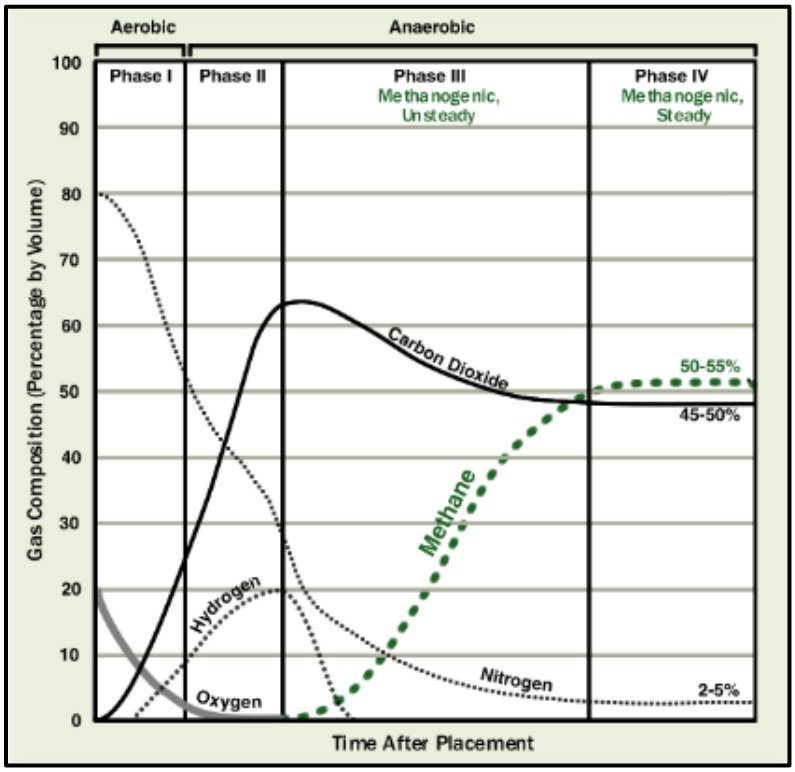

Figure 1.4: Landfill gas composition during the four phases of landfill gas synthesis [9]

During Phase I, aerobic bacteria break down long chains of organic molecules into simpler molecules while consuming oxygen. Carbon dioxide is the primary product of the first phase. Once aerobic bacteria deplete the oxygen present in the landfill, Phase II begins. In the second phase, hydrolysis occurs, in which water molecules further break down carbohydrates, fats, and proteins into simple sugars, fatty acids, and amino acids. This is followed by acidogenesis, in which anaerobic bacteria convert the products of

hydrolysis into volatile fatty acids. As this phase proceeds, the hydrogen and carbon dioxide content of the gas increases. Phase III consists of acetogenesis followed by methanogenesis. During acetogenesis, anaerobic bacteria digest the volatile fatty acids from the previous phase, generating acetic acid, hydrogen, and carbon dioxide. Next, through the process of methanogenesis, methanogenic bacteria consume hydrogen and acetic acid to make methane. During this step, the hydrogen present in the landfill gas is depleted, the carbon dioxide content decreases, and methane becomes the majority component. The overall reaction taking place during the production of landfill gas from organic waste is

$$C_6H_{12}O_6 \rightarrow 3CO_2 + 3CH_4 \quad (1.1)$$

Finally, in Phase IV, the composition of the landfill gas stabilizes, and the gas typically consists of 50-55% methane and 45-50% carbon dioxide. Other trace components that may be found in the sample depend on the type of waste in that landfill.[9]

Once the digestion of organic waste into biogas concludes, the resulting landfill gas is rich in methane. Particularly environmentally harmful, methane traps heat in the Earth's atmosphere 28 to 36 times more effectively than carbon dioxide, according to the United States Environmental Protection Agency (EPA). In addition to its greenhouse activity, an important feature of methane is its energy content. Methane has a heating value of 1,011 Btu/ft^3, which compares favorably to hydrogen's heating value of 325 Btu/ft^3. With methane acting as the main energy source in landfill gas, an ordinary landfill gas sample has a heating value of approximately 500 Btu/ft^3, still surpassing that of hydrogen.[9] While landfill gas is an environmentally harmful waste product, its renewability and energy richness make it an attractive alternative to fossil fuels.

Taking the rate of municipal waste production into account, the abundance of landfill gas makes it an appealing source of energy. In 2013, per EPA estimates, the United States created 254 million tons of municipal solid waste. This waste produces 300 cubic feet per minute of landfill gas, with one million tons of waste having the potential to generate 0.78 megawatts of power.[9] Most landfills collect landfill gas in vertical or horizontal wells, use a blower to draw the gas into a flare, and finally dispose of the gas by burning it. Figure 1.5, taken from a U.S. Army Corps of Engineers manual, shows an example of a system for capturing and burning landfill gas.[10]

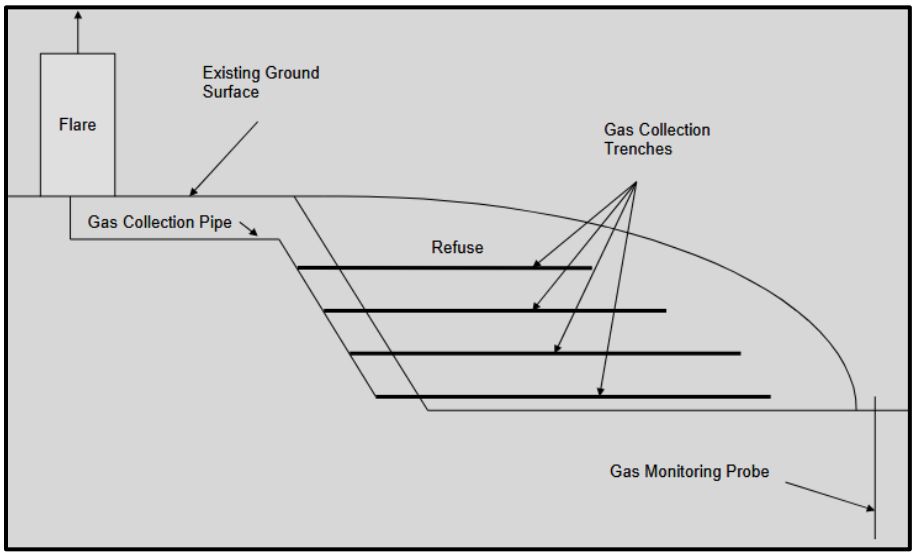

Figure 1.5: Landfill gas collection system using horizontal extraction wells [10]

However, seeing its utility, landfills began collecting landfill gas to use as fuel in the 1970s. After collection using extraction wells, landfills treat the gas to remove impurities before feeding it into an energy recovery system.[9]

Once the landfill gas is collected and treated, there are several methods of converting landfill gas to electrical and thermal energy. Outlined in the EPA's Landfill Gas Energy Project Development Handbook, these methods range from using landfill gas

to power internal combustion engines and turbines, to the direct use of landfill gas in boilers and furnaces. Comprising approximately 75% of electricity-generating landfill gas projects, internal combustion engines are presently the most common method of obtaining energy from landfill gas. Because they are relatively inexpensive to implement and efficiently convert 30% to 40% of landfill gas into electricity, internal combustion engines are more popular than turbines. Despite these benefits, some disadvantages of internal combustion engines include high emissions and substantial maintenance costs. On the other hand, gas turbines and microturbines convert landfill gas into electricity, but with the advantage of decreased emissions of nitrogen oxides. However, as with internal combustion engines, maintenance costs and the need to extensively pretreat landfill gas before it is fed into these systems are substantial drawbacks.[9]

More recent research looks at fuel cells as a method for harnessing landfill gas's energy potential. A 2007 paper by Duerr et al. proposed the use of an alkaline fuel cell with a lead acid battery to convert landfill gas to energy, theoretically yielding 545.2 MWhs of electricity annually. The authors of the study also acknowledged the downsides of this system, citing the need to reform methane into hydrogen gas and the high startup and maintenance costs required.[8] Another paper published by Milewski and Lewandowski in the *Archives of Thermodynamics* examined the use of solid oxide fuel cells for the same purpose, praising them as safe, efficient, and relatively inexpensive to operate, especially compared to counterparts that operate at lower temperatures.[11]

Solid Oxide Fuel Cells

Solid oxide fuel cells (SOFCs) convert chemical energy into electricity through the flow of electrons from the anode to the cathode of the fuel cell. The main characteristic differentiating SOFCs from traditional fuel cells is that all the components of the cell exist in the solid state. A review of SOFCs written by Prakash et al. in 2014 described the three main components of SOFCs: the cathode, electrolyte, and anode. In modern SOFCs, the cathode is commonly made of lanthanum manganite doped with strontium (LSM). The most common electrolyte used in these cells is yttria-stabilized zirconia (YSZ),[12] though Fuel Cell Materials has developed a Hionic™ substrate, which combines YSZ and scandia-stabilized zirconia (ScSZ) and boasts better mechanical strength and conductivity than either electrolyte material on its own.[13] Finally, because of their properties, composites of ceramic and metallic materials (cermets) make up modern anodes. Nickel-YSZ (Ni-YSZ) cermet anodes, made of nickel (II) oxide mixed with YSZ, are particularly popular due to their stability, nonreactivity, and high electronic conductivity.

This same review identified the numerous advantages of SOFCs, especially when they are compared to more traditional methods of electricity generation.[12] Unlike combustion engines, which are limited by the Carnot cycle and achieve a maximum efficiency of approximately 40%,[14] SOFCs convert fuel into electrical energy with 50-60% efficiency. Furthermore, the heat produced by fuel cell operation can be used to power turbines; this co-generation process increases the overall efficiency to upward of 70%. Although SOFCs require an initial energy investment to reach their operating temperatures of 500 to 1000°C, once the fuel cell is running, it is self-sustaining. These

high operating temperatures offer fuel flexibility, allowing for the internal reforming of methane and making the cell able to withstand the presence of many common landfill gas contaminants.[12]

In addition to being more efficient, SOFCs are less harmful to the environment than other technologies for converting landfill gas into electricity. According to the World Energy Council, when landfill gas is burned to generate electricity, pollutants such as NO_x, SO_x, and ammonia are emitted into the atmosphere.[2] Unlike generators based on combustion, SOFCs operating on landfill gas do not release such pollutants into the atmosphere, as the only products of the SOFC reaction are water and carbon dioxide.[12] Because the carbon dioxide produced at the anode is free of contaminants, it can be captured and sequestered, further reducing its environmental impact. Because of their versatility and efficiency, SOFCs are a promising method of converting landfill gas into electrical energy, minimizing the world's reliance on fossil fuels and turning a waste product into a sustainable energy source. According to the EPA, doing so would directly decrease greenhouse gases by converting methane into water and carbon dioxide during the energy production process. Furthermore, it would indirectly decrease greenhouse gases by replacing fossil fuels as energy sources.[9]

Operating SOFCs on Landfill Gas

Landfill gas contains hydrocarbons in the form of methane, which is a fuel source for SOFCs. The review published by Prakash et al. described the general process by which SOFCs convert fuel into electrical energy as a series of three steps. First, oxygen is reduced at the cathode, forming the oxygen anion, as shown in Equation 1.2:

$$O_2 + 4e^- \rightarrow 2O^{2-} \quad (1.2)$$

This anion is then transported across the solid-state electrolyte and into the anode. In the last step of the process, the fuel is oxidized at the anode, producing electrons:

$$2H_2 \rightarrow 4H^+ + 4e^- \quad (1.3)$$

The overall reaction is therefore

$$2H_2 + O_2 \rightarrow 2H_2O \quad (1.4)$$

When methane is used to fuel SOFCs, several reactions occur depending on the conditions. At the cathode, oxygen is reduced to give the oxygen anion:

$$2O_2 + 8e^- \rightarrow 4O^{2-} \quad (1.5)$$

At the anode, the electrochemical half-reactions given in Equations 1.6 through 1.8 occur:

$$CH_4 \rightarrow C + 2H_2 \quad (1.6)$$

$$C + 2O^{2-} \rightarrow CO_2 + 4e^- \quad (1.7)$$

$$2H_2 + 2O^{2-} \rightarrow 2H_2O + 4e^- \quad (1.8)$$

The overall electrochemical reaction taking place at the anode is

$$CH_4 + 4O^{2-} \rightleftarrows CO_2 + 2H_2O + 8e^- \quad (1.9)$$

Combining the cathode and anode reactions gives the overall reaction for a SOFC operated on methane as

$$CH_4 + 2O_2 \rightleftarrows CO_2 + 2H_2O \quad (1.10)$$

The flow of electrons given off by the reactions described above directly generates electricity for our use.[12] Figure 1.6 shows a general schematic of how SOFCs function.

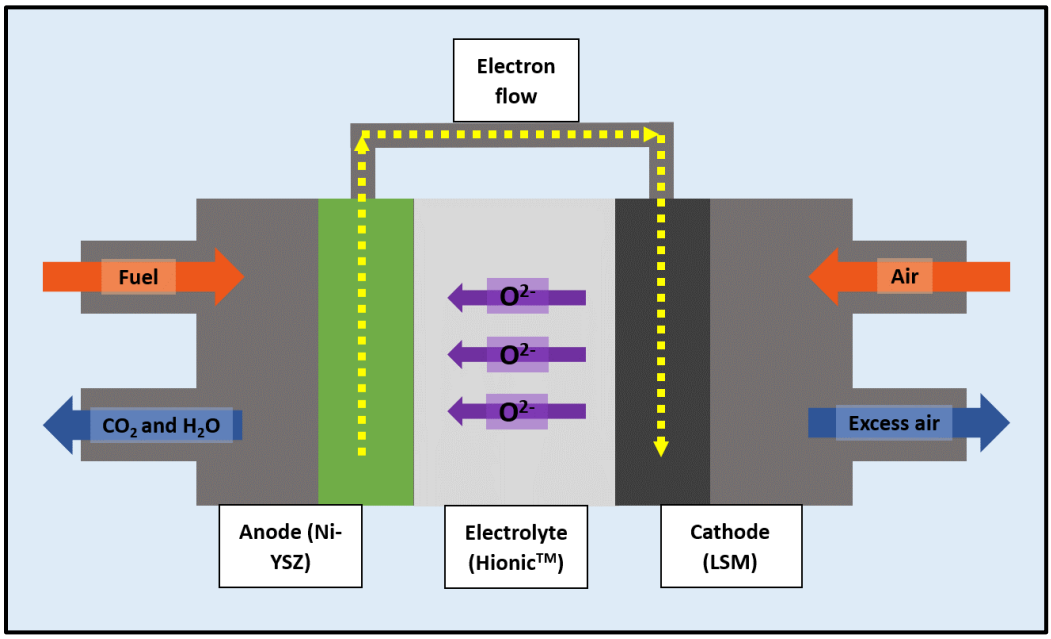

Figure 1.6: SOFC function

Solid oxide fuel cells operated on landfill gas have exciting potential for supplementing energy production and reducing the environmental impact of municipal waste, but several obstacles currently hinder the use of this technology.

Obstacles to Using Landfill Gas in SOFCs

The inefficiencies in solid oxide fuel cell operation primarily arise from the interaction of the fuel gas with the anode. Despite the advantages of using solid oxide fuel cells rather than internal combustion engines for electricity generation from landfill

gas, they share some pitfalls. Both systems are subject to operating losses due to carbon deposition and contaminants present in landfill gas.[14]

Carbon Deposition

In their comprehensive review of the current state of Ni-YSZ-based SOFCs, Prakash et al. described the process of anode inactivation through carbon deposition.[12] Carbon deposition, or coking, results from the incomplete combustion of hydrocarbon fuels. The pyrolytic decomposition of methane results in coking through the following reaction:

$$CH_4 \rightarrow 2H_2 + C_{(s)} \quad (1.11)$$

One approach to overcoming the issues of carbon deposition is the development of hardier anode materials. A paper by Kan et al. studied the effect of the anode's composition on carbon deposition by doping a Ni-YSZ anode with tin. Using methane as the fuel, Kan et al. measured the power densities of a Ni-YSZ cell and a Sn-doped Ni-YSZ cell over time, finding that the Ni-YSZ cell lost function after 2.3 hours, while the Sn-doped Ni-YSZ cell continued to function for 49.0 hours, showing improved stability compared to the Ni-YSZ cell.[15] These results suggest that experimenting with different anode compositions is a feasible method of combatting carbon deposition.

Until suitable anode materials are discovered, the current methods for avoiding carbon deposition involve pretreating the landfill gas before using it as fuel. For example, humidifying the fuel gas before feeding it into the fuel cell mitigates the issue of carbon deposition.[12] When methane is reformed with steam, the reaction proceeds as

$$CH_4 + H_2O \rightarrow 3H_2 + CO \quad (1.12),$$

avoiding carbon formation. When operating SOFCs on methane, the fuel gas can be externally reformed with steam, where the reaction described by Equation 1.12 occurs before gases enter the anode. Alternately, steam and methane can be simultaneously fed into the anode chamber, and the reforming reaction takes place directly at the anode. This process is called internal reforming.

In 2010, Mermelstein et al. published a study in the *Journal of Power Sources* that examined the effect of steam on carbon formation at Ni-YSZ anodes. Mermelstein et al. pumped steam across a Ni-YSZ anode, using polarization resistance to monitor anode performance. They found that increasing steam concentration decreased the polarization resistance of the anode, meaning that the presence of steam reduced the degradation of the cell. This study demonstrated that humidifying fuel gases prevents carbon deposition without impairing fuel cell performance.[16]

Sulfide Poisoning

Anode inactivation through sulfide poisoning remains a more difficult problem to solve than carbon deposition. In his research at Youngstown State University, Dr. Feroze Khan examined the effect of hydrogen sulfide on fuel cell operation and studied the efficacy of flowing hydrogen gas through the fuel cell to reverse sulfide poisoning. Khan fed hydrogen sulfide gas into a Ni-YSZ/LSM fuel cell and demonstrated that the cell suffered a decrease in voltage in the presence of hydrogen sulfide in concentrations of 5 ppm.[17] This presents a problem, as actual landfill gas contains hydrogen sulfide in concentrations ranging between 50 ppm and several hundred ppm.[18] Khan also found that

sulfide poisoning could be reversed by introducing a flow of hydrogen gas into the cell, but because this required 13% to 19% hydrogen gas at hydrogen sulfide concentrations of 5 ppm, this method is inefficient.[17] As with carbon deposition, new anode materials are being studied as a means of eliminating anode passivation,[12] but currently, pretreatment of landfill gas to remove hydrogen sulfide is the main method for avoiding sulfide poisoning.

Hydrogen sulfide, although especially harmful to SOFC performance, is not the only component of landfill gas that can cause problems for a Ni-YSZ anode. A typical sample of landfill gas contains only trace amounts of contaminants, making up less than 1% of the total composition.[19] However, as studies of hydrogen sulfide have shown, amounts of certain contaminants at the part per million level are capable of inactivating solid oxide fuel cells. The exact composition of a landfill gas sample will depend on the landfill from which it is collected, with factors such as the types of waste and the moisture content of the landfill determining the compounds present in the landfill gas sample.[18] Common landfill gas contaminants of concern include volatile organic compounds, such as chlorine compounds, sulfur compounds, and siloxanes.[19]

Siloxane Poisoning

Siloxanes are organosilicon compounds that, after sulfur compounds, represent the next largest family of impurities found in landfill gas. Because they are commonly used in cosmetics and detergents, siloxanes are abundant in municipal landfills.[20] As they are oxidized, siloxanes form silica (silicon dioxide) microparticles on the surface of the anode, eventually causing the fuel cell to fail. The reactions responsible for silica

formation under solid oxide fuel cell operating conditions are given in Equations 1.13 and 1.14:

$$[SiO(CH_3)_2]_{n\,(g)} + 5n\ H_2O \rightarrow n\ Si(OH)_{4\,(g)} + 2n\ CO + 6n\ H_2 \qquad (1.13)$$

$$Si(OH)_{4\,(g)} \rightarrow SiO_{2\,(s)} + 2H_2O \qquad (1.14)$$

In the reaction given by Equation 1.13, a volatile siloxane expressed as $[SiO(CH_3)_2]_n$, where n describes the number of silicon atoms present in the compound, degrades in the presence of water to form gaseous silicon hydroxide, carbon monoxide, and hydrogen gas. This is followed by the reaction shown in Equation 1.14, in which the dehydration of one equivalent of silicon hydroxide, also called silicic acid, results in the formation of one equivalent of solid silica and two equivalents of water.[21] Figure 1.7 shows silica deposits on the piston of a combustion engine that was operated on landfill gas.[22]

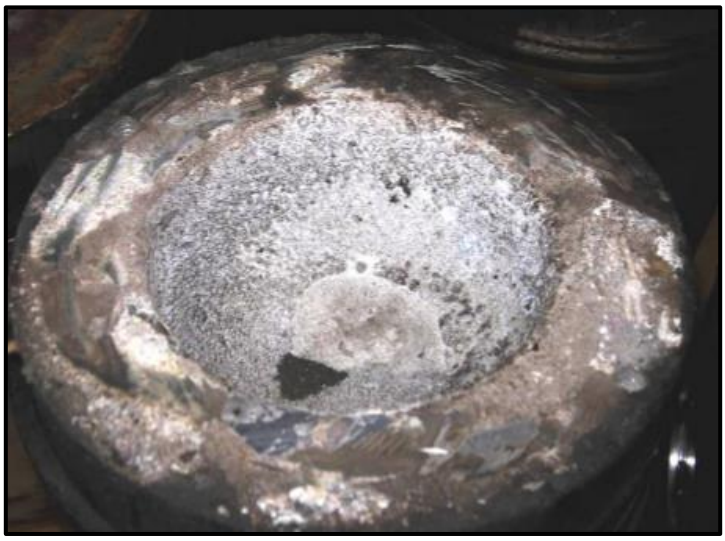

Figure 1.7: Silica buildup on the piston of a landfill gas engine [22]

As with hydrogen sulfide, the presence of siloxane in landfill gas results in the formation of a compound on the anode surface, causing cell inactivation over time. However, unlike hydrogen sulfide poisoning, anode inactivation through silica deposition is irreversible. This makes the removal of siloxanes from landfill gas critical to SOFC function.

When seeking to remove siloxanes from landfill gas on a large scale, it is necessary to consider both the efficacy of the method and its environmental and economic impact. A review by Soreanu et al. compares various methods based on siloxane removal efficiency and operating cost. For example, siloxane removal by refrigeration and condensation can remove up to 95% of siloxanes in a gas sample without using toxic reagents. However, the need for specialty equipment, the required cleaning and maintenance of the equipment, and the energy required to operate it make this method less attractive than conventional absorption and adsorption methods.[23]

Absorption and adsorption techniques involve using either liquid or solid materials to strip siloxanes from landfill gas. One method, described by Kazimierz Gaj, involves the physical absorption of siloxane by organic solvents. Depending on the solvent used, siloxane removal can be very effective; Selexol, a proprietary propylene glycol dimethyl ether, can remove up to 99% of siloxanes in a gas sample. While this method is appealing, Gaj explains that its efficiency fluctuates with changes in temperature and the amount of siloxanes present in the sample.[24] Additional disadvantages are the price of proprietary solvents and their impact on the environment.[23] Liquids, such as strong acids, that chemically absorb siloxanes eliminate the possibility of

desorption that physical absorbents carry, but they are also bad for the environment and dangerous to handle.[24]

Siloxane adsorption on solid materials is a physical process, and its ability to remove siloxanes from landfill gas depends on the material used. Solid adsorbents have several advantages over the liquid absorbents previously mentioned. Unlike organic solvents and strong acids, the solid adsorbents used for siloxane removal tend to safer to handle and less harmful to the environment. Additionally, they can be easily regenerated and reused. A study by Sigot et al. compared the octamethylcyclotetrasiloxane (D4) removing capacity of three solid adsorbents: activated carbon, zeolite, and silica gel. The reported technique compared the amount of D4 removed by each adsorbent by measuring the milligrams of D4 adsorbed per gram of adsorbent. The silica gel proved to be the most effective adsorbent, capturing twice as much D4 as zeolite and approximately four times as much D4 as activated carbon by mass.[25] The review by Soreanu et al. cites the siloxane removal efficiency of solid adsorbents as 90-99%.[23] Like other siloxane removal methods, the use of solid adsorbents has disadvantages. An adsorbent can only hold a certain quantity of siloxanes before it begins to lose efficacy, making it necessary to frequently regenerate and replace the material. Also, adsorbents such as silica gel will also adsorb water, so the adsorbent would need to be placed before the humidification system in the landfill gas pretreatment apparatus.

Mahoning Landfill

The Mahoning Landfill in New Springfield, Ohio is a municipal solid waste landfill operated by Waste Management Inc. According to the Landfill Methane Outreach Program's July 2019 report, as of 2017, the Mahoning Landfill had 6.8 million tons of

solid waste in place, generating 1.658 million standard cubic feet of landfill gas per day. Previously, the Mahoning Landfill disposed of the collected gas by flaring it into the atmosphere, but in 2013, Waste Management Renewable Energy, LLC launched a project utilizing landfill gas for electricity generation. Collected gas is piped into the on-site Mahoning Landfill Gas to Energy Facility, shown in Figure 1.8, where five generators powered by CAT 3516 reciprocating piston engines produce 4 megawatts of electricity.[26] The electricity generated at the Mahoning Landfill is sold to the city of Oberlin, accounting for 25% of Oberlin's energy sources.[27]

Figure 1.8: The Mahoning Landfill Gas to Energy Facility for on-site electricity generation

As previously discussed, the landfill gas must be pretreated prior to its use in combustion engines such as those at the Mahoning Landfill. On-site engineers at the Mahoning Landfill explained that the gas is compressed, filtered, and dehumidified before it is fed into the engines. The Mahoning Landfill is not required to measure the

siloxane content of its landfill gas and was therefore unable to provide such data. However, engineers indicated the presence of siloxanes in the gas feed contributes to the need for equipment maintenance. While some siloxanes are removed through condensation during the dehumidification process, the heavier siloxanes that remain in the gas lead to silica deposition inside the engines. Every six months, the engines are shut off for cleaning, including sandblasting to remove deposited silica. Figure 1.9 shows a gray deposit on a spark plug from one of the CAT engines, kindly provided by the Mahoning Landfill.

Figure 1.9: CAT 3516 reciprocating engine spark plug with a gray deposit

When the Mahoning Landfill Gas to Energy Facility is shut down for maintenance, the gas must be flared, as shown in Figure 1.10.

Figure 1.10: When the Gas to Energy Facility is not operating, landfill gas is flared.

PART II: Statement of Purpose

The effects of carbon deposition and hydrogen sulfide poisoning on the Ni-YSZ anode of solid oxide fuel cells have been extensively studied, and methods for minimizing their harm to the anode have been implemented. However, the effects of the other potential contaminants discussed in the previous section have not been as closely examined. Further research in the Linkous research group at Youngstown State University will focus on the effects of siloxanes found in landfill gas samples collected from the Mahoning Landfill in New Springfield, Ohio. The goal of this research is to operate a Ni-YSZ/Hionic™/LSM solid oxide fuel cell on landfill gas from the Mahoning Landfill while examining the effects of siloxanes on the anode material. This research will be accomplished in four stages.

In the first stage, preliminary voltammetric experiments will be used to confirm that the Ni-YSZ/Hionic™/LSM solid oxide fuel cell can be successfully operated on humidified methane, the fuel component of landfill gas. Once a baseline for expected voltage and current output is established, the second stage of research will examine the effect of siloxanes on fuel cell performance. The solid oxide fuel cell will be operated on methane spiked with known concentrations of decamethylcyclopentasiloxane, which will serve as a model siloxane. As with the preliminary voltammetric experiments, the cell's function will be monitored by observing current and voltage output over time. This will demonstrate the effect siloxanes have on cell function.

In the third stage, the voltammetric testing procedure will be repeated using a Mahoning Landfill gas sample rather than methane. As previously discussed, data collected by Feroze Khan confirmed the presence of hydrogen sulfide in landfill gas from the Mahoning Landfill. Based on Khan's data, hydrogen sulfide removal is crucial to cell function. Therefore, landfill gas will be passed through a commercial chemisorbent filter, and colorimetric gas detection tubes will then be used to determine the hydrogen sulfide content of the landfill gas before and after treatment. Ultimately, the goal of this stage of research is to see if the solid oxide fuel cell can be successfully operated on a sample of gas from the Mahoning Landfill.

Once cell performance during each test has substantially decayed, the fourth stage of research involves using surface analysis techniques to determine the distribution and elemental composition of contaminants, mainly silicon compounds, present on the Ni-YSZ anode. This will be accomplished using scanning electron microscopy (SEM) to

compare the anode surface before and after operation. Furthermore, energy-dispersive X-ray spectroscopy (EDS) will be used to determine the presence of silicon on the anode.

CHAPTER 2: MATERIALS, INSTRUMENTATION, AND METHODS

PART I: Initial Voltammetric Experiments on Ni-YSZ/Hionic™/LSM Button Cells

To verify that the cell can give an acceptable current output under laboratory conditions, voltage versus current measurements were made on a Ni-YSZ/Hionic™/LSM button cell operated on hydrogen and then humidified methane. Furthermore, these preliminary experiments were used to confirm that the apparatus and conditions for humidifying the fuel gas successfully prevent carbon deposition.

Button Cell

Button cells consisting of a Ni-YSZ anode, Hionic™ electrolyte, and LSM cathode were purchased from Fuel Cell Materials in Lewis Center, Ohio. The most common SOFC electrolyte is YSZ, but Fuel Cell Materials uses their proprietary Hionic™ electrolyte, which is based on scandia-stabilized zirconia. The manufacturer claims the Hionic™ material is four times stronger than YSZ electrolytes and is also more conductive.[13] These button cells get their name from their small size, with the cells used for the voltammetry experiments having a total diameter of 20 mm. The cathode and anode diameter is 12.5 mm, for an active electrode area of approximately 1.23 cm^2. Figure 2.1 is a diagram showing the construction of a Ni-YSZ/Hionic™/LSM button cell.

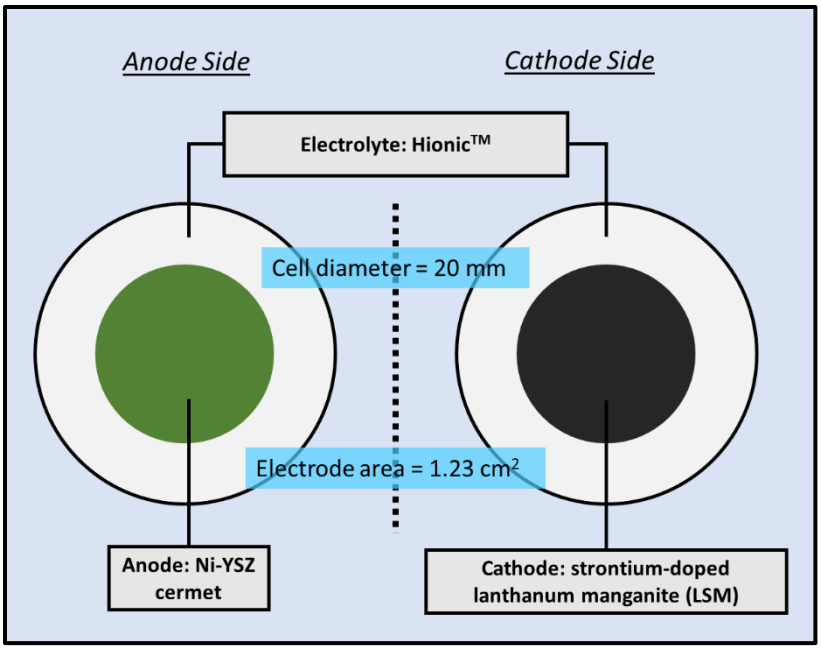

Figure 2.1: Diagram of a 20 mm NextCell button cell

ProboStat™

Voltammetric experiments on the button cell were performed using the ProboStat™, an instrument manufactured by Norwegian Electro Ceramics AS and purchased from Fuel Cell Materials. This versatile instrument can measure numerous electrical properties, but for this experiment, it was configured to measure voltage and current. The ProboStat™ consists of an outer alumina tube that closes the system off from the atmosphere and an inner alumina tube on which the button cell is cemented. Inside the inner alumina tube is the inner gas flow tube, which delivers air to the cathode of the button cell. An inner platinum contact is placed between the top of the inner gas tube and the cathode of the button cell. The outer alumina tube contains an outer platinum contact that rests on the anode of the button cell and an outer gas tube that delivers the fuel gas to the anode. The inner and outer alumina tubes are screwed onto the base of the

ProboStat™ and sealed with O-rings. A support assembly consisting of an alumina plate and three spring-loaded rods is placed over the outer platinum contact, ensuring that it is secured to the button cell. Figure 2.2 shows a diagram of the ProboStat™.

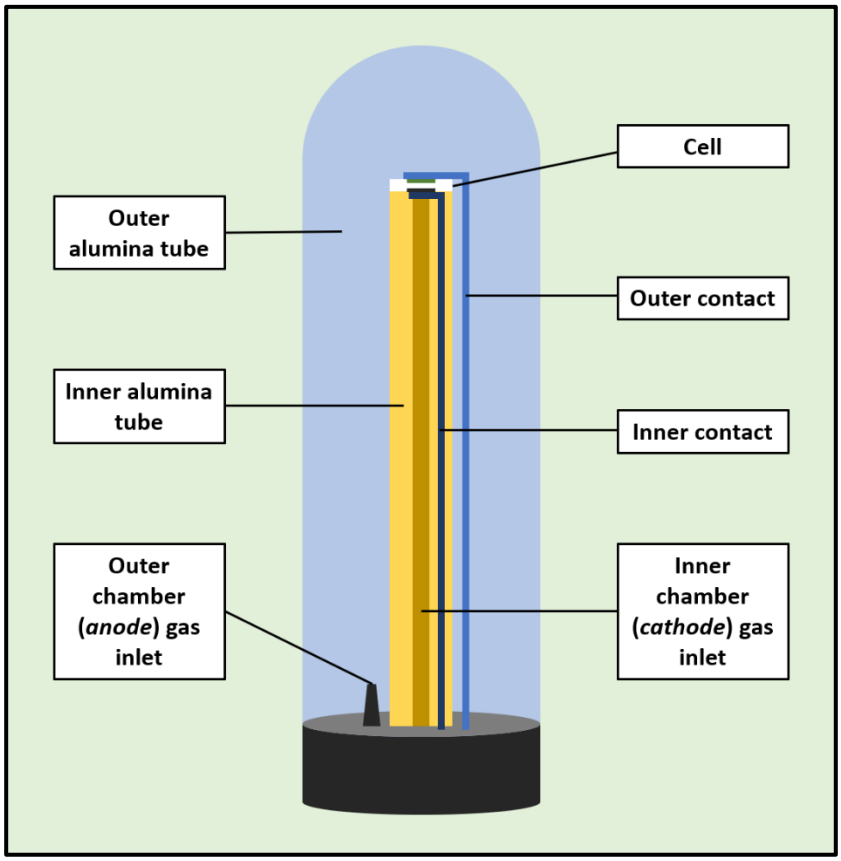

Figure 2.2: ProboStat™ schematic

The button cell was affixed to the inner alumina tube of the ProboStat™ using a thin layer of Ceramabond 552-VFG, a high-temperature ceramic cement made by Aremco Products, Inc. The Ceramabond was air dried for 4 hours, and at this stage, the ProboStat™ was fully assembled and the bonding process completed in a vertical tube furnace. The assembled instrument was heated at 93°C for 2 hours and at 260°C for another two hours, per the manufacturer's instructions for curing Ceramabond.[28] Figure 2.3 is a photograph of a button cell secured to the ProboStat™.

Figure 2.3: Button cell affixed to inner alumina tube of ProbStat

The ProboStat™ has 6 BNC contacts and 16 electrical/thermocouple feedthroughs. The inner general purpose 2-wire platinum contact was placed on feedthrough pins 3 and 4, and the outer contact was placed on feedthrough pins 13 and 15, as shown in the wiring diagram in Figure 2.4, taken from the ProboStat™ manual.[29] These feedthrough pins correspond to the inner low voltage (ILV) and high voltage (HV) BNC sockets on the base of the ProboStat™. BNC coaxial cables were connected to the ILV and HV sockets, joining the ProboStat™ to a circuit including a load box, ammeter set up in series, and voltmeter set up in parallel. Figure 2.5 shows the circuit diagram for this apparatus.

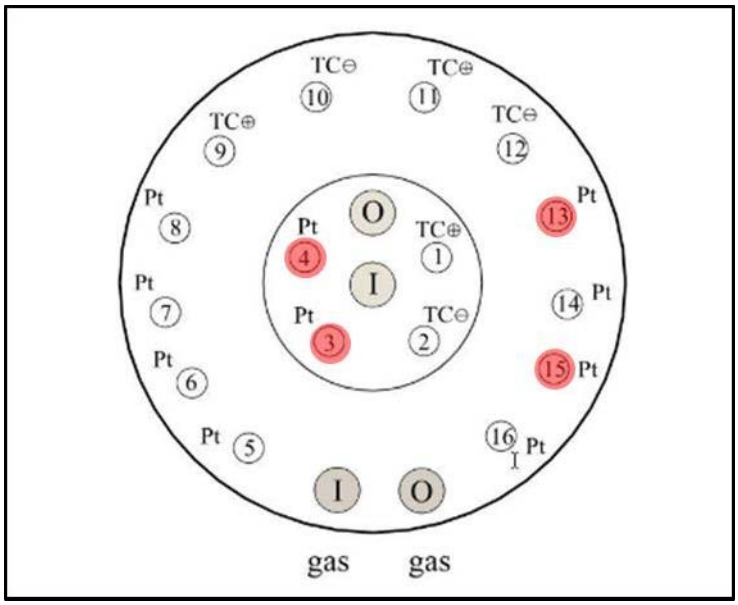

Figure 2.4: Top view of the ProboStat™ wiring diagram, with feedthroughs highlighted

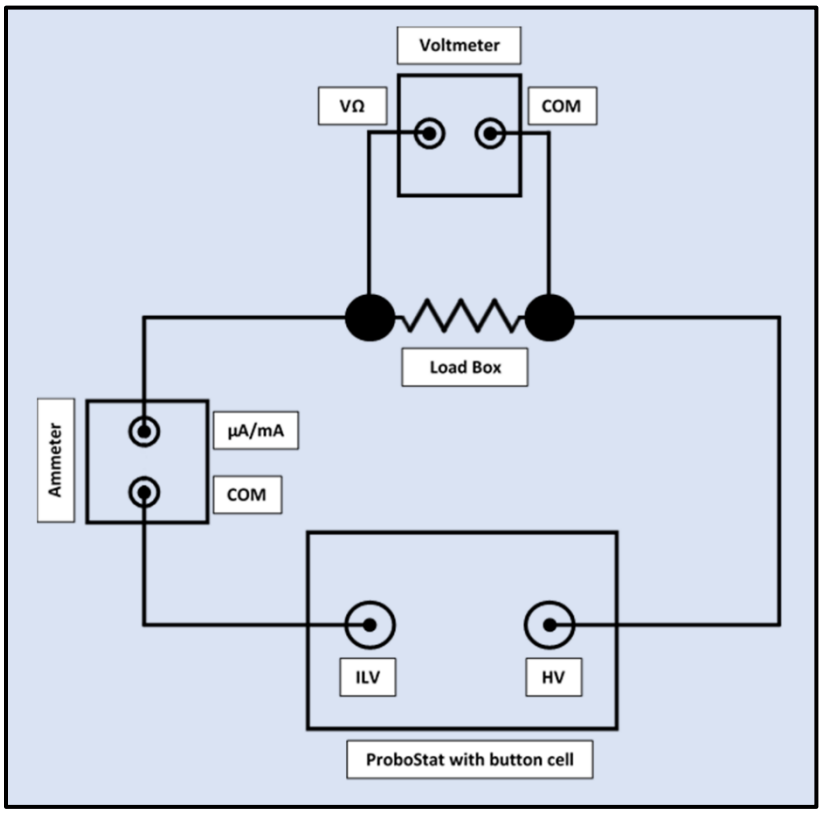

Figure 2.5: Circuit diagram for current-voltage measurements of button cell operated on hydrogen or humidified methane

The base of the ProboStat™ has four Swagelok quick-connect gas connections, two which serve as the gas inlet and outlet for the cathode chamber (inner alumina tube), and two which serve as the gas inlet and outlet for the anode chamber (outer alumina tube). After the ProboStat™ assembly was heated to the desired operating temperature in the vertical tube furnace, these quick-connects were used to feed hydrogen or humidified methane to the anode and air to the cathode of the button cell.

Multimeters

Extech EX430 11-Function True RMS Professional MultiMeters were used to measure voltage and current outputs at variable loads.

Mass Flow Controller

Mass flow controllers made by Brooks Instruments were used to deliver gas to the button cell. The flow controllers, calibrated for air, hydrogen, and methane, are capable of accurately dispensing between 5 mL and 100 mL of gas per minute. The flow of air went directly from the mass flow controller into the inlet for the cathode chamber of the ProboStat™, while methane leaving the mass flow controller was passed through a humidification system before entering the inlet for the anode chamber. When hydrogen was used as a fuel instead of methane, it was not necessary to use the humidification assembly.

Fuel Gas Humidification System

To prevent carbon deposition on the anode, hydrocarbon fuels were internally reformed with steam. Methane, and later landfill gas, was pumped through a

humidification assembly prior to being fed into the anode chamber, as previous research conducted by Feroze Khan demonstrated that humidifying the fuel gas prevents carbon deposition on the anode.[17] Controlling the temperature of the water inside the humidification flask controls the partial pressure of water vapor, which is used to select the desired humidification level. Khan's research showed that a humidification level greater than 50% prevented carbon deposition,[17] so based on his data, a humidification level of approximately 67% was selected for this experiment. This was accomplished by heating the water in the humidification flask to 89°C, for a vapor pressure of 506 torr.[30] Heating tape set to 120°C was wrapped around the tubing delivering the fuel gas from the humidification flask to the anode gas inlet of the ProboStat™, preventing water vapor from condensing before it reaches the anode. Figure 2.6 is a photograph of the apparatus for performing voltammetric tests on the button cell, with the humidification assembly shown.

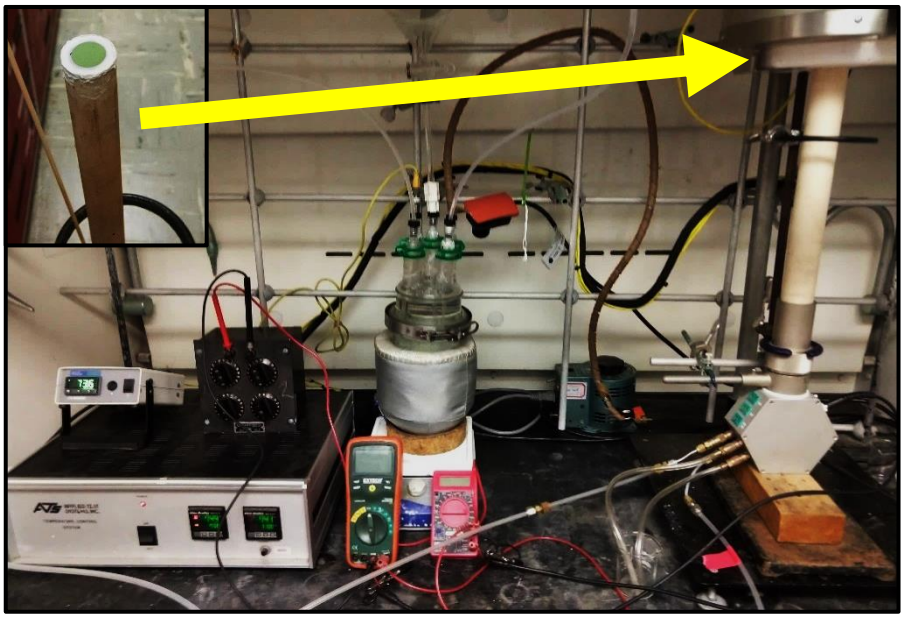

Figure 2.6: Button cell assembly with load box, multimeters, humidification system, and tube furnace

Fuel Cell Operation

The system was purged with nitrogen gas, and the cell was operated on hydrogen and then on humidified methane. Hydrogen was fed into the anode at a rate of 100 mL/min, and air was fed into the cathode at a rate of 50 mL/min. While air only contains approximately 20% oxygen, it was not necessary to use an airflow five times that of hydrogen to maintain the 2:1 stochiometric ratio of hydrogen to air; this is because the button cell utilizes a very small percentage of fuel gas. When humidified methane was used as the fuel, methane was fed into the anode at a rate of 50 mL/min, and air was fed into the cathode at a rate of 100 mL/min. The load box was used to vary the resistance at increments, and the resulting voltage was plotted against the current at each increment. The experiment was performed at temperatures of 750°C, 800°C, 850°C, and 900°C.

PART II: Voltammetric Experiments on Ni-YSZ/Hionic™/LSM Button Cells Operated on Humidified Methane Spiked with Decamethylcyclopentasiloxane

The purpose of this section of experiments was to observe the effect of siloxane buildup on the voltage output of a solid oxide fuel cell. This was accomplished by using a micropump to inject a desired amount of decamethylcyclopentasiloxane (D5) into a stream of humidified methane. This mixture was then fed into the anode of a button cell operating at steady state at 750°C, and voltage measurements were made over time until the cell's output was significantly diminished.

Decamethylcyclopentasiloxane (D5)

Decamethylcyclopentasiloxane, abbreviated as D5, was purchased from ThermoFisher Scientific. This compound was chosen as a representative siloxane because of its prevalence in landfill gas samples and its relative safety compared to similar siloxanes. A presentation given at the EPA's 14th annual Landfill Methane Outreach Program conference stated that D5 was present in 83% of landfill sites. Only octamethylcyclotetrasiloxane (D4) was more prevalent, detected at 90% of landfill sites tested.[31] However, D5 is less flammable than D4 and generally safer to handle, so it was chosen as a model siloxane for examining the effect of siloxanes on SOFC function. Figure 2.7 shows the two-dimensional structure of D5 and its relevant properties.[32]

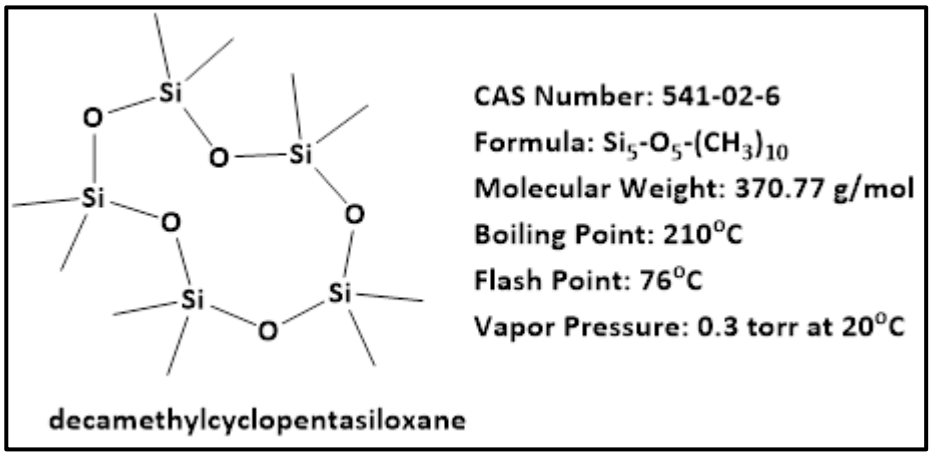

Figure 2.7: Two-dimensional structure and properties of D5 [32]

Syringe Pump

A Cole-Parmer 74900-00 single-syringe infusion pump with a gastight syringe was used to dispense D5 into the humidified methane gas stream. The syringe pump is programmed to inject either a set volume or a set flow rate. For humidified methane that

contains 10 ppmv D5, the methane mass flow controller was set to 50 mL/min, so the desired flow rate of D5 was 0.5 µL/min. This was accomplished by selecting the "Rate" setting of the syringe pump and entering a rate of 30 µL/h.

Fuel Cell Operation

The same general apparatus that was used for the hydrogen and humidified methane tests was also used when operating the button cell on the humidified methane/D5 mixture, but with several modifications. The goal of the experiments described in this section was to see the effect different concentrations of D5 have on the life of the cell, so no attempts were made to remove siloxanes. The complete experimental setup described here is shown in Figure 2.8. The circuit diagram shown in Figure 2.5 remained unchanged.

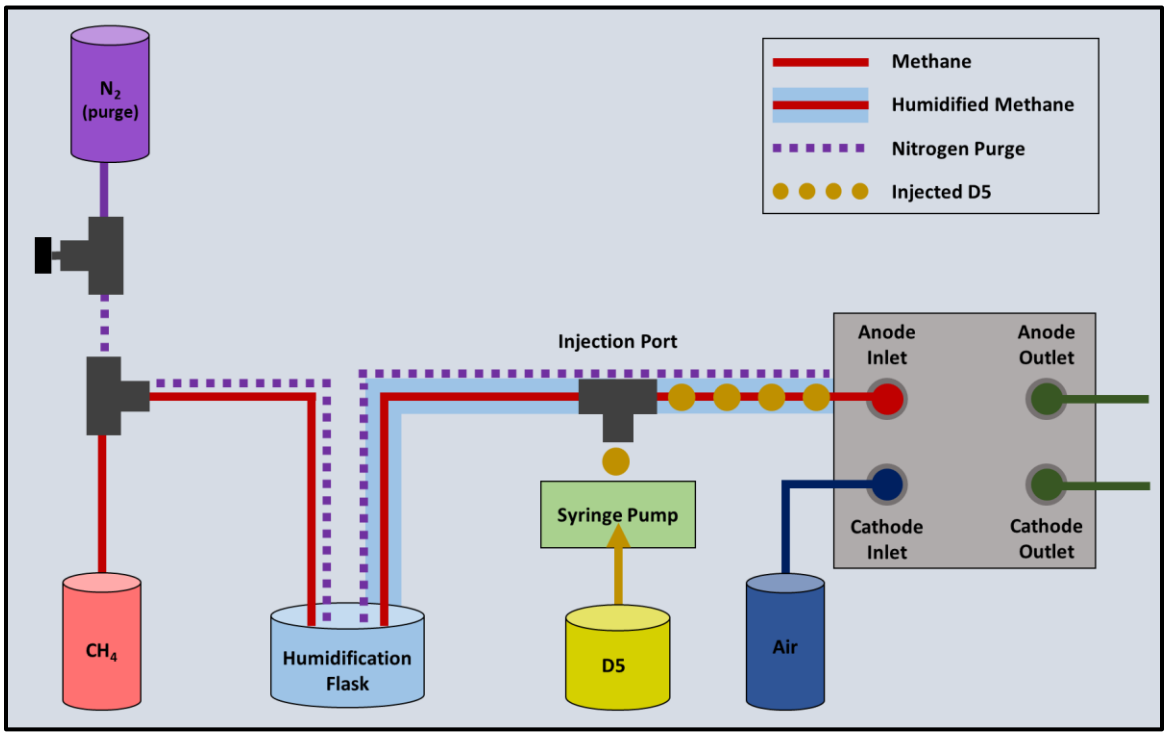

Figure 2.8: Apparatus for operating the button cell on a humidified methane/D5 mixture

X-Ray Diffraction (XRD)

X-ray diffraction (XRD) was used to identify deposits found on the inside of the ProboStat™ after the button cells were operated on D5-spiked gas. XRD analysis was performed using the Bruker AXS X8 Prospector diffractometer, which is found in Youngstown State University's X-Ray Diffraction Laboratory. This instrument uses a copper X-ray source and a sensitive CCD area detector and is capable of analyzing very small and weakly diffracting samples.[33] When X-rays, generated by the instrument's source, strike atoms inside the sample material, they are diffracted according to Bragg's Law. These diffracted X-rays are collected by the detector and create a diffraction pattern. Analyzing the diffraction pattern gives information about the material's crystalline structure and chemical composition.

PART III: Voltammetric Experiments on Ni-YSZ/Hionic™/LSM Button Cells Operated on Mahoning Valley Landfill Gas

As with the button cell operated on hydrogen and humidified methane, voltammetric measurements were used to assess cell function when operated on landfill gas. For these voltammetric and life test experiments, the circuit remained the same as the one shown in Figure 2.5. However, several components for pretreating the gas sample were added to the apparatus.

Mahoning Landfill Gas Sample

Samples of landfill gas were collected on site at the Mahoning Landfill in New Springfield, Ohio. The samples were stored in three 5-gallon propane tanks that were filled using an explosion-proof compressor. The tanks are connected with gas tubing, so their combined volume may be used during an experiment. The tanks are shown in Figure 2.9.

Figure 2.9: Propane cylinders connected with gas tubing contain landfill gas pressurized to 40 psi.

Colorimetric Analysis

Colorimetric gas detection tubes purchased from RAE Systems were used to analyze the hydrogen sulfide content of the Mahoning Landfill gas sample before and after treatment with the chemisorbent filter, giving information about the efficacy of the pretreatment method. These tubes rely on a ligand exchange reaction to quantify the amount of hydrogen sulfide present in the gas sample. Hydrogen sulfide reacts with the white lead acetate in the tube, producing brown to black lead sulfide. The gas detection tube is marked, and the concentration of hydrogen sulfide is read directly from the furthest point of color change along the tube. Corrections for temperature and humidity are then calculated according to the RAE Systems handbook.[34]

Chemisorbent Filter (H_2S Scrubber)

A hydrogen sulfide scrubber that removes H_2S through chemisorption was obtained from Custom Sensors & Technology, a company operating out of Fenton, Missouri. This scrubber contains a proprietary material that changes color from green to black when it is saturated with hydrogen sulfide. To remove hydrogen sulfide from landfill gas, the scrubber was placed between the landfill gas cylinder and the anode gas inlet of the ProboStat™, as shown in Figure 2.10.

Fuel Cell Operation

The same general apparatus that was described in Part II of this chapter was used when operating the button cell on Mahoning Landfill gas, but with several modifications. Because the landfill gas needs to be pretreated to remove hydrogen sulfide, it passes through a chemisorbent filter before entering the anode chamber of the cell. Two sampling ports that can be opened using needle valves are used to measure the hydrogen sulfide content of the landfill gas before (sampling port #1) and after (sampling port #2) it passes through the H_2S scrubber. The complete experimental setup described here is shown in Figure 2.10.

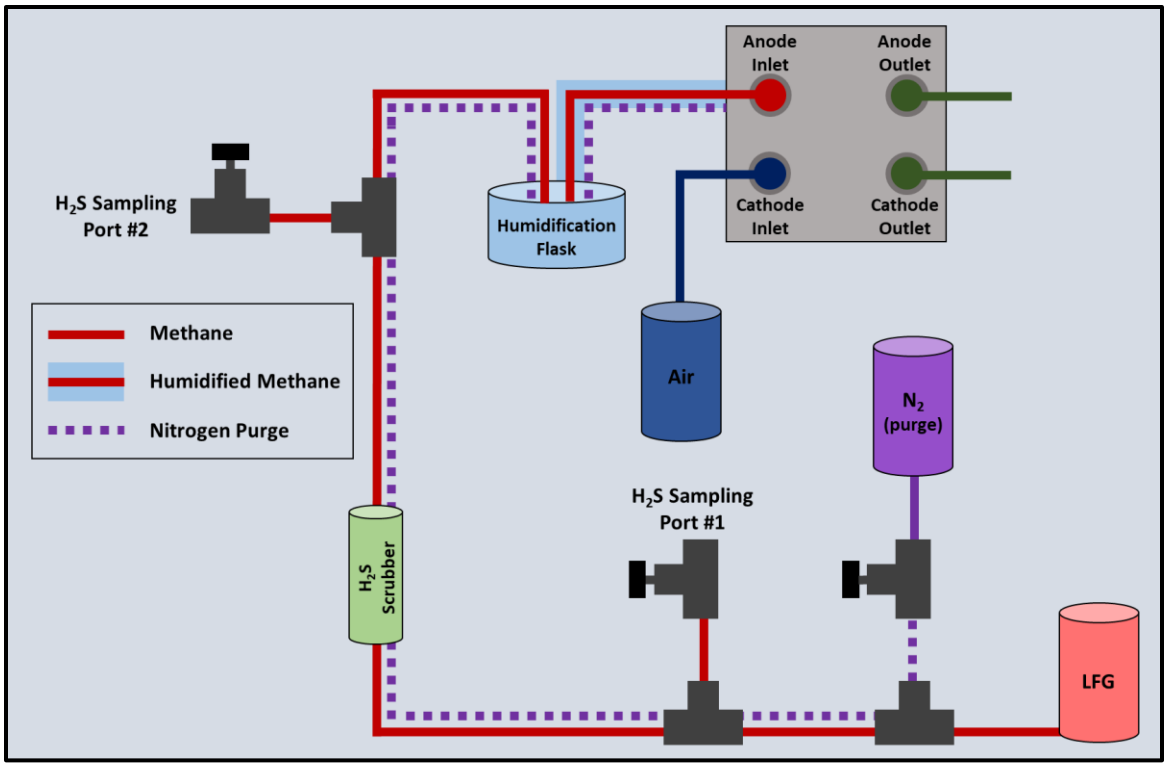

Figure 2.10: Apparatus for operating the button cell on landfill gas.

PART IV: Anode Surface Analysis.

Surface analysis techniques were used to examine the anode after the cell had undergone the experiments described in Part II and Part III of this chapter. The techniques used provided qualitative and quantitative data about the materials present on the anode surface.

Scanning Electron Microscopy (SEM) with Secondary Electron Imaging (SEI)

Youngstown State University's Electron Microscopy Facility houses a JEOL JIB-4500 Multi Beam System scanning electron microscope. Capable of resolutions as high as 2.5 nm,[35] the SEM was used for qualitative comparisons of the anode surface of the button cells before and after they were operated under the conditions described in Parts II

and III. Secondary electron imaging (SEI) was used to obtain information about the anode's surface topography. In SEI, an incident electron from the electron beam, in this case generated by a lanthanum hexaboride emitter, transfers an amount of energy to an electron in the sample's outer shell. This small-angle, inelastic collision causes the newly-ionized outer shell electron to escape as a secondary electron. These secondary electrons are collected on a secondary electron detector, generating an image of the sample surface.

Energy-Dispersive X-Ray Spectroscopy (EDS)

The JEOL JIB-4500 Multi Beam System scanning electron microscope at Youngstown State University is equipped with an EDAX APOLLO XV X-ray energy dispersive spectrometer.[35] When the electron beam strikes the sample, X-ray photons are emitted. Because different elements have unique emission energies, the measured energy is used to determine the elements present. Integrating the areas of the measured peaks provides quantitative information about the concentration of each element present in the sample. Because the main objective of this research was to examine the effects of siloxanes on the SOFC anode, the detection of silicon was especially important.

X-Ray Fluorescence Spectroscopy (XRF)

The Bruker AXS S2 Ranger is an X-ray fluorescence (XRF) spectrometer is used for the elemental and chemical analysis of powder and solid samples.[36] The principle behind this instrument is similar to XRD, SEM, and EDS techniques. When X-rays from the instrument strike the sample, atoms become ionized, releasing an electron from the inner shell. An outer shell electron then takes the place of the emitted electron, releasing

energy in the process. This energy, called fluorescence, is characteristic for a given material. The main limitation of the S2 Ranger instrument is that it cannot detect elements lighter than sodium. Here, the S2 Ranger was used to study the composition of Ceramabond, an alumina and silicate material.[28]

CHAPTER 3: RESULTS AND DISCUSSION

PART I: Initial Voltammetric Experiments on Ni-YSZ/Hionic™/LSM Button Cells

Button Cell Operated on Hydrogen

Using the setup illustrated in Figure 2.5, the button cell was operated on hydrogen to test its voltage-current output and resistance. The cell was heated to 750°C, and hydrogen was fed into the anode at a rate of 100 mL/min, while air was fed into the cathode at a rate of 50 mL/min. The load box was used to decrease the resistance from 9999 Ω to 1999 Ω in 1000-Ω increments, 999 Ω to 199 Ω in 100-Ω increments, and 99 Ω to 19 Ω in 10-Ω increments, and the resulting voltage was plotted against the current at each increment. The resistance was then increased using the same increments, and voltages were again plotted against the currents. This data is shown in Figure 3.1.

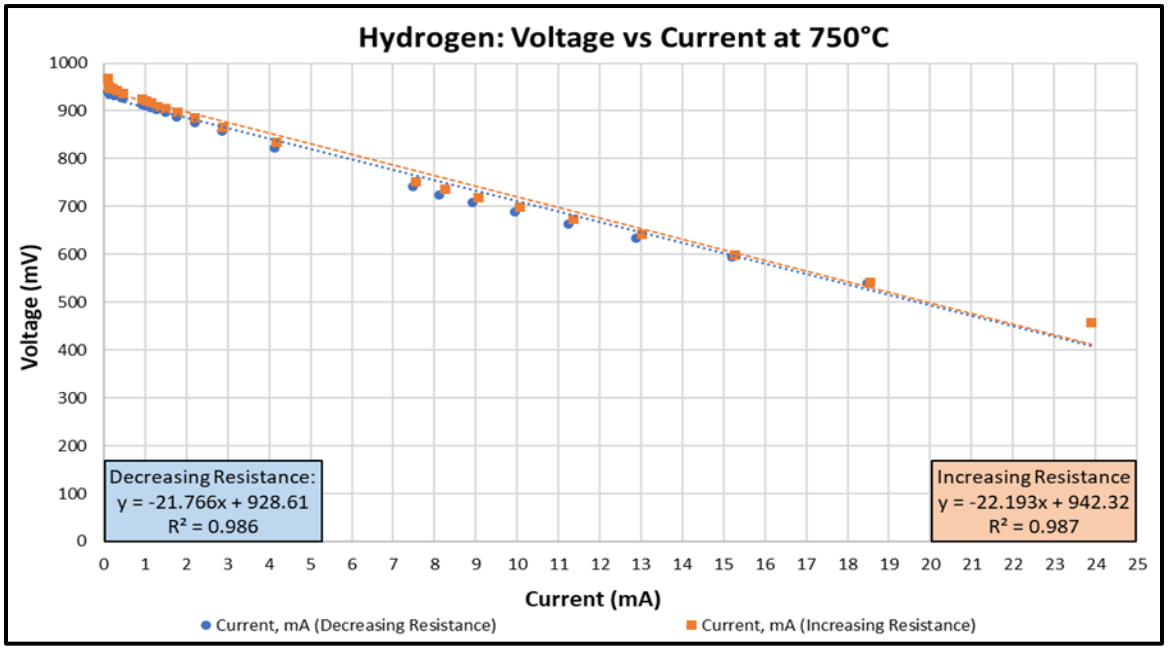

Figure 3.1: Voltage vs current plot for the Ni-YSZ/Hionic™/LSM button cell operated on hydrogen at 750°C

Based upon the linear relationship between the voltage and current, ohmic resistance dominates under the conditions described above. When linear regression is used to fit a line to each data series, the absolute value of the slope represents the resistance of the cell, and the y-intercept represents the open-circuit voltage. In the case of the button cell operated on hydrogen, the resistance was approximately 22 Ω.

To simplify comparisons to published data, voltammetric data for fuel cells is typically reported as a polarization curve, in which the cell voltage is plotted against the current density, *j*. The current density is described by

$$\mathrm{j} = \frac{\mathrm{i}}{\mathrm{A}} \qquad (3.1),$$

where *A* is the active cell area. The button cells used in this experiment had an electrode diameter of 12.5 mm, for an active cell area 1.23 cm^2. Figure 3.2 gives the data reported in Figure 3.1 as a polarization curve.

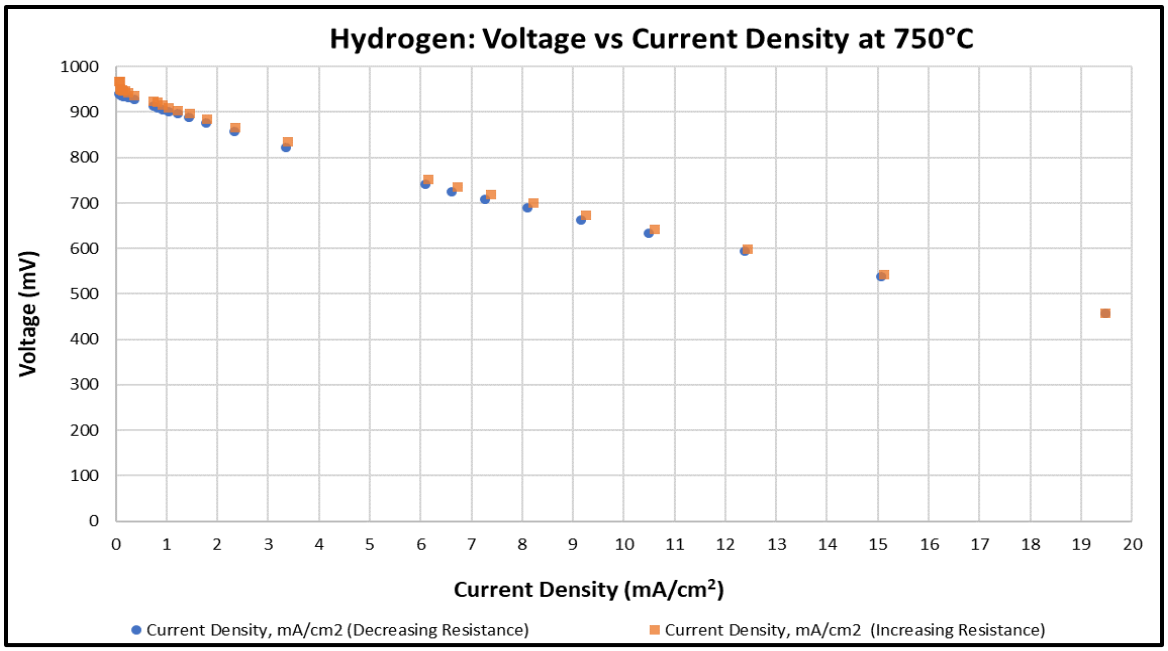

Figure 3.2: Polarization curve for the Ni-YSZ/Hionic™/LSM button cell operated on hydrogen at 750°C

Recall that when a fuel cell is operated on hydrogen, the reaction is described by

$$2H_2 + O_2 \rightarrow 2H_2O \qquad (1.4).$$

Assuming complete reversibility, the theoretical maximum voltage, E°, can be calculated using the Gibbs free energy released by the formation of water. When enough hydrogen and oxygen are consumed to make one mole of water, the calculation for E° is given by Equation 3.2.

$$E° = \frac{-\Delta G}{nF} \qquad (3.2)$$

Two electrons are transferred when one mole of hydrogen is consumed to make one mole of water, so $n = 2$. At 750°C, ΔG = -202.10 kJ/mol,[37] so the theoretical open-circuit voltage, E°, is 1.05 V. The experimental value for the button cell operated on hydrogen was 0.942 V. The theoretical value does not account for irreversibility in the system, so

the experimental open-circuit voltage is expected to be less than the theoretical value. Because the Gibbs free energy value for the hydrogen-operated SOFC decreases as temperature increases, applying Equation 3.2, one would expect to see the open-circuit voltage decrease with increasing temperature. In practice, however, higher voltages can be obtained by increasing the temperature, as shown in the next set of data.

Button Cell Operated on Humidified Methane

Using the apparatus shown in Figure 2.6, the cell was operated on humidified methane blended with 89°C water vapor (vapor pressure = 506 torr, or 67% humidification) and fed into the anode at a rate of 50 mL/min. Air was fed into the cathode at a rate of 100 mL/min. Figure 3.3 shows the voltage versus current curves for the button cell operated under the above conditions at 750°C, 800°C, 850°C, and 900°C. As with the hydrogen experiment reported in Figure 3.1, the load box was used to decrease the resistance from 9999 Ω to 1999 Ω in 1000-Ω increments, 999 Ω to 199 Ω in 100-Ω increments, and 99 Ω to 19 Ω in 10-Ω increments, with voltage and current readings recorded at each increment. This data is represented by the solid markers labeled "°C inc." Similarly, the data recorded as the load box resistance was increased is represented by the outlined markers labeled "°C dec."

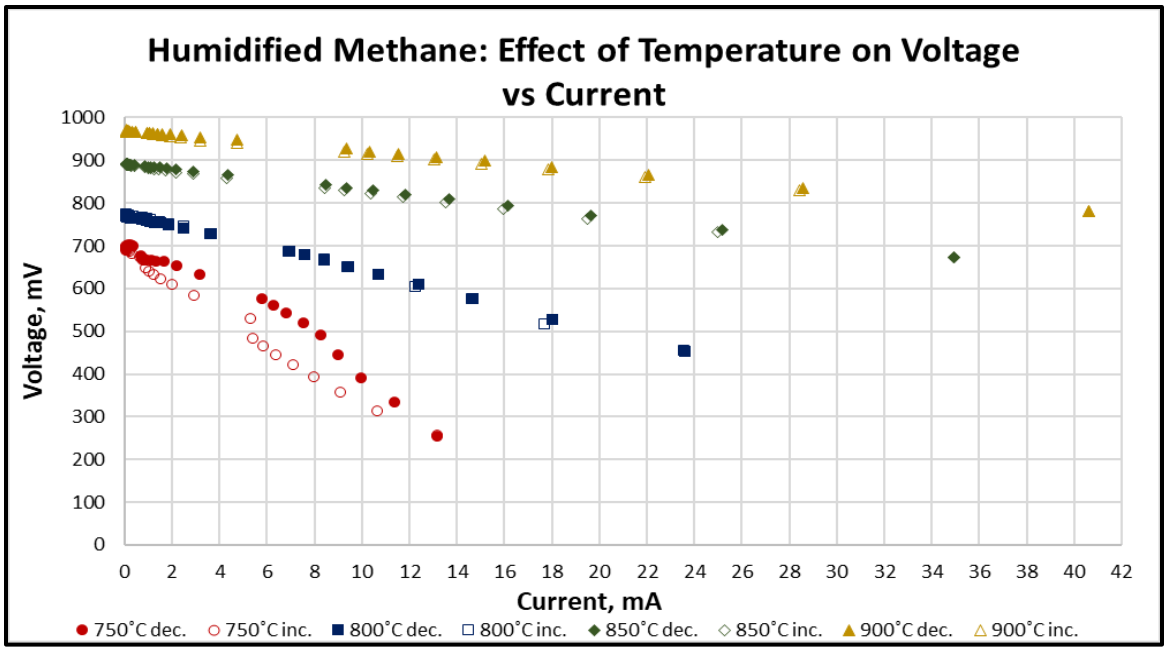

Figure 3.3: Voltage vs current plot for the Ni-YSZ/Hionic™/LSM button cell operated on humidified methane at 750°C, 800°C, 850°C, and 900°C

Because the curves are nearly linear, ohmic resistance dominates in this region. In Figure 3.3, the plots of voltage versus current at 750°C, 800°C, 850°C, and 900°C show a trend of decreasing resistance with increasing temperature, which can be explained by the effects of the electrolyte on cell conductivity. In the button cell, much of the surface area is composed of the electrolyte, which becomes more conductive as the temperature increases, as shown in Figure 3.4, taken from the proceedings of a 1983 conference on SOFC electrolytes.[38]

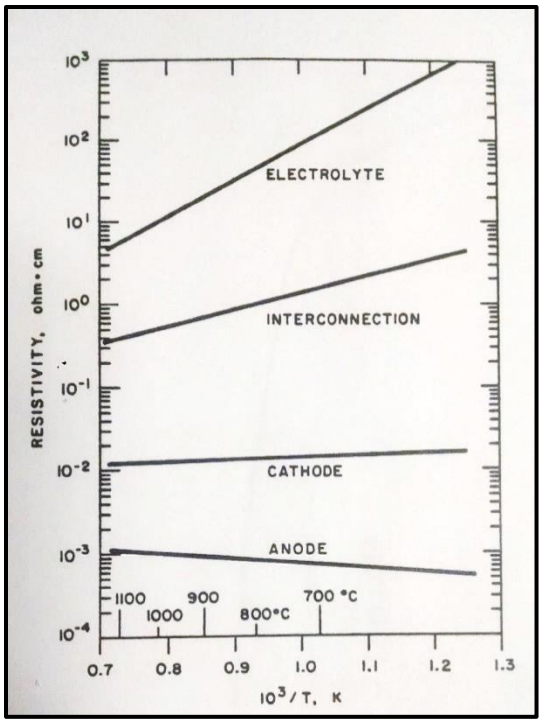

Figure 3.4: Relationship between SOFC material resistivity and temperature; note that as temperature increases, the resistivity of the electrolyte decreases.[38]

The data for the button cell operated on humidified methane showed a greater open-circuit voltage at higher temperatures, while Equation 3.2 predicted lower open-circuit voltages at higher temperatures. As previously mentioned, Equation 3.2 assumes complete reversibility in the system, ignoring the effects of activation losses and resistance. In a real system, these factors exist, meaning that irreversibility exists in the system and that the actual open-circuit voltage will usually be less than the theoretical value. Similarly, these sources of irreversibility explain why the inverse relationship between open-circuit voltage and temperature predicted by Equation 3.2 does not hold true. At higher temperatures, reactions proceed more rapidly, decreasing activation losses due to the initial slowness of reactions at the surface of the electrode. Likewise, for a cell whose surface area is mostly comprised of the electrolyte, the resistance decreases with

increasing temperature. These factors explain the trends of increasing open-circuit voltage and decreasing resistance as the temperature increased, shown in Figure 3.3.

As with the button cell operated on hydrogen, the data for the button cell operated on humidified methane can be reported as polarization curves. These are shown below in Figure 3.5 through Figure 3.8.

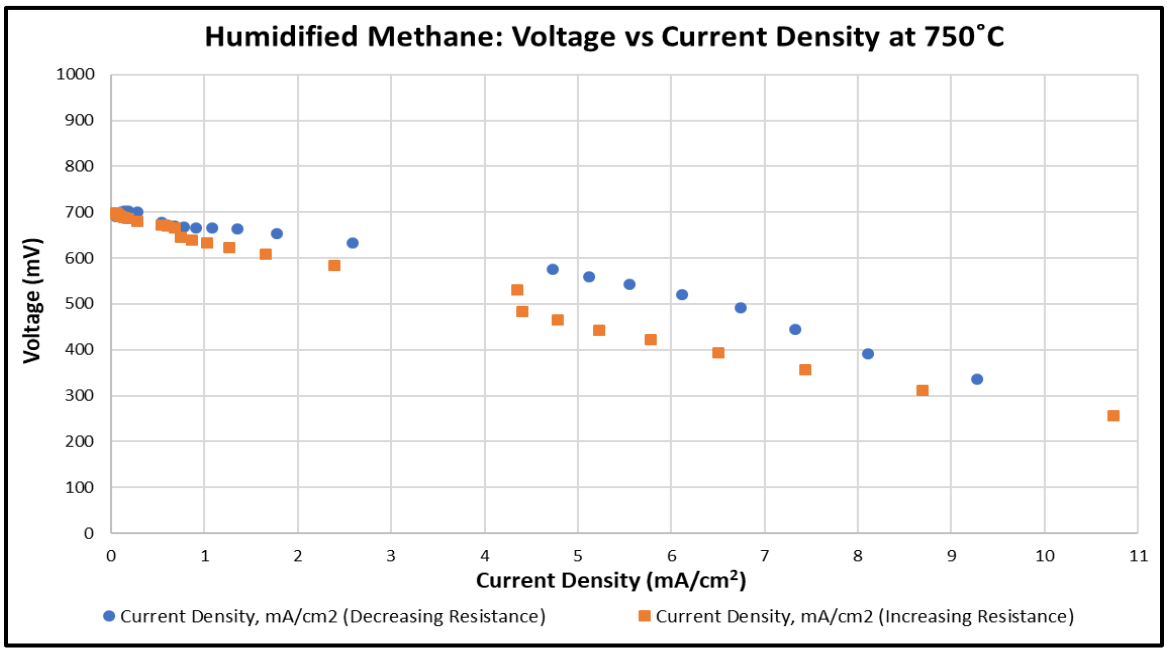

Figure 3.5: Polarization curve for the Ni-YSZ/Hionic™/LSM button cell operated on humidified methane at 750°C

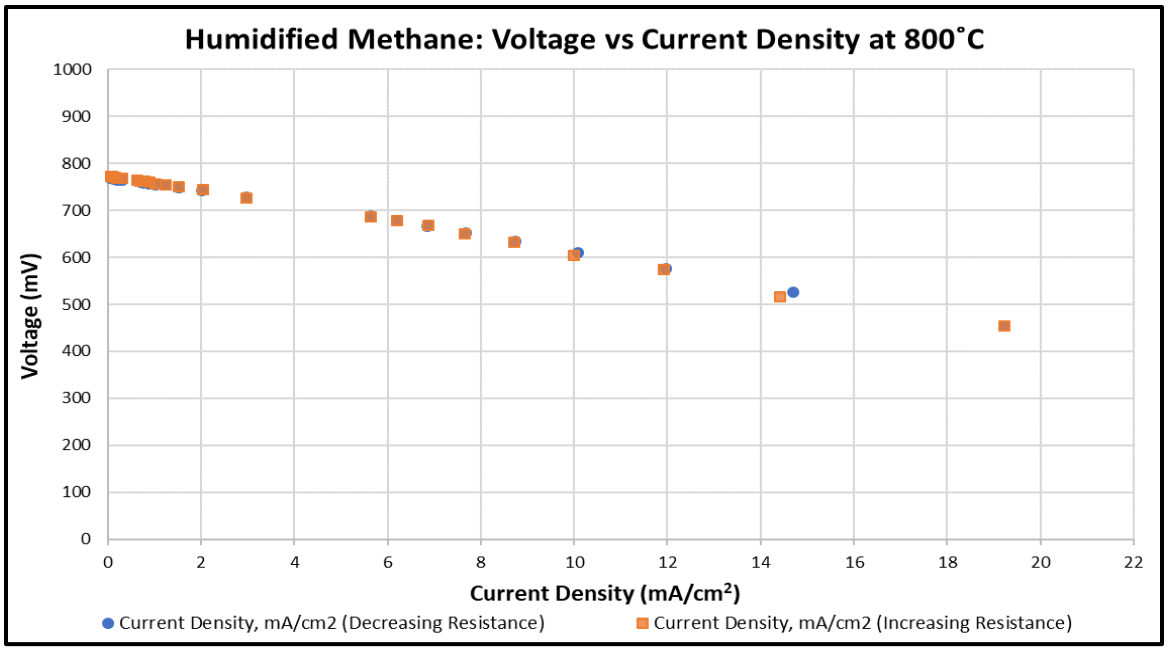

Figure 3.6: Polarization curve for the Ni-YSZ/Hionic™/LSM button cell operated on humidified methane at 800°C

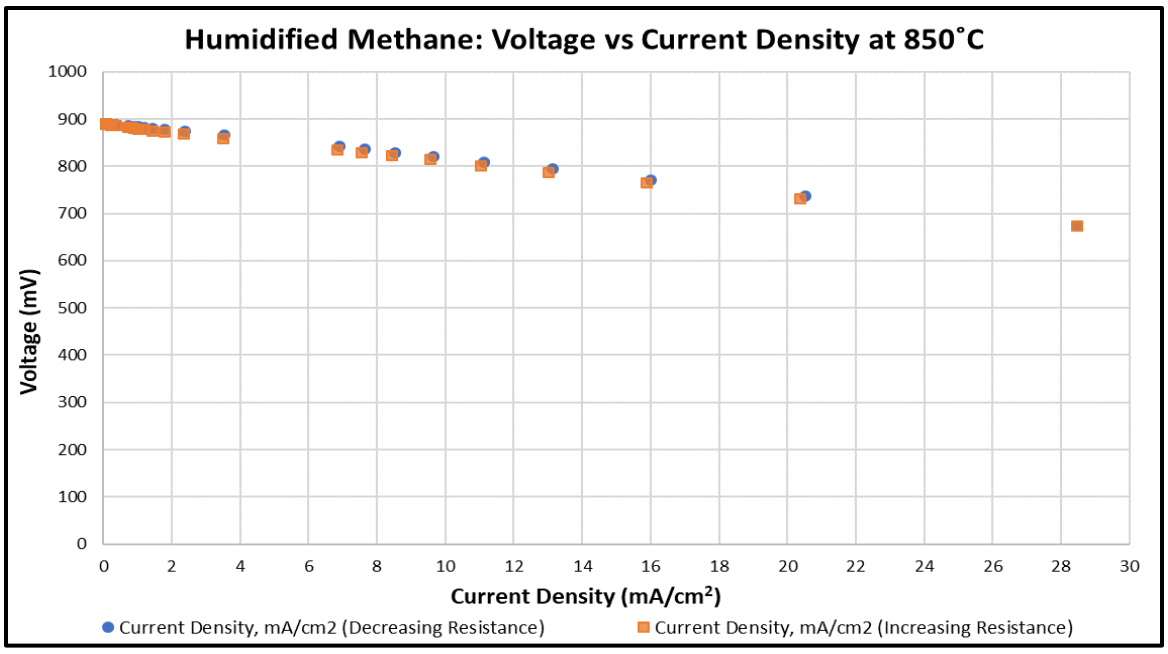

Figure 3.7: Polarization curve for the Ni-YSZ/Hionic™/LSM button cell operated on humidified methane at 850°C

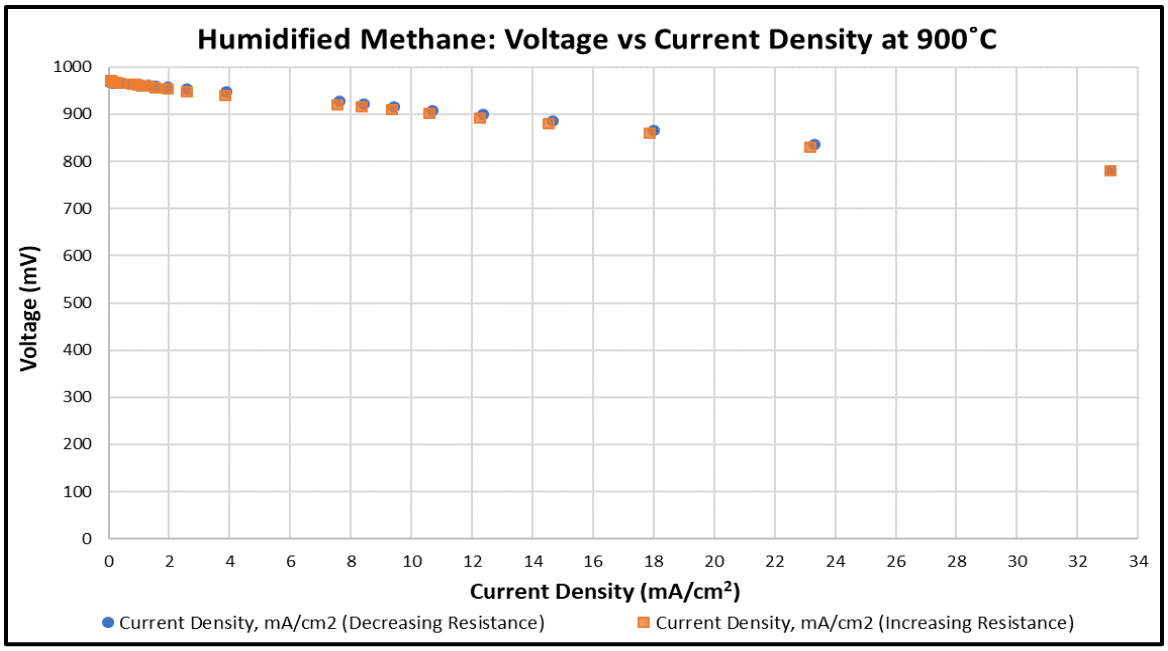

Figure 3.8: Polarization curve for the Ni-YSZ/Hionic™/LSM button cell operated on humidified methane at 900°C

The polarization curves given in Figure 3.5 through Figure 3.8 do not match the typical polarization curve for a solid oxide fuel cell, shown in Figure 3.9, which was based on a review by Huang et al.[39]

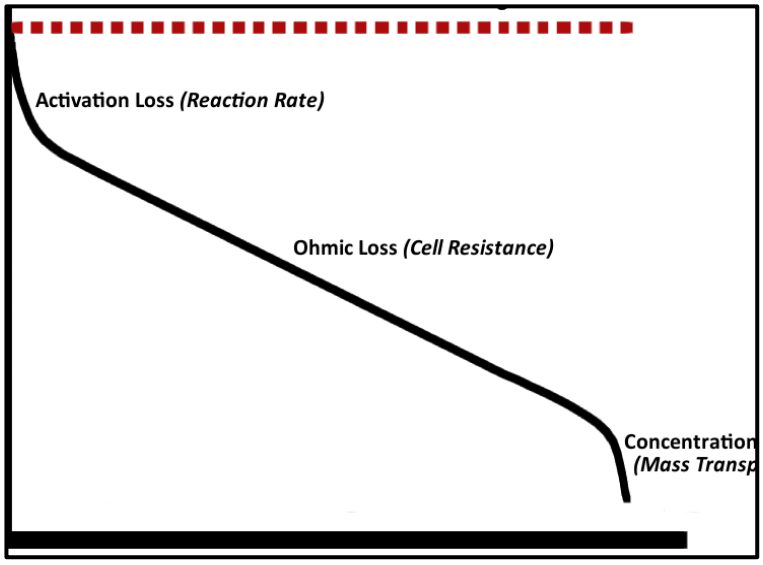

Figure 3.9: Typical SOFC polarization curve

The curve in Figure 3.9 has three distinct regions, indicating the three factors that cause the cell's voltage to deviate from the theoretical maximum, represented by the dashed line. These factors are the activation loss due to the rate of cell reactions, the ohmic loss due to cell resistance, and the concentration loss due to mass transport.[39] Unlike the typical polarization curve, the curves shown in Figure 3.5 through Figure 3.8 only show the ohmic loss region corresponding to the linear portion of Figure 3.9. As the operating temperature of the cell increased, the slope of the linear ohmic loss region decreased, suggesting that the electrolyte is the primary source of resistance in the cell.

As the operating temperature increased, the voltage and current output of the cell increased. Comparing the voltammetric data in Figure 3.5 to the data in Figure 3.8 shows that the maximum current density achieved by the cell increased from approximately 11 mA/cm^2 to 33 mA/cm^2 as the operating temperature was raised by 150°C. Based on these results, it may be worthwhile to operate solid oxide fuel cells at a temperature greater than 750°C, as the performance improved as temperatures increased.

PART II: Voltammetric Experiments on Ni-YSZ/Hionic™/LSM Button Cells Operated on Humidified Methane Spiked with Decamethylcyclopentasiloxane

To examine how siloxanes affect SOFC function over time, a button cell was operated on humidified methane at 750°C. The load box resistance was set to 99 Ω, and the cell was given time to reach a steady state, during which its voltage and current output was monitored. Then, a known concentration of D5 was introduced into the fuel gas, and voltage and current measurements were made every 15 minutes until the voltage output showed significant decay (or until it was evident that the siloxane had no measurable effect). The button cell was operated on 50 mL/min of humidified methane

(89°C humidification flask temperature for a water vapor pressure of 506 torr, or 67% humidification) and 100 mL/min of air. Concentrations of D5 were varied, keeping in mind that a typical landfill gas sample contains volatile organic silicon compound (VOSC) concentrations between 0.41 ppmv and 13.9 ppmv.[31] Figure 3.10 shows the voltage and current output of the cell over time.

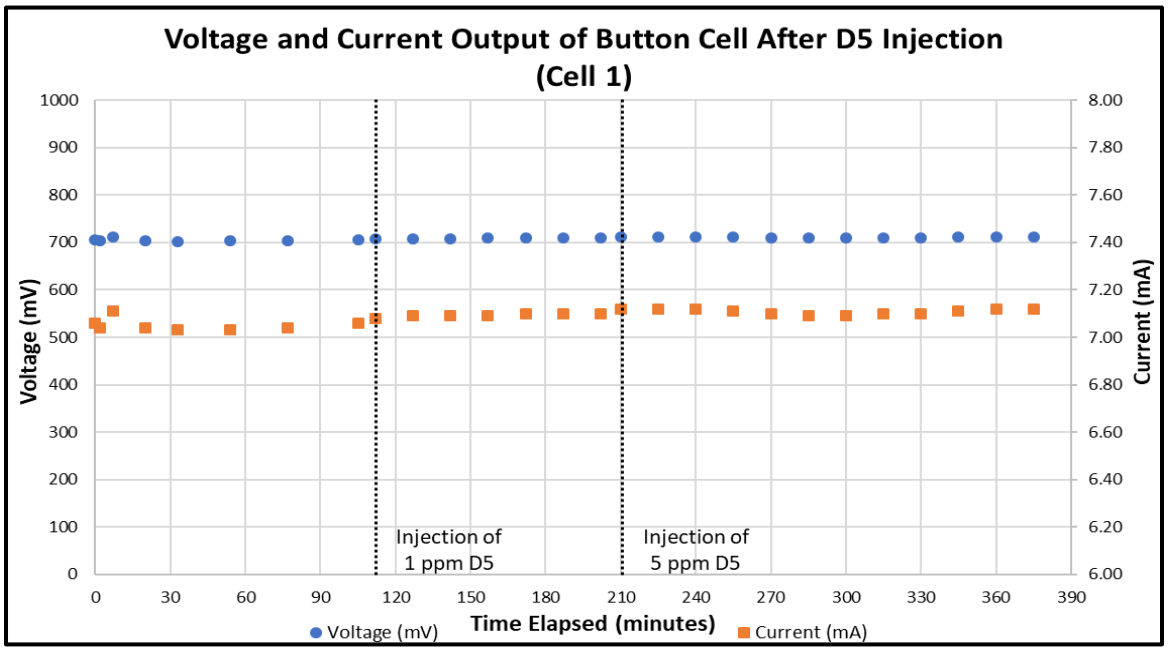

Figure 3.10: Voltage and current output of the Ni-YSZ/Hionic™/LSM button cell operated on 50 mL/min of humidified CH_4 and 100 mL/min of air. After 112 minutes had passed, 1 ppmv D5 was injected into the fuel stream, and 5 ppmv D5 was injected after 210 minutes had elapsed.

Figure 3.10 suggests that D5 concentrations of 1 ppmv and 5 ppmv did not have an appreciable effect on the cell's voltage and current output. The cell ran for 6.5 hours without losing function. When the ProboStat™ assembly was opened, there was evidence of silica deposition. A buildup of a white solid, shown in Figure 3.11, was observed at the top of the outer alumina tube, the portion of the ProboStat™ that maintains the highest temperature during operation. Because siloxanes decomposition requires water and a

sufficiently high temperature, it is likely that the D5-spiked gas flow reaches the alumina tube surface before it reaches the anode of the cell. As a result, silica forms on the ProboStat™, and the anode is unaffected by D5.

Figure 3.11: The arrow points to the white silica deposits on the inside top of the ProboStat™'s outer alumina tube.

Because the goal of this portion of research is to observe the effects of D5 on the anode, it was necessary to modify the apparatus to ensure that D5 would reach the anode. A curved quartz tube, included with the ProboStat™, was attached to the anode gas inlet using a piece of silicone tubing, directing the gas flow from the anode chamber gas inlet to the anode surface. The silicone tubing fit snugly around the anode gas inlet and the bottom of the quartz tube, not allowing gas to escape until it reached the opening at the top. This is shown in Figure 3.12.

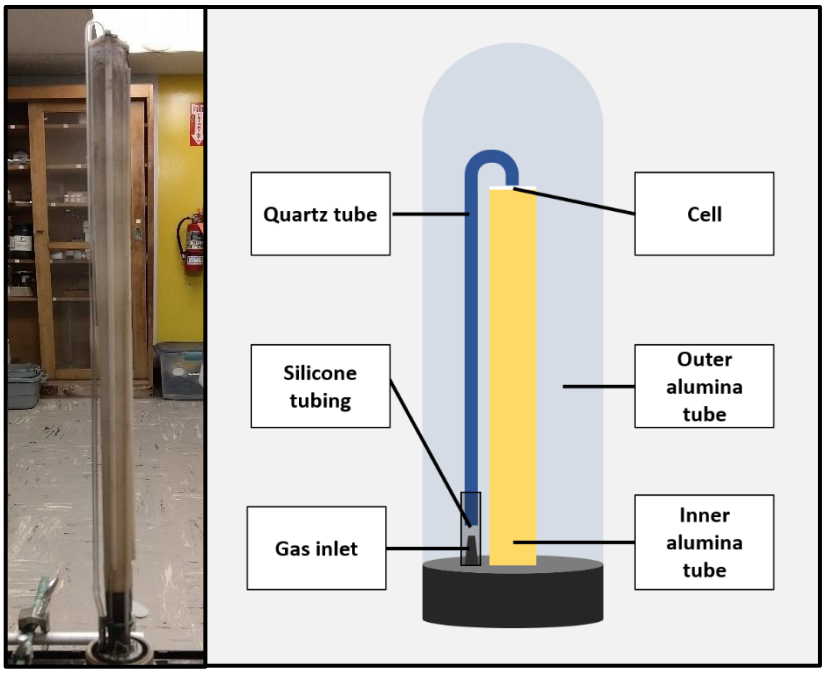

Figure 3.12: The curved quartz tube (left) delivers gas directly from the gas inlet to the anode. On the right is an illustration, showing the quartz tube more clearly.

After the quartz tube was added to the apparatus, a new button cell was fixed to the ProboStat™. However, after an hour of operation, the cell had developed a hole. As with the planar cell experiments, which are discussed in Chapter 5 of this paper, the cracks were hypothesized to form because of a buildup (and sudden release) of pressure caused by trapped condensate. Though heating tape is used to prevent water vapor from condensing before it enters the base of the ProboStat™, little can be done to control condensation inside the ProboStat™ itself; while the portion of the instrument enclosed by the tube furnace (the "hot zone") maintains the set temperature of 750°C, the temperature of the portion where the humidified gas enters the anode chamber may range from 70°C to 165°C,[29] allowing water vapor to condense. Before the addition of the quartz tube, the humidified fuel gas flowed out of the gas inlet and into the outer chamber, so condensate could freely fall back onto the base of the ProboStat™ without

causing an obstruction to gas flow. However, as the earlier experiment showed, it was necessary to place a tube over the anode gas inlet to direct gas flow to the anode.

With the quartz tube in place, the humidified gas was forced to flow through a tube with a diameter of approximately 4 mm. In this setup, the only exit point is the opening of the quartz tube, which is located directly above the anode. Since portions of the quartz tube exist outside of the ProboStat™'s "hot zone," condensate forms and accumulates inside the quartz tube, forming a plug of water. When enough pressure, generated by the incoming gas flow, builds up behind the plug of water, the plug and gas trapped behind it are forcefully launched through the quartz tube and expelled out its open end. As this happened, the cell experienced a burst of pressure, causing it to crack. Figure 3.13 supports this hypothesis, as the large chip in the cell occurred at the opening of the quartz tube, where gas first encounters the cell.

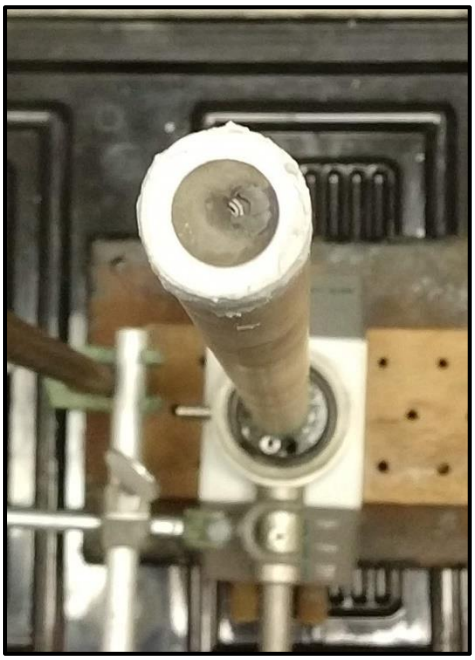

Figure 3.13: The chip in button Cell #2 corresponds to the opening of the quartz tube.

To alleviate the pressure buildup inside the quartz tube and the resulting forceful expulsion of water and gas onto the cell, the ProboStat™ was slightly modified. A Teflon cone was placed over the gas inlet, and the top of this cone was connected to the bottom of the quartz tube using silicone tubing, as shown in Figure 3.14. The cone creates space between the gas inlet and the quartz tube, allowing water vapor to collect on the sides of the cone and drip down into the base of the ProboStat™. This prevents condensate from becoming trapped in the quartz tube and creating pressure. Furthermore, the height of the cone raises the quartz tube into the ProboStat™'s "hot zone," ensuring that water remains in the vapor phase as it travels through the tube.

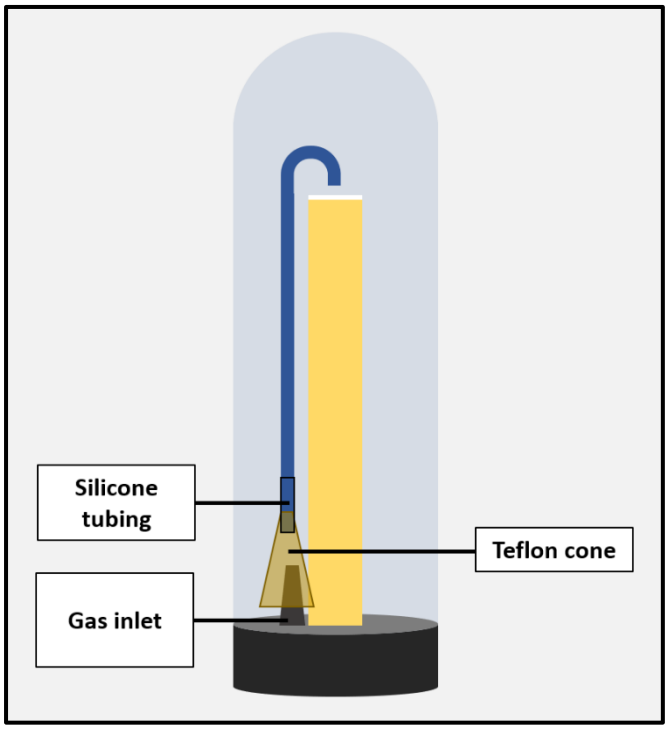

Figure 3.14: The Teflon cone allows condensate to escape, preventing it from becoming trapped in the quartz tube.

With the Teflon cone in place, the experiment was repeated with concentrations of 1 ppmv, 5ppmv, and 10 ppmv D5 in humidified methane. The voltage and current data for the first test on button Cell #3 ("Cell 3a") are shown in Figure 3.15.

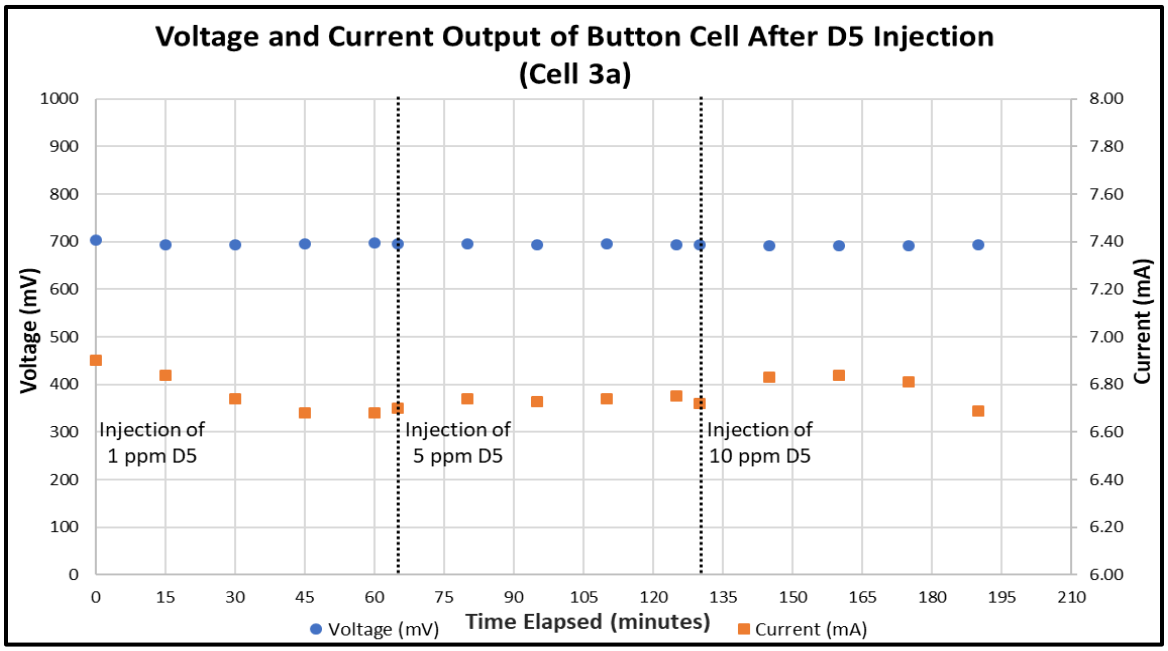

Figure 3.15: Voltage and current output of the Ni-YSZ/Hionic™/LSM button cell operated on 50 mL/min of humidified CH_4 and 100 mL/min of air. The load box resistance was set to 99 Ω, and once a steady state was reached, 1 ppmv D5 was injected into the fuel stream. 5 ppmv D5 was injected after 65 minutes had elapsed, and 10 ppm D5 was injected after 130 minutes had elapsed.

As with Cell #1, the introduction of D5 into the fuel gas seemed to have no effect on the cell's voltage and current output, with both remaining stable over approximately 3 hours. To verify these results, a second experiment was performed on Cell #3 ("Cell 3b") with injections of 10 ppmv D5 and 100 ppmv D5 after the cell had reached a steady state at a load of 99 Ω. The results of this experiment are shown in Figure 3.16.

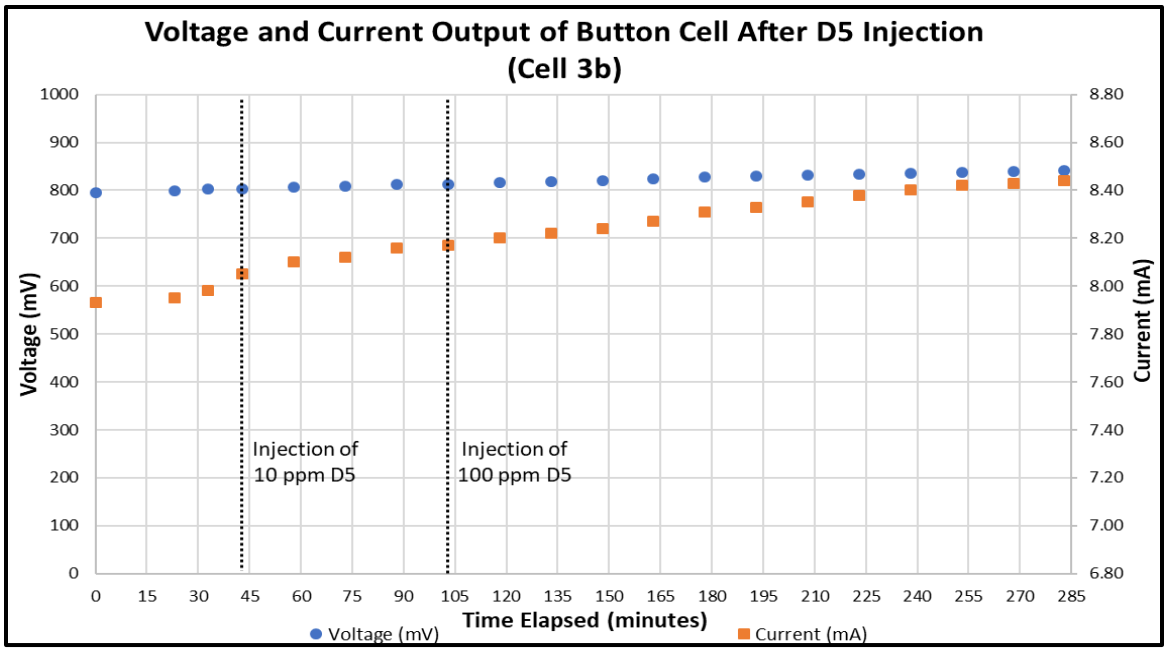

Figure 3.16: Voltage and current output of the Ni-YSZ/Hionic™/LSM button cell operated on 50 mL/min of humidified CH_4 and 100 mL/min of air. The load box resistance was set to 99 Ω, and 10 ppmv D5 was injected into the fuel stream after 43 minutes had elapsed at steady state. 100 ppmv D5 was injected after 103 minutes had elapsed.

Even at a D5 concentration that is an order of magnitude higher than what is found in a typical landfill gas sample, the cell showed no evidence of anode poisoning through silica deposition. Unexpectedly, though the experiments shown in Figure 3.15 and Figure 3.16 were performed using the same cell, the voltage and current output of the cell was greater during the trial described in Figure 3.16. This could be due to the anode becoming more reduced over time, allowing electrochemical reactions to occur more readily. The results do suggest, however, that the injection of D5 did not negatively affect anode function. When the apparatus was disassembled, a white rind, shown in Figure 3.17, was found on the outside of the quartz tube.

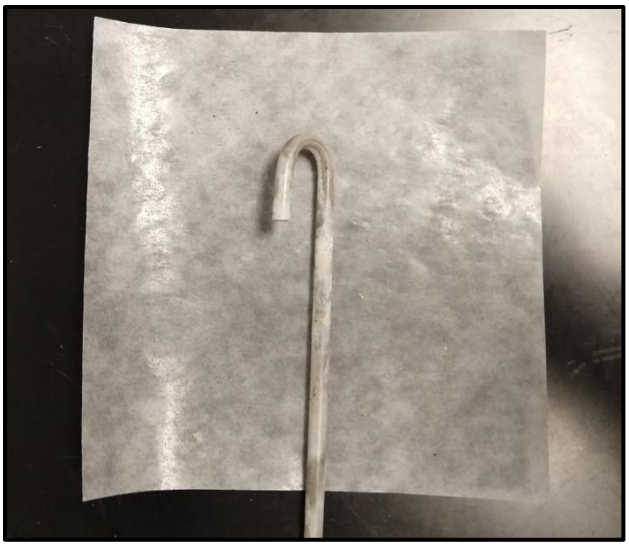

Figure 3.17: A white deposit was found on the quartz tube.

The white deposit from the outside of the quartz tube was scraped and then analyzed using the Bruker AXS X8 Prospector. X-ray diffraction data, shown in Figure 3.18, revealed the sample to be crystalline quartz.

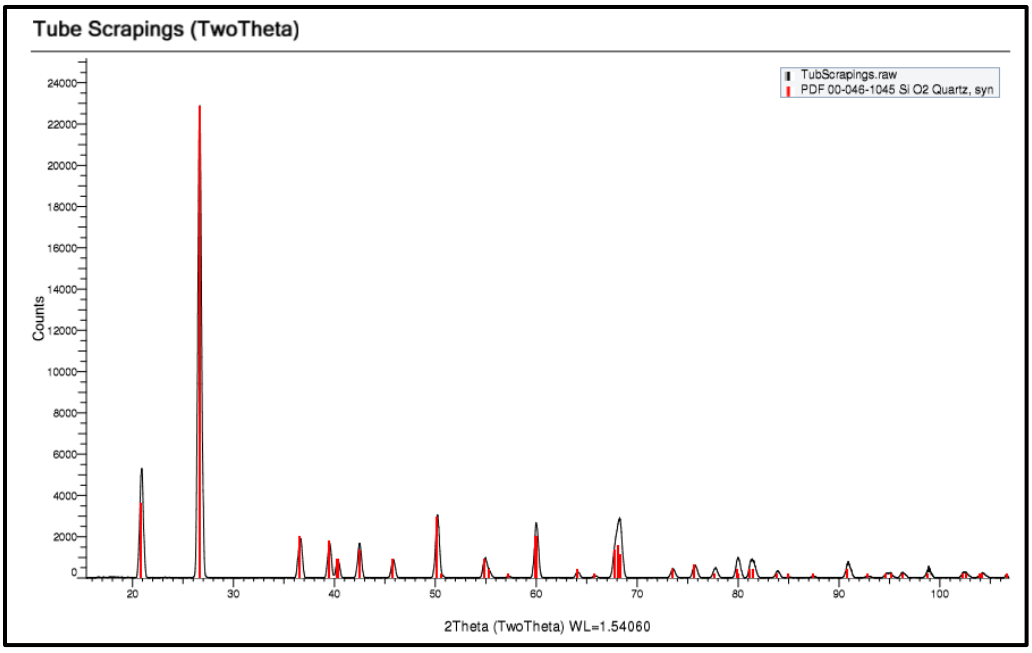

Figure 3.18: XRD analysis of the tube scrapings shows that the white deposit is crystalline quartz.

For comparison, an unused piece of quartz tubing was also analyzed. Figure 3.19 shows the XRD data for the quartz tube imposed over the data for the tube scrapings. While the tube scrapings had a high degree of crystallinity, as indicated by the sharp peaks in the diffraction pattern, the quartz tube itself was amorphous, showing a broad hump. This suggests that the scrapings were deposited silica.

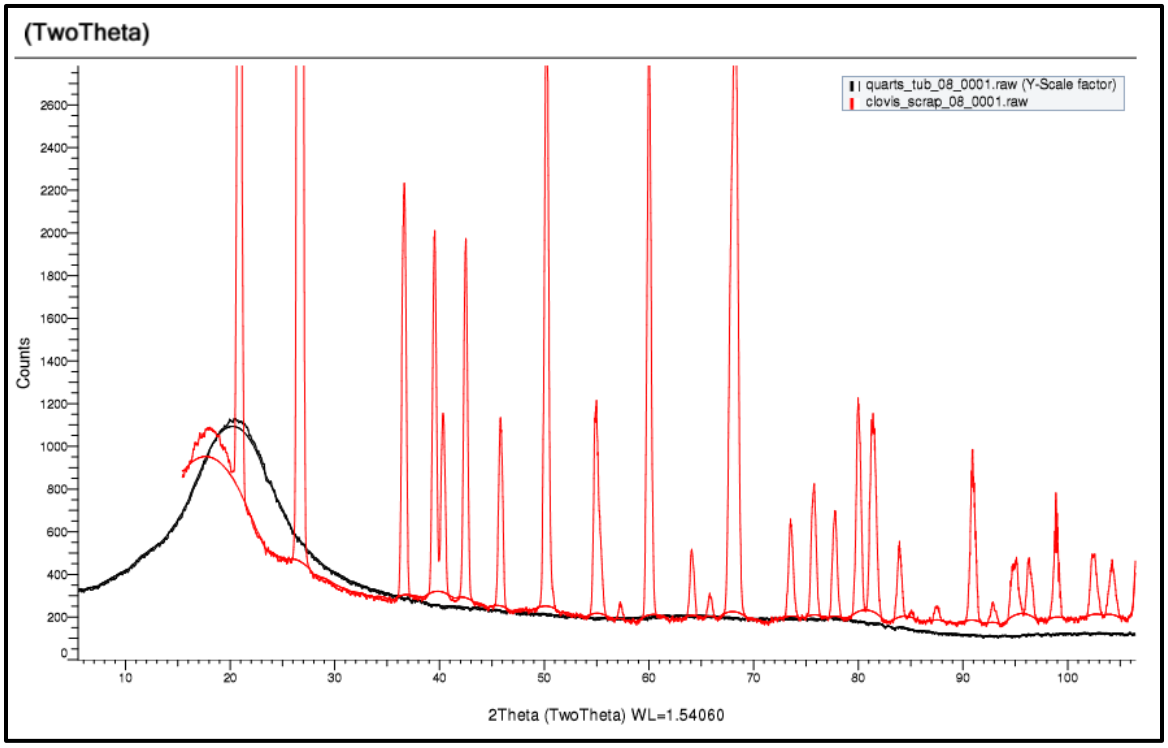

Figure 3.19: XRD data from the quartz tube (shown in black) imposed over the data from the tube scrapings (shown in red).

Some of the scraped sample was also sent to Material Research Laboratories, where energy-dispersive X-ray spectroscopy further confirmed that the sample was quartz. The EDS data is given in Figure 3.20.

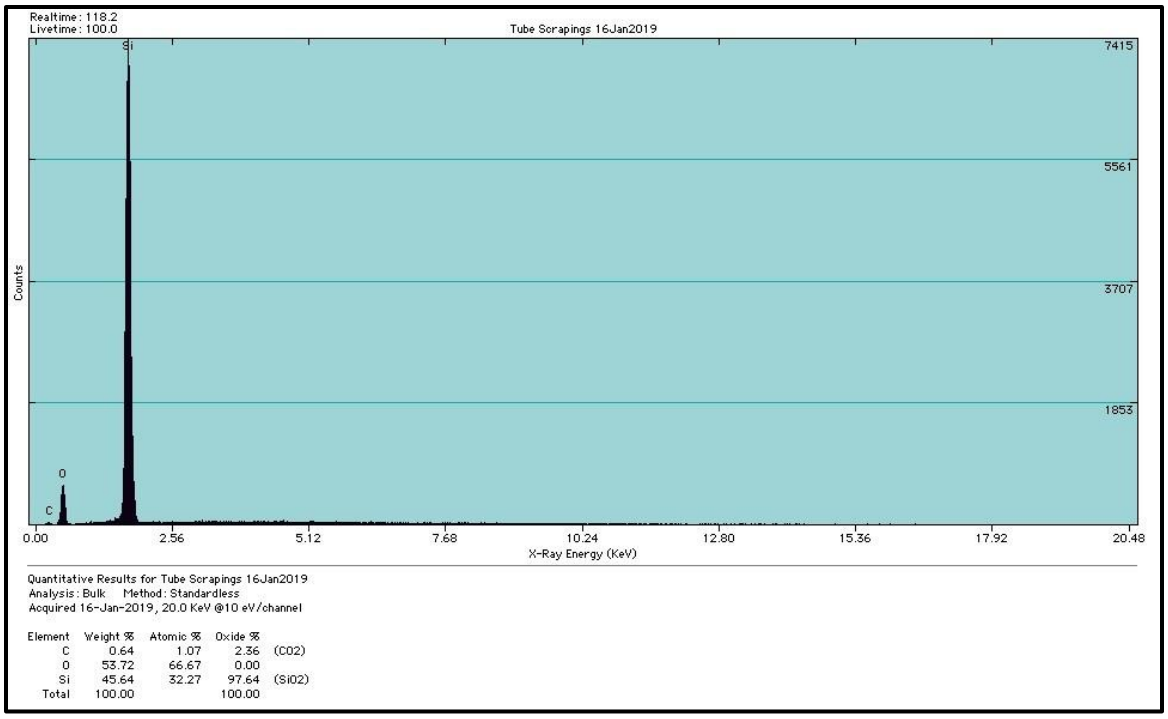

Figure 3.20: EDS analysis identified the white deposit as quartz.

When siloxanes decompose at high temperatures in the presence of water, they deposit silica on available surfaces. Based on XRD and EDS data, the sample scraped from the quartz tube was quartz, a crystalline form of silica. This suggests that D5 underwent the decomposition reaction described in Equations 1.13 and 1.14.

Although there was evidence of silica deposition, not all the D5 injected into the cell underwent the decomposition reaction. The beaker of deionized water that the anode and cathode outlet gases bubble into had an oily film floating on its surface. It is possible that D5 condensed into the bottom of the ProboStat™ and left the instrument without reacting, or D5 degraded into smaller silicon compounds. This film was collected for liquid IR analysis, the results of which are shown in Figure 3.21. This spectrum was compared to a reference spectrum for D5, shown in Figure 3.22.

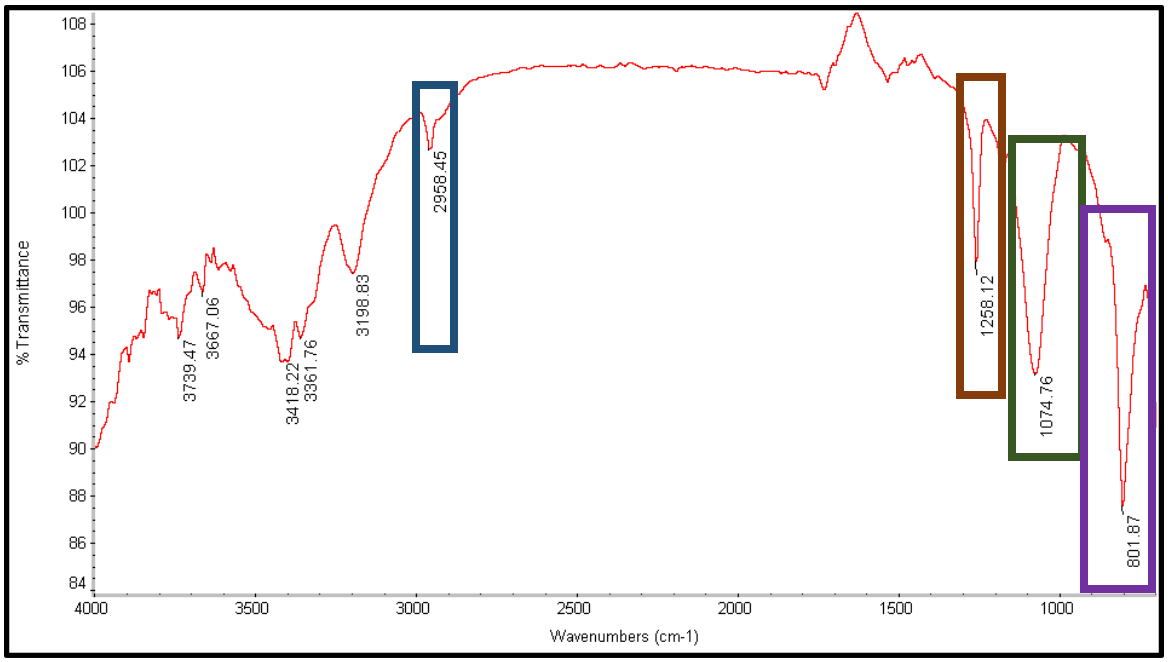

Figure 3.21: IR analysis of the film on the bubbler water, with deionized water used as the background. The relevant peaks corresponding to the reference spectrum for D5 (shown in Figure 3.23) are highlighted.

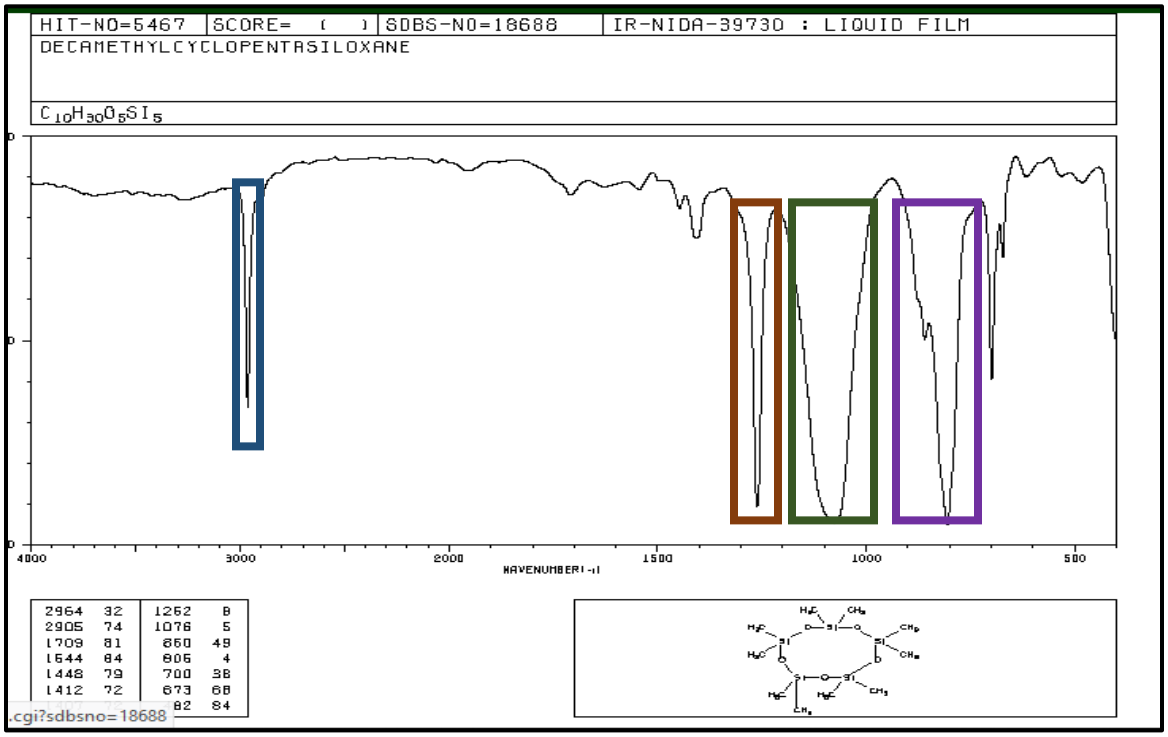

Figure 3.22: D5 spectrum from an IR database.[40] Peaks corresponding to those in Figure 3.22 are highlighted.

A comparison of the IR spectrum for the bubbler water sample (Figure 3.21) with the IR spectrum for D5 (Figure 3.22), taken from the National Institute of Advanced Industrial Science and Technology's spectral database,[40] suggests that the film contains D5. The relevant siloxane peaks and their meanings are described in Table 3.1.[41] It is very likely that some of the D5 that was injected into the gas stream condensed before entering the quartz tube that directs gas to the anode. The condensed D5 was then able to leave the ProboStat™ through the anode gas outlet and into the beaker of bubbler water.

Table 3.1: IR spectrum of bubbler water sample [41]

Bubbler Water Sample	*D5 Reference*	
Peak Position (cm^{-1})		**Bond**
2958.45	2964.32	C-H_3 stretch
1258.12	1252.8	CH_3-Si-CH_3 symmetric deformation
1074.76	1076.5	Si-O-Si asymmetric stretch
801.87	805.4	Si-CH_3 asymmetric rocking

The voltammetric data for Cell #3, given in Figure 3.15 and Figure 3.16, did not show any significant change in the voltage and current output of the button cell as D5 was injected into the system. Combined with the scrapings collected from the quartz tube, it is evident that D5 underwent decomposition before it could reach the anode. These experiments suggest that D5 and similar siloxanes are unstable under the operating conditions required for SOFCs; at sufficiently high temperatures and in the presence of water, siloxanes decompose to deposit silica on the first available surface. In the case of the ProboStat™, this surface was either the top of the outer alumina tube, or when a quartz tube was present, on the quartz tube. While the voltammetric experiments on Cell #1 and Cell #3 did not show how siloxanes affect the anode, the results suggest that

because of their instability, siloxanes may not pose a problem for the cell because they tend to decompose before reaching the anode.

Additional Tests Using Hydrogen Spiked with D5

In the previous experiments with humidified methane, it is almost certain that D5 did not reach the anode. Another attempt to understand the effect of siloxane on fuel cell performance was made, this time using hydrogen rather than methane. When hydrogen is used as the fuel, humidification is not required, as there is no danger of carbon deposition. Because there are no humidification requirements, it was possible to collect voltammetric data for a cell operating on dry hydrogen spiked with known concentrations of D5 without worrying about the cell cracking due to condensation. The experimental setup was similar to the one shown in Figure 2.8, but the humidification flask was bypassed. The quartz tube used in the Cell #3 experiment was replaced with a new quartz tube leading from the gas inlet to the anode. This ensured that D5 was delivered to the anode without a chance to condense and leave the ProboStat™, as it did when the Teflon cone was in place during the Cell #3 experiment.

When operating the cell on dry hydrogen, D5 was expected to reach the anode without reacting, as the water required for siloxane decomposition was not pumped into the system. In the first experiment on Cell #4, the cell was operated on 50 mL/min of hydrogen and 50 mL/min of air and allowed to reach a steady state at a load of 99 Ω. The hydrogen gas was then spiked with 1 ppmv D5 and later 5 ppmv D5. The voltammetric data for this experiment is given in Figure 3.23.

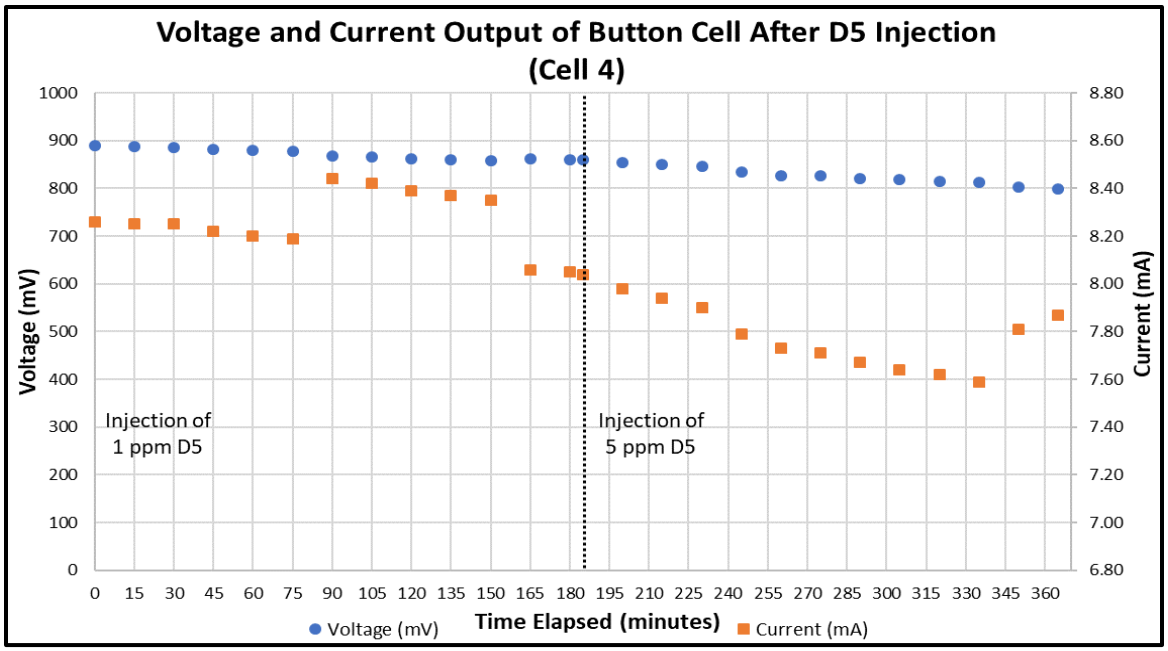

Figure 3.23: Voltage and current output of the Ni-YSZ/Hionic™/LSM button cell operated on 50 mL/min of H_2 and 50 mL/min of air. 1 ppmv D5 was initially injected, followed by 5 ppmv D5 after 185 minutes had elapsed.

While the current measurements were unreliable, the voltage measurements showed a steady downward trend. After 3 hours of operation on hydrogen spiked with 1 ppmv D5, there was a 3% loss in voltage output. When the D5 concentration was increased to 5 ppmv, the cell experienced a 7% loss in voltage output after 3 hours. Over the course of 6 hours, the voltage output of the cell had decreased from the steady state value of 889 mV to 798 mV, representing a 10% decrease in the cell's voltage output. Compared to the voltammetric data for Cells #1 and #3, which did not show any voltage decrease, this 10% loss is significant. Electron microscopy was used to determine if silica was present on the anode of Cell #4, and the results are discussed in Part IV of this chapter.

Figure 3.24 shows the anode of Cell #4 and the quartz tube after the cell was operated under the conditions described above. The exterior of the quartz tube is coated with a layer white deposit that increased in thickness as it neared the top of the quartz

tube. The deposit was carefully scraped off the quartz tube and analyzed using XRD, the results of which are shown in Figure 3.25.

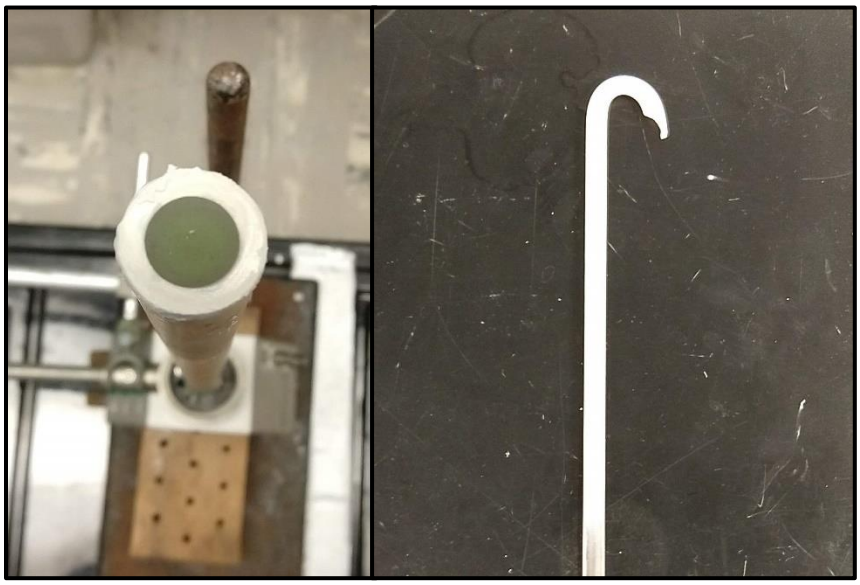

Figure 3.24: The anode of Cell #4 (left) and the quartz tube coated in a white deposit (right) after cell operation on hydrogen spiked with 1 ppmv and 5 ppmv of D5.

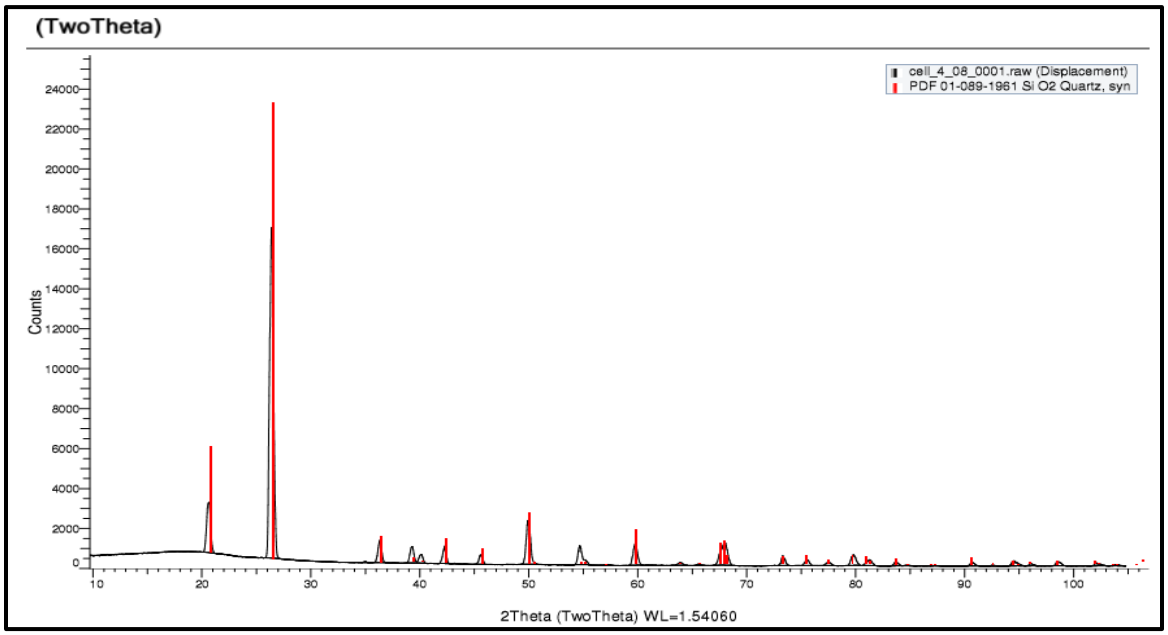

Figure 3.25: XRD analysis of the tube scrapings from the Cell #4 show that the sample is crystalline quartz.

Like the deposit scraped from the quartz tube after the Cell #3 experiment, the deposit shown in Figure 3.24 is also crystalline silica.

For verification, Cell #5 was operated under the same conditions as Cell #4, but with D5 concentrations of 10 ppmv. The voltammetric data for this experiment is given in Figure 3.26. After the cell had reached a steady state at a load of 99 Ω, the hydrogen was spiked with 10 ppmv of D5. After six hours under these conditions, the cell's voltage output had decreased from 939 mV to 817 mV, representing a 13% loss in output.

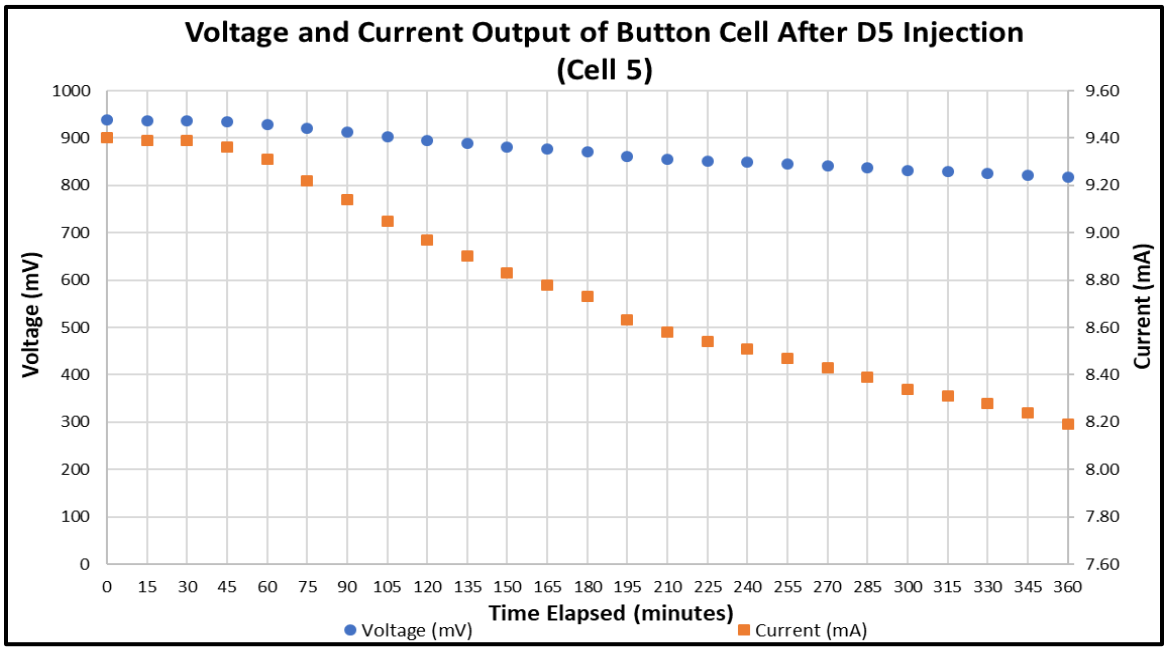

Figure 3.26: Voltage and current output of the Ni-YSZ/Hionic™/LSM button cell operated on 50 mL/min of H_2 and 50 mL/min of air. 10 ppmv D5 was initially injected at t = 0 minutes.

Recall that the decomposition of siloxane into silica proceeds according to

$$[SiO(CH_3)_2]_{n\,(g)} + 5n\,H_2O \rightarrow n\,Si(OH)_{4\,(g)} + 2n\,CO + 6n\,H_2 \qquad (1.13)$$

$$Si(OH)_{4\,(g)} \rightarrow SiO_{2\,(s)} + 2H_2O \qquad (1.14),$$

with water being necessary for the formation of orthosilicic acid, which then undergoes dehydration to form silica. In the Cell #4 and Cell #5 experiments, the fuel gas (hydrogen) was not humidified, but the formation of silica on the quartz tube indicates that water was present. This phenomenon can be explained by the fuel cell reaction

$$2H_2 + O_2 \rightarrow 2H_2O \qquad (1.4),$$

of which water is a product. Though water was not supplied to the cell, the production of water at the anode allowed the reaction shown in Equation 1.13 to proceed. Cells #4 and #5 were examined for evidence of silica deposition using SEM/EDS techniques, as described in Part IV of this chapter.

PART III: Voltammetric Experiments on Ni-YSZ/Hionic™/LSM Button Cells Operated on Mahoning Valley Landfill Gas

Detection of Hydrogen Sulfide Using Colorimetric Analysis

RAE Systems colorimetric gas detection tubes were used to analyze the hydrogen sulfide content of Mahoning Landfill gas. The gas was tested on site, directly from the gas line. The testing parameters are described in Table 3.2, and the testing tube is shown in Figure 3.27. The on-site measurement indicated that Mahoning Landfill gas contains 80 ppmv of hydrogen sulfide.

Table 3.2: H_2S content of Mahoning Landfill gas (on-site)

Range	25-250 ppmv
Number of Strokes	1
Sample Volume	100 mL
Sample Time	1 minute
Correction Factor	1
Tube Reading	80 ppmv

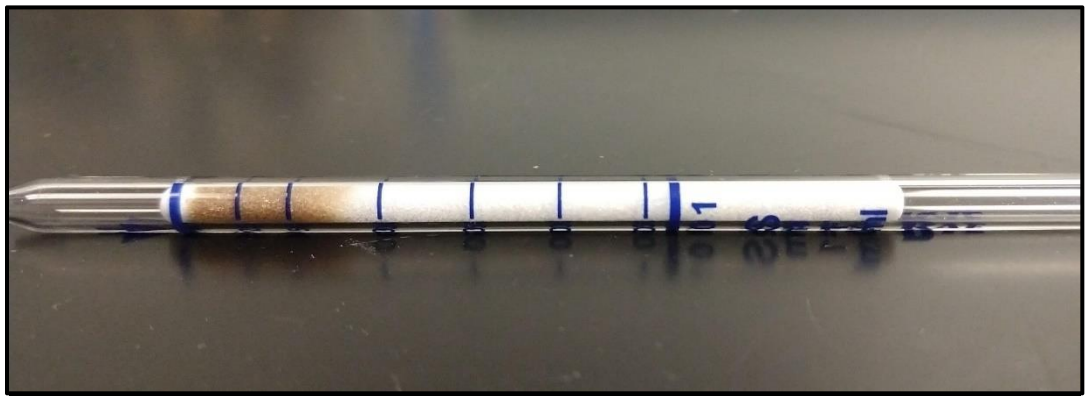

Figure 3.27: The RAE Systems gas detection tube measured the on-site H_2S content of Mahoning Landfill gas as 80 ppmv.

Previous research conducted by Feroze Khan demonstrated that landfill gas is a dynamic system, with the hydrogen sulfide concentration decreasing over time when the gas is stored in propane cylinders.[17] Therefore, the hydrogen sulfide content was retested on the day the button cell was operated on landfill gas. The landfill gas was sampled before the gas was fed through the H_2S scrubber (using sampling port #1 shown in Figure 2.10), and the results are given in Table 3.3 and Figure 3.28.

Table 3.3: H_2S content of Mahoning Landfill gas (pre-scrubber)

Range	2.5-50 ppmv
Number of Strokes	1
Sample Volume	100 mL
Sample Time	1 minute
Correction Factor	1
Tube Reading	Undetectable

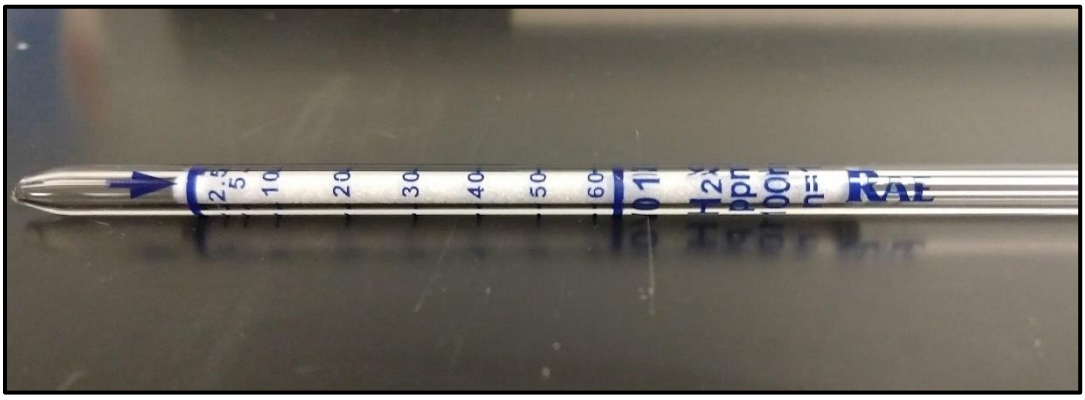

Figure 3.28: The 2.5-50 ppmv RAE Systems gas detection tube was unable to detect H_2S in the Mahoning Landfill gas after 1 day of storage in the propane cylinders.

Although the hydrogen sulfide content of the landfill gas prior to scrubbing was undetectable by the 2.5-50 ppmv gas detection tube, this does not guarantee the landfill gas is completely free of hydrogen sulfide. Rather, the H_2S concentration may be below the limit of detectability for this gas detection tube. Therefore, the chemisorbent filter remained in the experimental apparatus to remove any H_2S that may still be in the sample, but there was no need to perform a colorimetric analysis on the landfill gas exiting the filter.

Voltammetric Tests

Using the apparatus described in Figure 2.10 and the circuit shown in Figure 2.5, a button cell (Cell #6) was operated on 25 mL/min of landfill gas and 50 mL/minute of air. The temperature in the humidification flask was kept at 83°C (water vapor pressure = 401 torr) for a humidification level of 53%. Once a steady state had been established, the load box resistance was set to 99Ω, and current and voltage measurements were made every 15 minutes for a period of 6 hours. The voltammetric data for this experiment is shown in Figure 3.29.

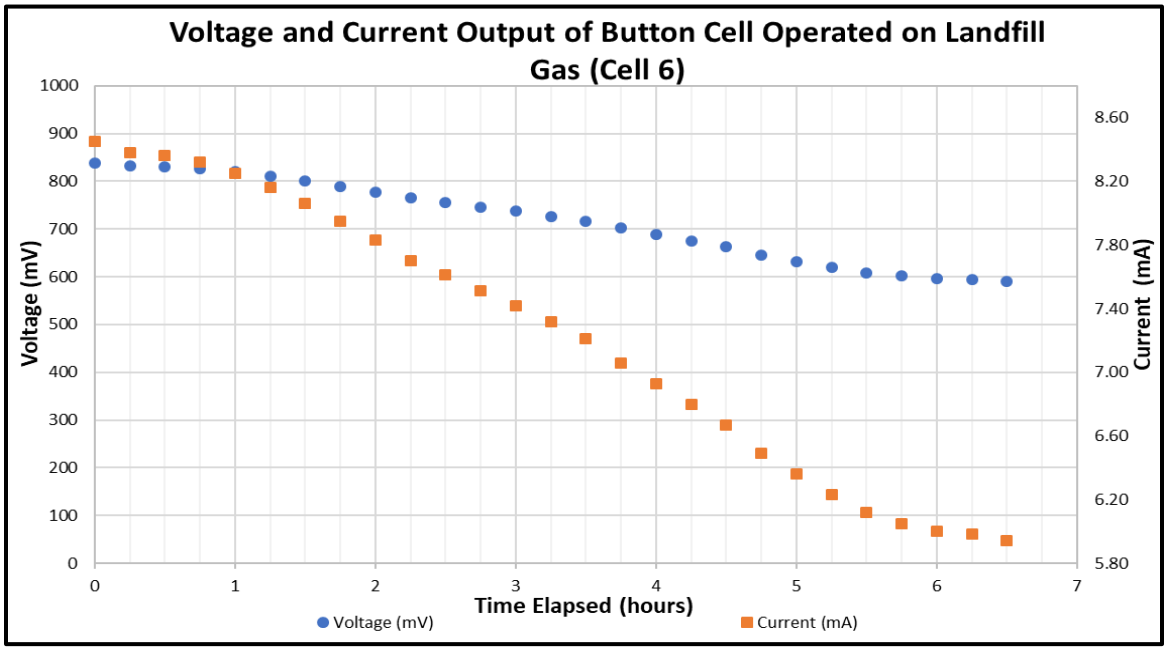

Figure 3.29: Voltage and current output of the Ni-YSZ/Hionic™/LSM button cell operated on 25 mL/min of humidified Mahoning Landfill gas and 50 mL/min of air.

Figure 3.29 shows a steady decline in voltage and current output over six and a half hours. Further data collection was abandoned because the cell cracked after approximately seven hours of operation. As seen with previous experiments using

humidified gas, the cracking was likely due to a buildup of condensed water vapor in the instrument. Unfortunately, unless modifications can be made to the ProboStat™ itself, this issue is unavoidable, as the base of the ProboStat™ maintains a temperature of approximately 70°C. This allows for condensation in the gas feedthrough tubes located in the base of the ProboStat™.

It is unclear what was responsible for the declining performance of Cell #6. Once the instrument was opened, there was no evidence of carbon deposition, which would be a clearly visible layer of soot. Furthermore, it is unlikely that the sub-parts-per-million levels of hydrogen sulfide remaining in the landfill gas would have passed through the chemisorbent filter as well as the water in the humidification flask, in which it is soluble. With carbon and hydrogen sulfide eliminated as the sources of anode inactivation, SEM and EDS analysis was used to investigate the cause of the loss in performance. This data is discussed in Section IV of this chapter.

To verify the results observed in the voltammetric experiment with Cell #6, the experiment was repeated with Cell #7, with two important modifications. First, nickel mesh was placed on the anode and silver mesh on the cathode to ensure an even distribution of current across the electrodes. The color gradient observed on Cell #6's anode could have resulted from the current being concentrated only in the area directly touching the platinum contact. Secondly, Cell #7 was reduced and allowed to come to a steady state under dry hydrogen before being operated on humidified Mahoning Landfill gas. The reasoning behind the second modification was two-fold. If the anode does indeed take a long time to become fully reduced and operational under landfill gas, pre-reducing with hydrogen accelerates this process, conserving the remaining supply of

landfill gas. Additionally, previous cells operated under hydrogen had a steady state voltage output of approximately 900 mV under a resistance of 99 Ω, so if Cell #7 behaves similarly, one can be assured that the cell itself is working as expected.

Cell #7 was reduced under a hydrogen flow of 50 mL/min and an air flow of 50 mL/min at 750°C. Once the cell reached a steady state at open circuit, the load resistance was decreased to 99 Ω, and the cell was allowed to stabilize again. The fuel gas was then changed to 25 mL/min of Mahoning Landfill gas, humidified with water vapor at 83°C. After an initial decline, the current and voltage output leveled off at approximately 510 mV and 5.20 mA, as shown in Figure 3.30.

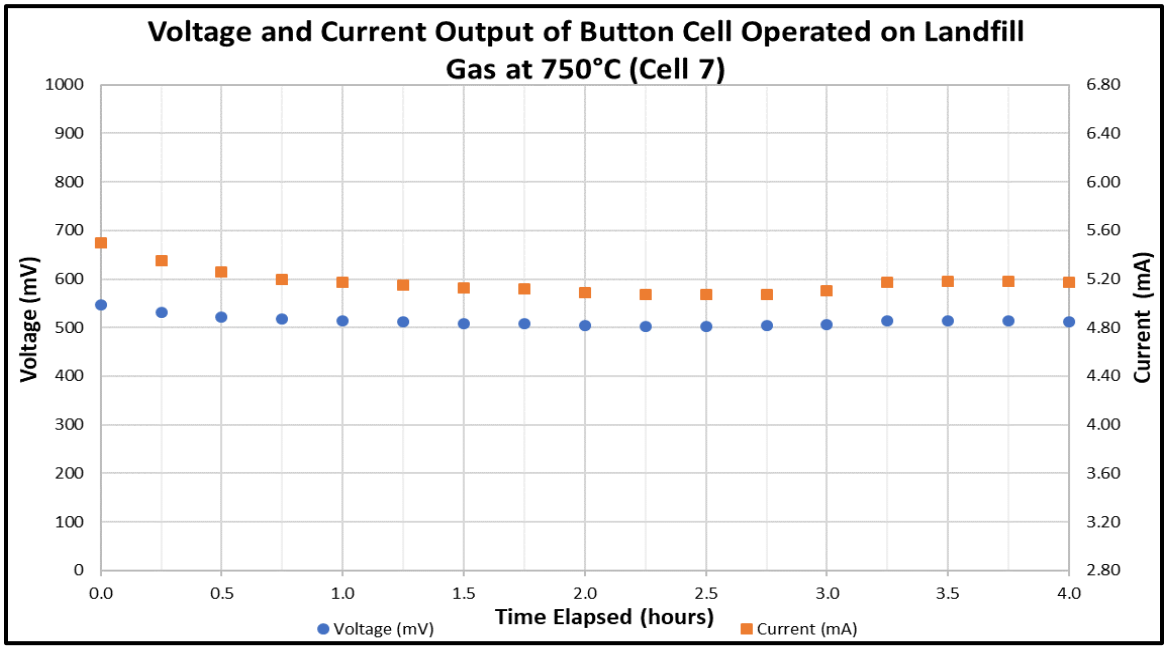

Figure 3.30: Voltage and current output of the Ni-YSZ/Hionic™/LSM button cell operated on 25 mL/min of humidified Mahoning Landfill gas and 50 mL/min of air at 750°C.

In comparison, cells operated on humidified methane reached a voltage of between 700 and 800 mV at a load of 99 Ω. To investigate if heavy hydrocarbons were affecting the

cell's performance, the operating temperature was increased to 900°C while all other conditions remained unchanged. The data collected under these conditions is shown in Figure 3.31.

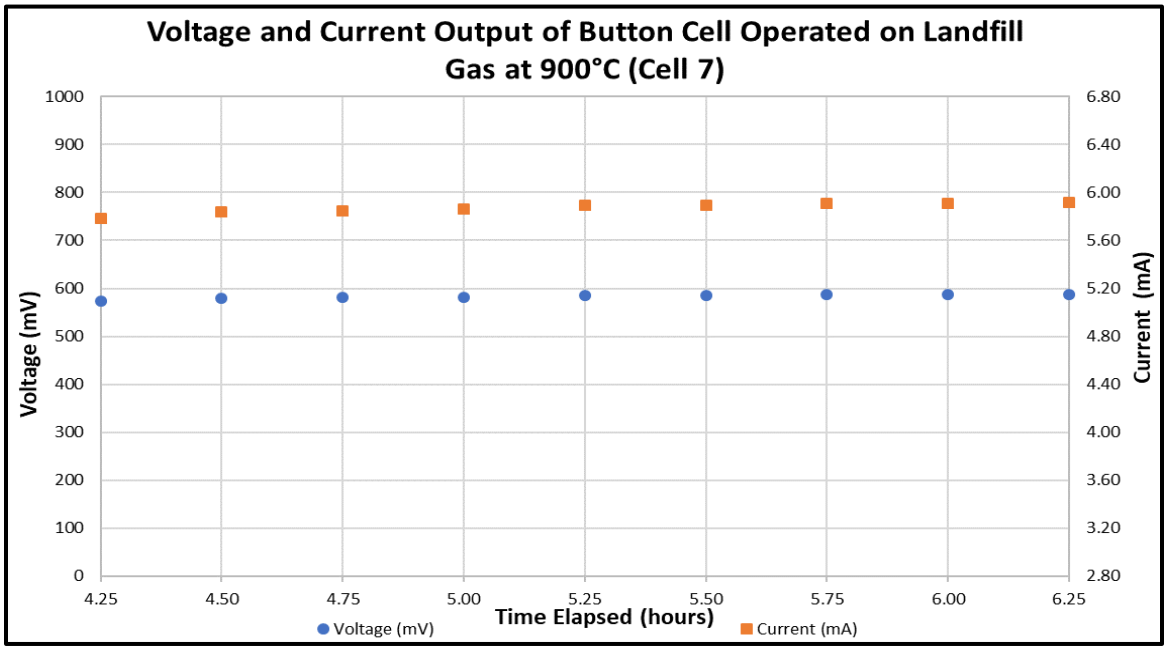

Figure 3.31: Voltage and current output of the Ni-YSZ/Hionic™/LSM button cell operated on 25 mL/min of humidified Mahoning Landfill gas and 50 mL/min of air at 900°C.

In the figure above, as the temperature was raised from 750°C to 900°C, the current and voltage output of the cell increased. This behavior is expected, as increasing the temperature decreases the resistivity of the electrolyte, and was also observed in a button cell operated on humidified methane (Figure 3.3). After an increase in performance compared to the same cell at 750°C, the voltage and current leveled off rather than continuing to increase. This suggests that heavy hydrocarbons were not responsible for the decreased performance: raising the temperature should have led to a complete recovery in cell function as carbon was burnt away. It appears that a material

other than carbon may have deposited on the anode, or that some component of landfill gas itself leads to lower outputs than cells operated on humidified methane. This hypothesis was tested by cooling the cell back to the standard operating temperature of 750°C, then switching the fuel gas from humidified landfill gas to hydrogen. The results are shown in Figure 3.32 and Figure 3.33.

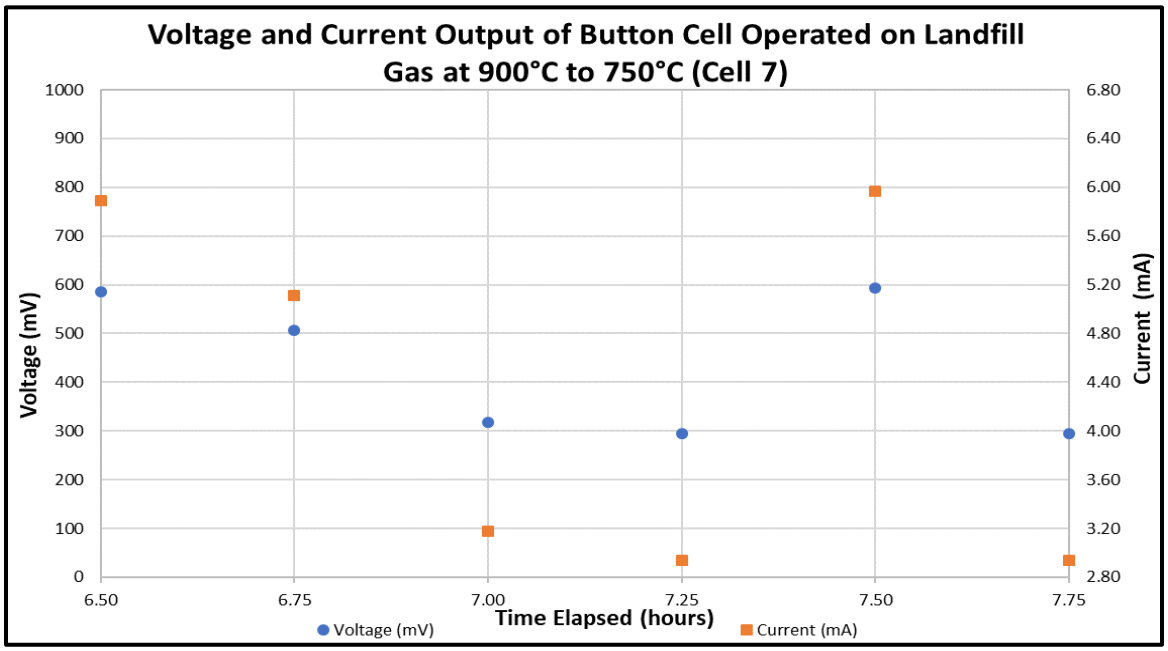

Figure 3.32: Voltage and current output of the Ni-YSZ/Hionic™/LSM button cell operated on 25 mL/min of humidified Mahoning Landfill gas and 50 mL/min of air as it cooled from 900°C to 750°C.

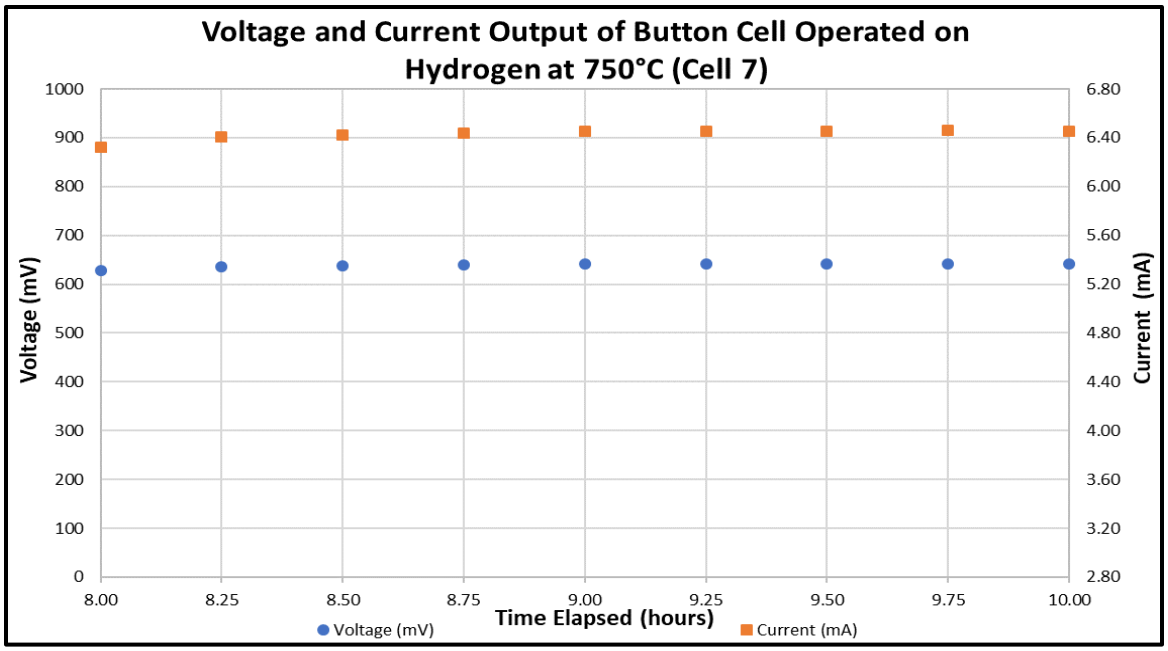

Figure 3.33: Voltage and current output of the Ni-YSZ/Hionic™/LSM button cell operated on 50 mL/min of H_2 and 50 mL/min of air at 750°C.

After the cell had cooled to 750°C, it was operated on 50 mL/min of hydrogen gas and showed a steady voltage and current output of approximately 640 mV and 6.45 mA. In comparison, a cell operated on hydrogen at a load of 99 Ω should have a voltage output of approximately 900 mV (Figure 3.23 and Figure 3.26). Figure 3.34 shows the changing voltage and current output of Cell #7 as the temperature and fuel gas conditions were varied during the experiment.

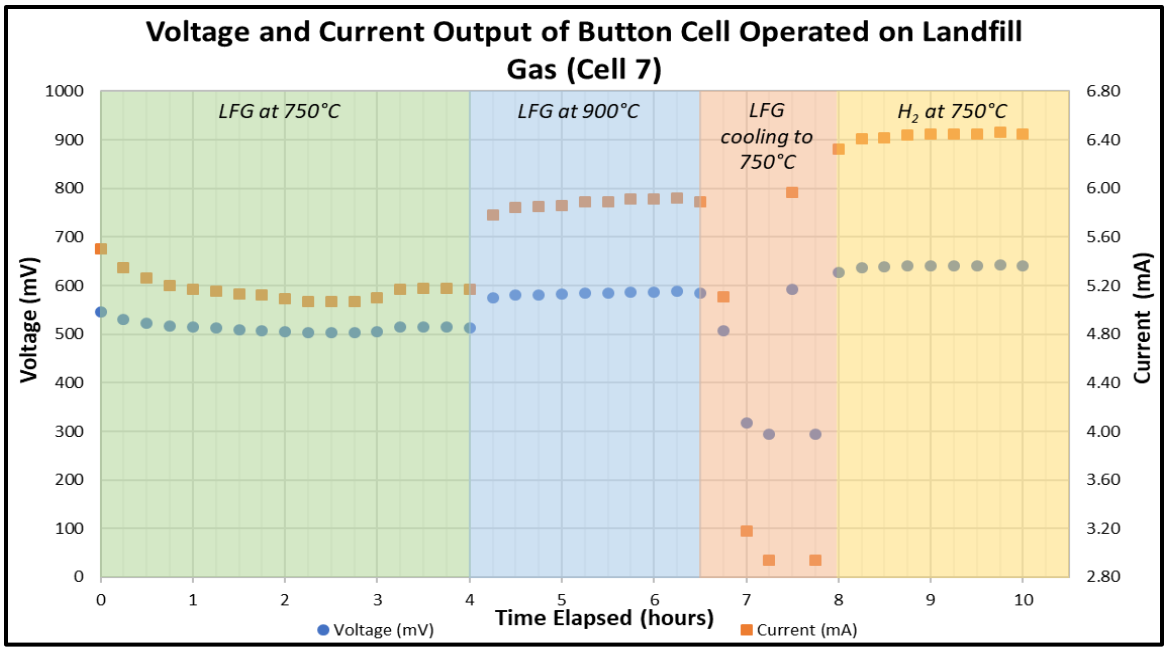

Figure 3.34: Voltage and current output of the Ni-YSZ/Hionic™/LSM button cell operated on humidified landfill gas at 750°C and 900°C, and H_2 at 750°C.

From the significantly worse performance observed in Cell #7, it is likely that a substance that cannot be removed by operating at higher temperatures or flowing hydrogen over the surface has deposited on the anode. This was examined using SEM and EDS, described in the next section.

PART IV: Anode Surface Analysis

Cells #3, #4, #5, #6, and #7, as well as an unused "blank" cell, were examined using a scanning electron microscope equipped with an EDS probe. Secondary electron imaging was used to study differences in the anode surface of the cells contaminated with D5 compared to the blank cell. EDS identified the atoms present on the anode, with the presence of silicon being the most important in confirming silica deposition.

Blank Cell

Figure 3.35 is an image of the blank cell's anode at 75x magnification. This cell was used as the baseline for identifying contaminants on the anodes of Cells #3, #4, #5, #6, and #7, as this cell was never operated.

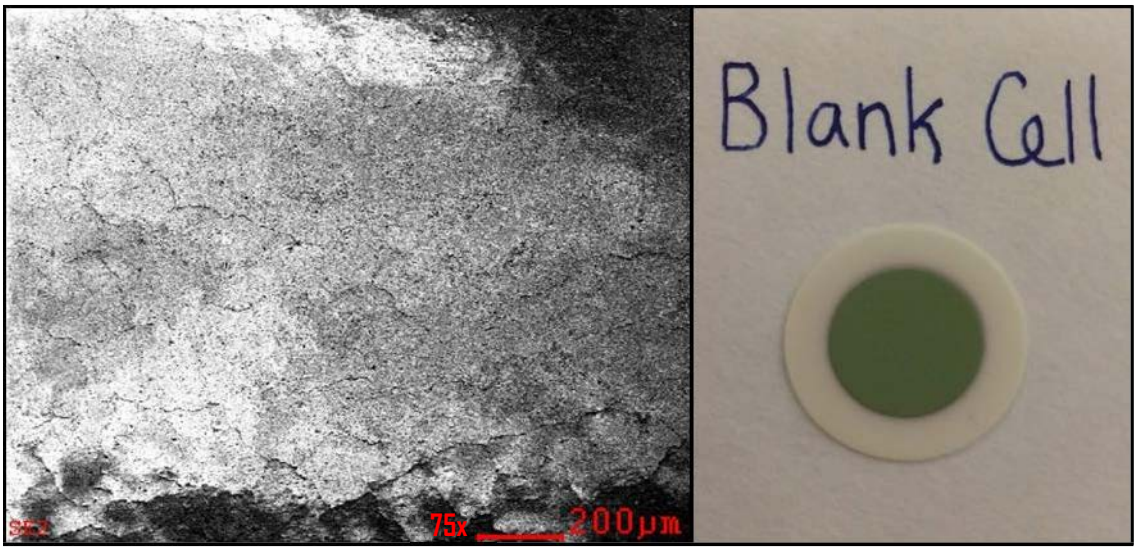

Figure 3.35: SEM image of the blank cell's anode at 75x magnification (left) and a picture showing the appearance of the cell (right)

The SEM image does not show any immediately identifiable features. Note that the anode of the blank cell is unblemished and light green in color. Figure 3.36 is the EDS spectrum of the area shown in the SEM image above, and Table 3.4 gives the atoms present in the spectrum as both weight and atomic percentages.

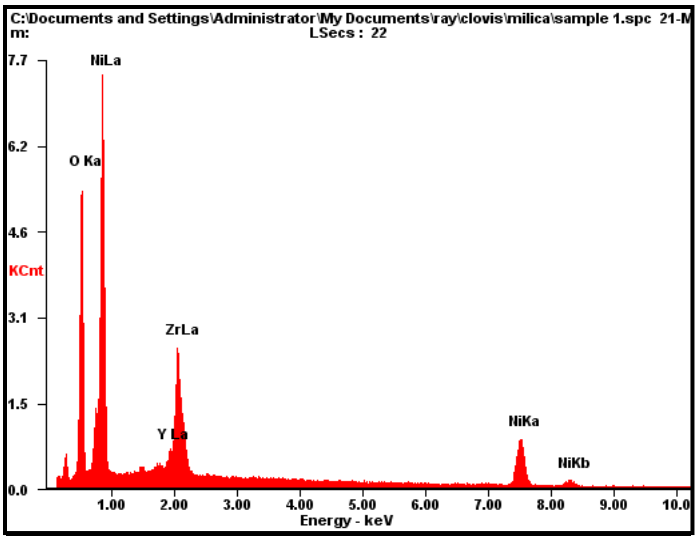

Figure 3.36: EDS spectrum of the blank cell anode (75x magnification)

Table 3.4: Weight and atomic percentages of elements in EDS spectrum of the blank cell anode (75x magnification)

Element	Weight %	Atom %
O_K	40	74
Y_L	4	1
Zr_L	22	7
Ni_K	35	18
Matrix Correction		*ZAF*

As expected for the Ni-YSZ anode, EDS analysis identified the presence of oxygen, nickel, zirconium, and yttrium. Because oxygen is a component of nickel (II) oxide, zirconium (II) oxide, and yttrium (III) oxide, it makes sense that oxygen is the most abundant atom. Additionally, because YSZ contains only 8 mol% yttrium (III) oxide, the least abundant atom found was yttrium. Fuel Cell Materials does not disclose the exact mass composition of their Ni-YSZ anodes; instead, their material safety data sheet gives the weight percent of their Ni-YSZ cermet as 50-80% NiO and 20-50% YSZ.[42]

Because the exact composition of the fuel cells is not known, the SEM/EDS experiments were conducted without a true standard, placing limitations on the weight and atomic percentages reported by the EDS software. In the absence of reliable standards, EDS was used as a qualitative technique to detect the presence of certain atoms rather than to quantify how much of each atom is present on the anode surface. Therefore, the weight and atomic percentages should be considered as relative instead of absolute values. To reflect these limitations and avoid implying a greater level of accuracy than achieved, these values were rounded to the nearest whole number rather than reported to two decimal places, which is the instrument's default setting. For reported values of less than 1%, the designation "<1" was used.

Cell #3

Recall that Cell #3 was operated on 50 mL/min of humidified CH_4 and 100 mL/min of air. The fuel gas was spiked with D5 in increasing concentrations of 1, 5, 10, and 100 ppmv. After approximately 8 total hours of operation (see Figure 3.15 and Figure 3.16), there was no decline in voltage and current output. Figure 3.37 is an SEM image of Cell #3's anode at 75x magnification.

Figure 3.37: SEM image of Cell #3's anode at 75x magnification (left) and a picture showing the appearance of the cell (right)

Compared to that of the blank cell, the SEM image of Cell #3's anode suggests that material has been deposited. Additionally, the anode has changed color from light green to black. Information about the identity of the deposit is given in Figure 3.38.

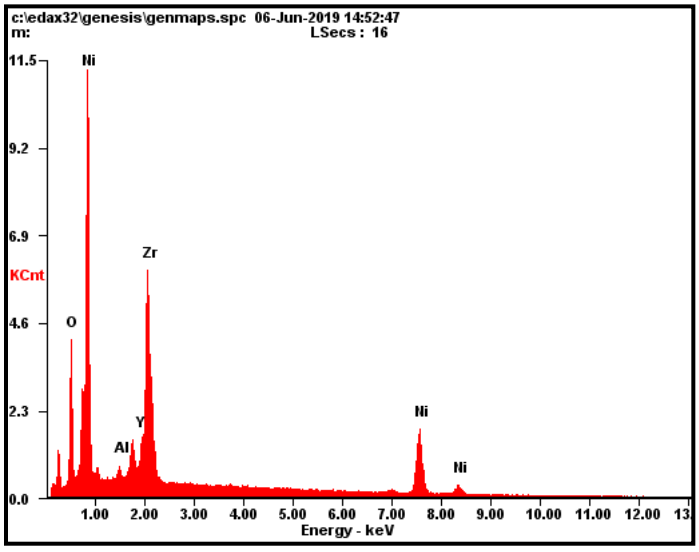

Figure 3.38: EDS spectrum of the Cell #3 anode (75x magnification)

The EDS spectrum of Cell #3 shows the appearance of a new peak, corresponding to aluminum. Table 3.5 shows the quantities of the elements present in the sample.

Table 3.5: Weight and atomic percentages of elements in EDS spectrum of the Cell #3 anode (75x magnification)

Element	Weight %	Atom %
O_K	22	42
Al_K	<1	10
Y_L	6	2
Zr_L	32	10
Ni_K	40	37
Matrix Correction		*ZAF*

According to EDS analysis, the anode of Cell #3 contains a small amount of aluminum. With the reported atomic percentage of aluminum being approximately 1%, it is difficult to say with certainty that the element is actually present in the sample. For this reason, EDS was used to generate elemental maps for each element detected in the sample. In the elemental map, spots represent the distribution and intensity of signals for an element in the scanned area, with bright spots representing a strong signal. Figure 3.39 is the elemental map for the elements EDS detected in Cell #3.

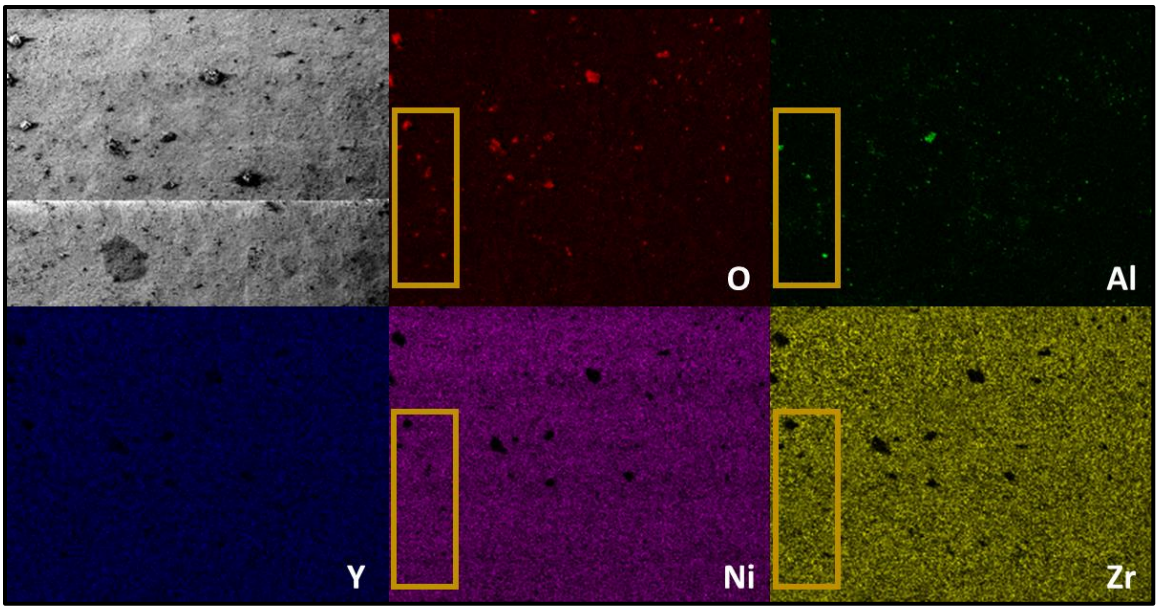

Figure 3.39: EDS elemental map for Cell #3 at 75x magnification; the highlighted regions show that strong signals for O and Al correspond to an absence of signals for Ni and Zr (Y is more difficult to see, so it was not included).

The elemental map for Cell #3 shows that other than a few spots, oxygen, yttrium, nickel, and zirconium are evenly distributed. Aluminum signals, on the other hand, appear less intense and more scattered. The boxes in Figure 3.39 are used to highlight a collection of strong aluminum signals corresponding to strong oxygen signals in the same area. Furthermore, this same area shows an absence of nickel and zirconium signals, suggesting that aluminum oxide may have deposited on the anode surface. The MSDS for the button cells states that the cell may contain up to 1% aluminum oxide by weight, likely as a sintering aid,[43] so this could be the reason for an aluminum signal.

Another important feature of the EDS data for Cell #3 is the lack of silicon, despite the fuel gas (humidified methane) being spiked with as much as 100 ppmv of D5. This, along with the constant voltage output shown in Figure 3.15 and Figure 3.16, indicates that silica was not deposited on the anode. Instead, the water content of the fuel

gas and the high temperatures inside the ProboStat™ led the siloxane to decompose before reaching the anode. This is supported by the presence of crystalline silica on the gas-directing quartz tube (Figure 3.17 and Figure 3.18) and on the outer alumina tube of the ProboStat™.

Cell #4

Cell #4 was operated on 50 mL/min of hydrogen and 50 mL/min of air and allowed to reach a steady state at a load of 99 Ω. The hydrogen gas was then spiked with 1 ppmv D5 and later 5 ppmv D5, and after 6 hours, the cell experienced a 10% decrease in voltage output. Figure 3.40 is an SEM image of the anode of Cell #4 at 75x magnification. The photograph of the cell itself shows that the anode is a dirty green color.

Figure 3.40: SEM image of Cell #4's anode at 75x magnification (left) and a picture showing the appearance of the cell (right)

Figure 3.41 and Table 3.6 give the EDS results for Cell #4.

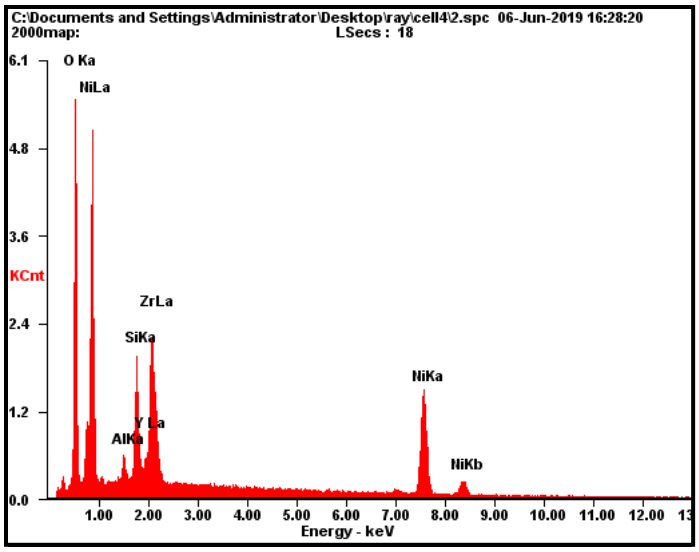

Figure 3.41: EDS spectrum of the Cell #4 anode (75x magnification)

Table 3.6: Weight and atomic percentages of elements in EDS spectrum of the Cell #4 anode (75x magnification)

Element	Weight %	Atom %
O_K	30	61
Al_K	1	1
Si_K	6	7
Y_L	2	1
Zr_L	17	6
Ni_K	43	24
Matrix Correction		*ZAF*

The spectrum for Cell #4 shows the appearance of a silicon peak. EDS also gave the atom percentage of silicon as higher than that of yttrium and zirconium, which are known to be present in the anode. This, along with the decline in voltage output, is strong evidence for the presence of silicon in the sample. Cell #5 was operated under similar conditions as

Cell #4 and showed a greater decline in voltage output, so Cell #5 was chosen for a more thorough analysis of silicon deposition.

Cell #5

Cell #5 was operated on 50 mL/min of hydrogen and 50 mL/min of air and allowed to reach a steady state at a load of 99 Ω. The hydrogen gas was then spiked with 10 ppmv D5, and the cell's voltage output decreased by 13% after 6 hours. Figure 3.42 is an SEM image of the anode of Cell #5 at 75x magnification. The photograph of the cell itself shows that the anode has become gray.

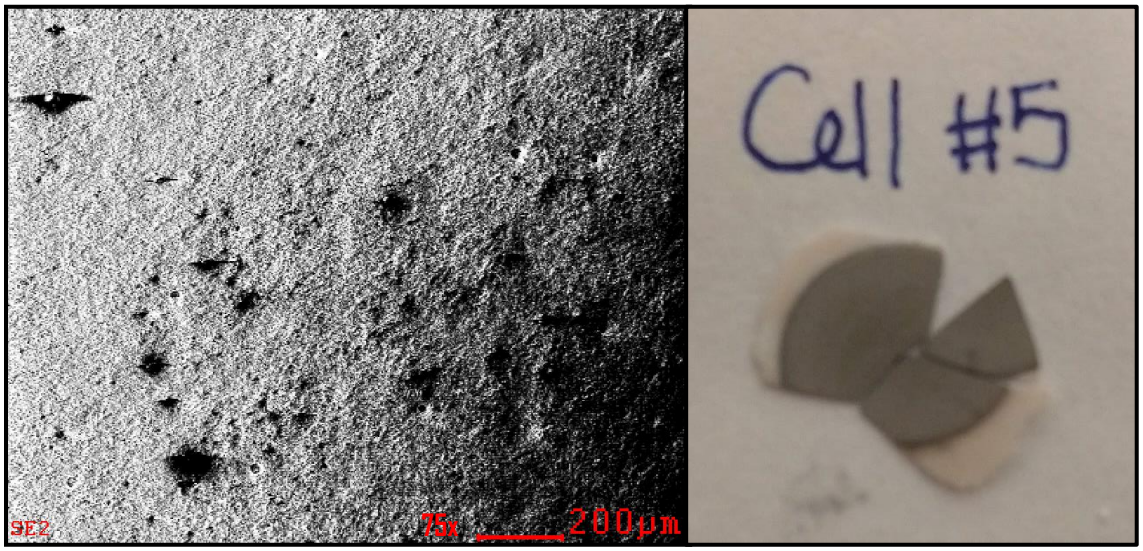

Figure 3.42: SEM image of Cell #5's anode at 75x magnification (left) and a picture showing the appearance of the cell (right)

The EDS results for Cell #5 are reported in Figure 3.43 and Table 3.7.

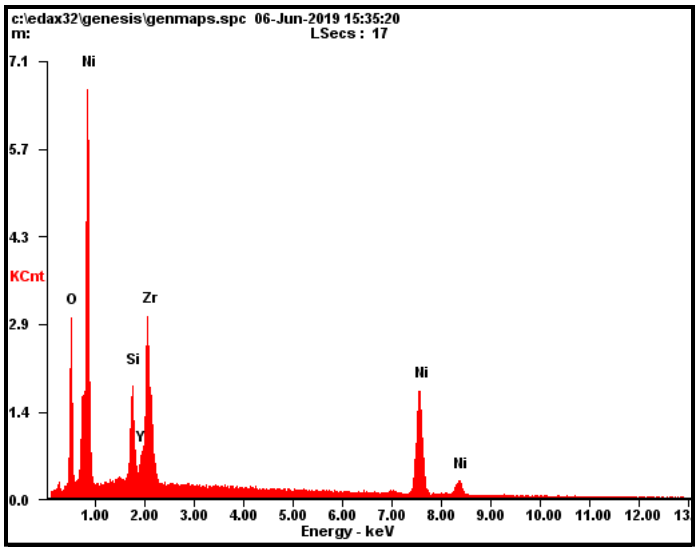

Figure 3.43: EDS spectrum of the Cell #5 anode (75x magnification)

Table 3.7: Weight and atomic percentages of elements in EDS spectrum of the Cell #5 anode (75x magnification)

Element	Weight %	Atom %
O_K	17	43
Si_K	6	9
Y_L	4	2
Zr_L	22	10
Ni_K	52	37
Matrix Correction		*ZAF*

In the EDS spectrum for Cell #5, the aluminum peak is not as sharp as the one in the Cell #4 spectrum and gave only trace amounts of aluminum. For this reason, the aluminum peak was not counted, as it was difficult to discern from background noise. The scattered and weak nature of the aluminum signals, shown in the EDS elemental map in Figure 3.44, validates the choice to omit aluminum from the spectrum. The silicon

signal was comparable to that of Cell #4, and the maps in Figure 3.44 give evidence of silica deposition on the sample surface.

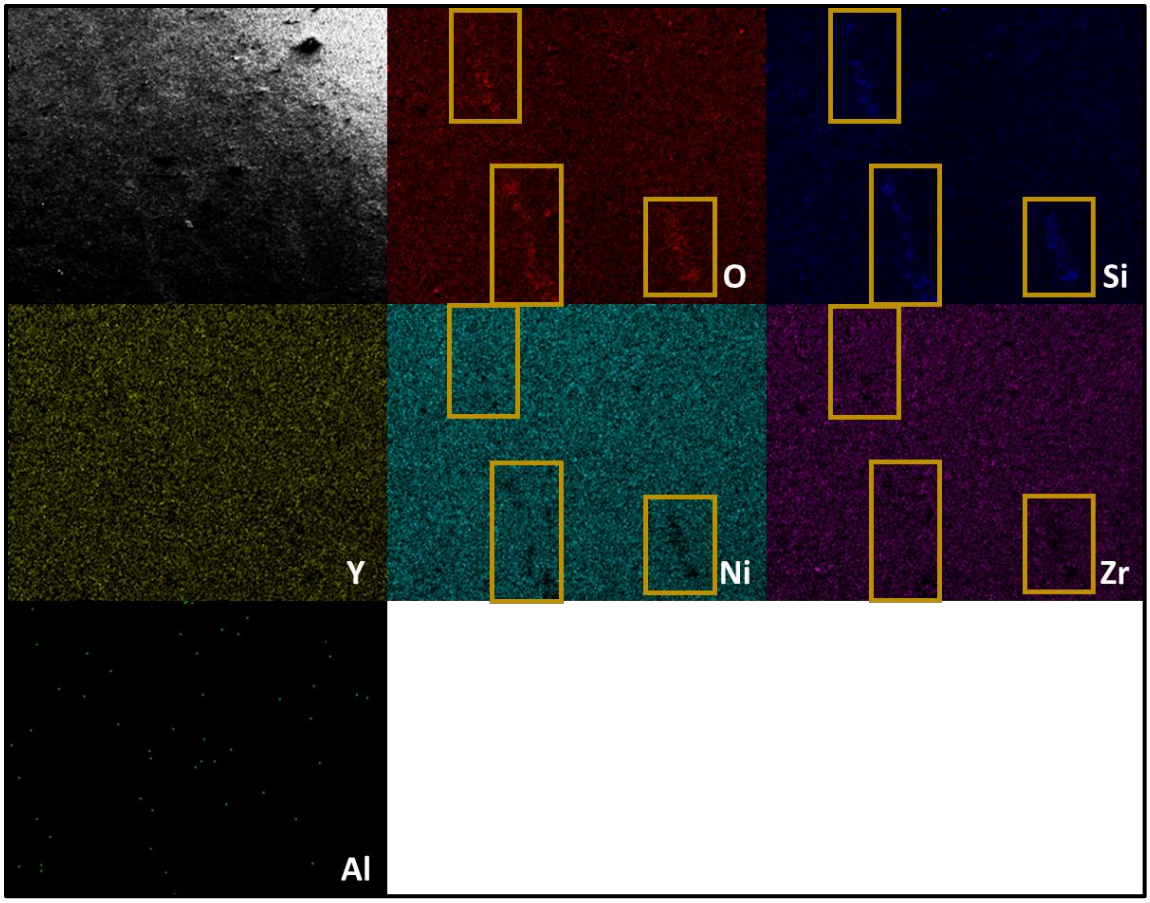

Figure 3.44: EDS elemental map for Cell #5 at 75x magnification; the highlighted regions show that strong signals for O and Si correspond to an absence of signals for Ni and Zr (Y is more difficult to see, so it was not included).

The elemental map in Figure 3.44 shows strong signals for oxygen and silicon in the same regions of the sample. The strong oxygen and silicon signals also correspond to an absence of nickel and zirconium signals. Based on these distributions, it is likely that silica has deposited on the anode surface. From the maps, it appears the silica has deposited as streaks on the anode. This was examined at a higher magnification. Focusing

in on one of the areas with high silicon signal density at 500x magnification produced the SEM image and EDS spectrum shown in Figure 3.45 and Figure 3.46.

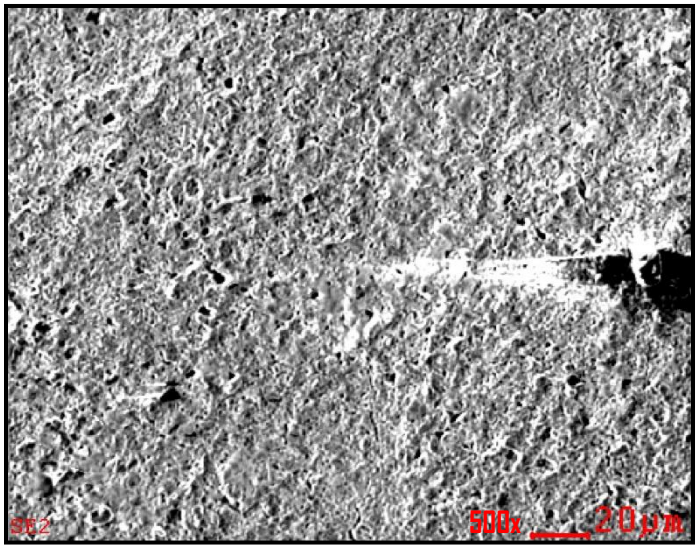

Figure 3.45: SEM image of Cell #5's anode at 500x magnification

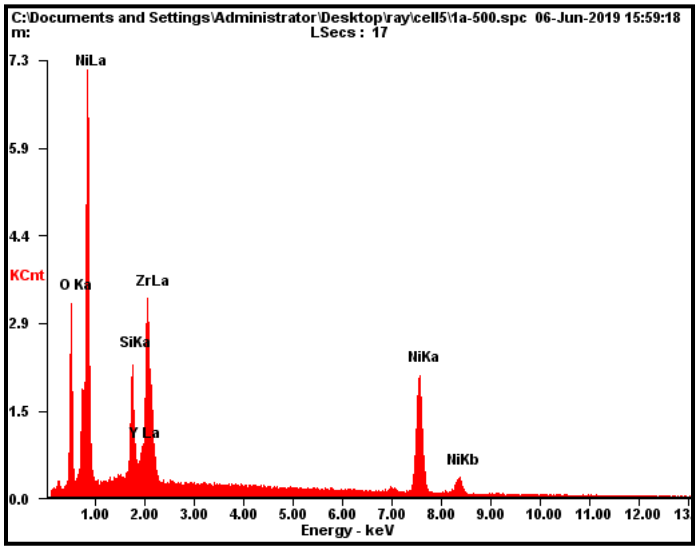

Figure 3.46: EDS spectrum of the Cell #5 anode (500x magnification)

The quantities in which the elements were detected by EDS are given in Table 3.8.

Table 3.8: Weight and atomic percentages of elements in EDS spectrum of the Cell #5 anode (500x magnification)

Element	Weight %	Atom %
O_K	16	42
Si_K	6	10
Y_L	3	2
Zr_L	22	10
Ni_K	52	37
Matrix Correction		*ZAF*

The sample area examined at 500x magnification has a very similar composition to the larger section that was examined at 75x magnification. The distributions of signals for the reported elements are shown in the maps in Figure 3.47.

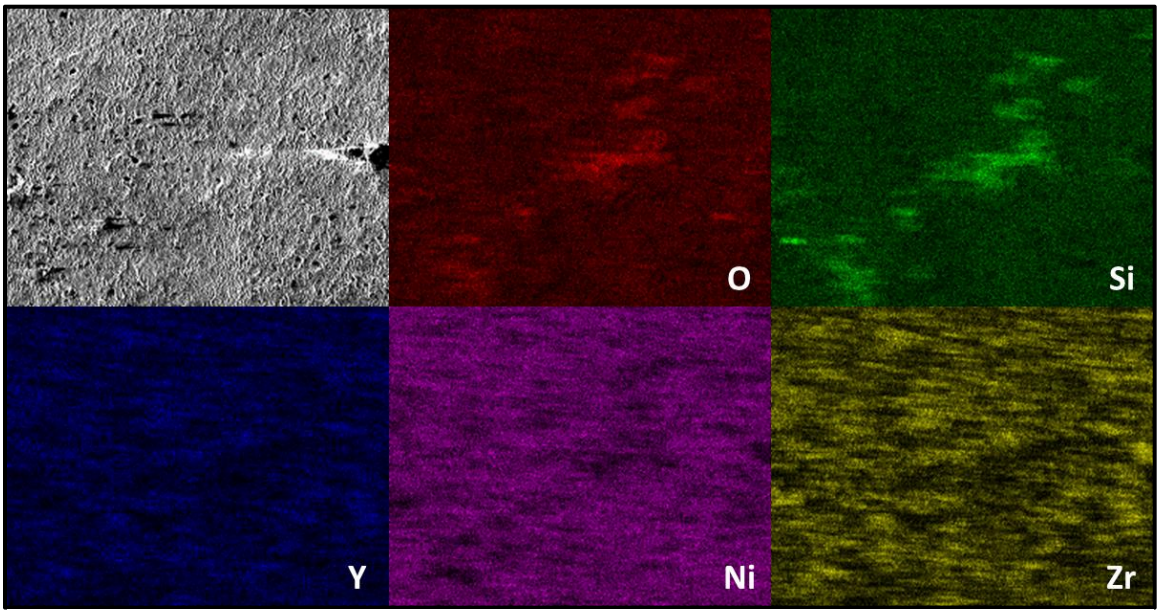

Figure 3.47: EDS elemental map for Cell #5 at 500x magnification; note the corresponding areas of high signal density in the O and Si maps. This also matches areas of low signal density in the Ni map.

Again, the maps indicate silica deposition, as the regions with strong oxygen signals overlap the regions with strong silicon signals. In the oxygen and silicon maps, these areas of high signal density run diagonally across the image, from the bottom left corner to the top right. As with the maps in Figure 3.44, these regions correspond to dark areas on the nickel map, meaning that nickel signals were not received from those specific areas. This is consistent with a deposit, in this case silica, building up on the anode surface. The yttrium and zirconium maps are expected to show the same dark areas as the nickel map, but they are not as easy to see. Another analysis was performed at 2000x magnification to confirm this. The image and EDS spectrum at 2000x magnification are shown in Figure 3.48 and Figure 3.49.

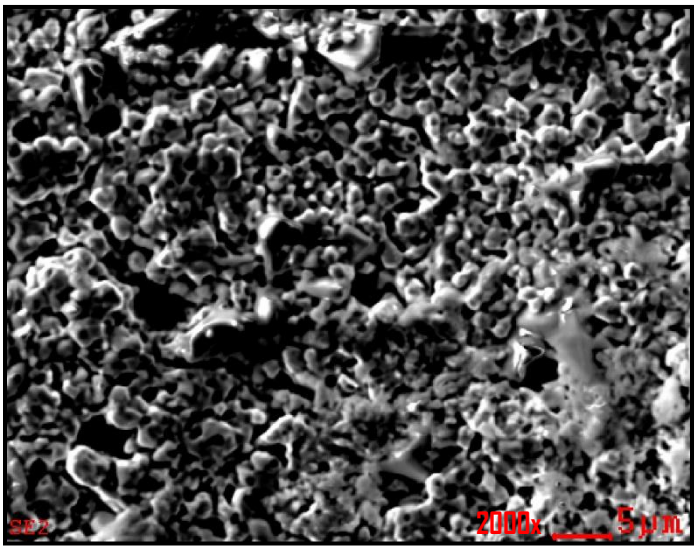

Figure 3.48: SEM image of Cell #5's anode at 2000x magnification

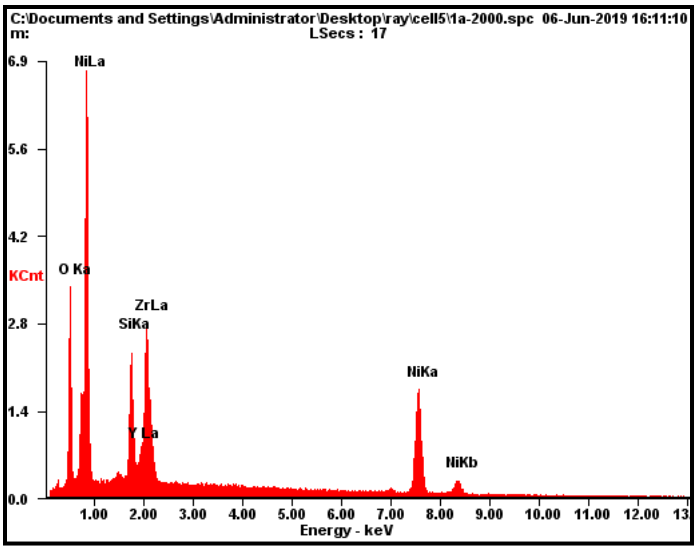

Figure 3.49: EDS spectrum of the Cell #5 anode (2000x magnification)

Table 3.9 quantifies the elements present in this region of the sample.

Table 3.9: Weight and atomic percentages of elements in EDS spectrum of the Cell #5 anode (2000x magnification)

Element	Weight %	Atom %
O_K	16	42
Si_K	6	10
Y_L	3	2
Zr_L	22	10
Ni_K	52	37
Matrix Correction		*ZAF*

The EDS analysis at 2000x magnification shows that silicon is present in the sample, and the sample composition has remained close to the values reported at 75x magnification and 500x magnification. Figure 3.50 is the EDS elemental map of Cell #5 at 2000x magnification, showing additional evidence of silica deposition.

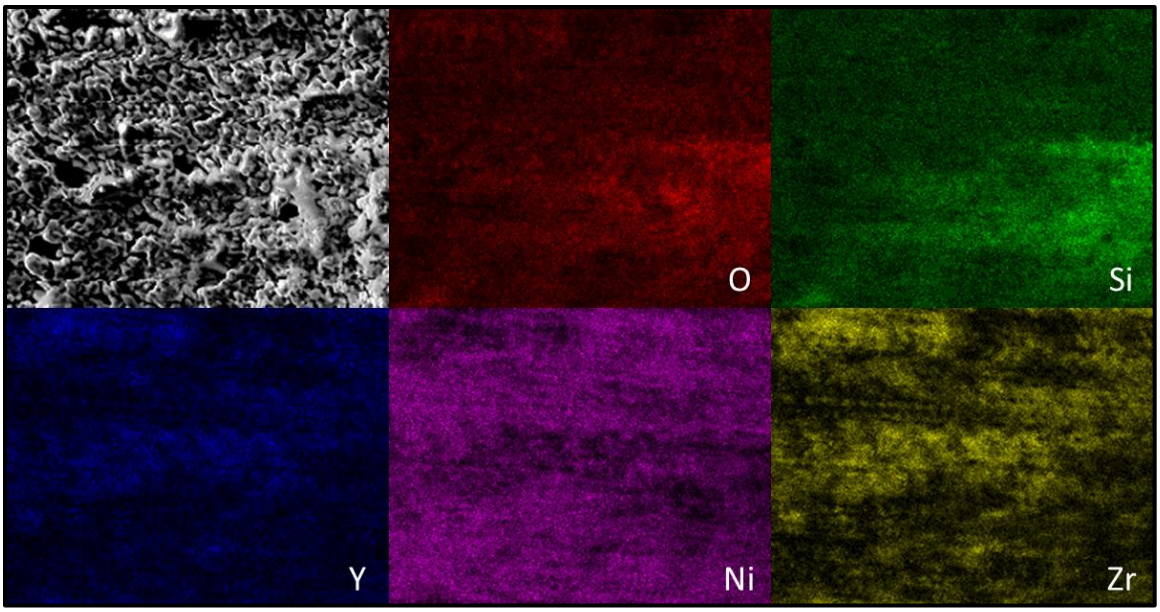

Figure 3.50: EDS elemental map for Cell #5 at 2000x magnification; clusters of high signal density in the O map match those in the Si map. This also matches areas of low signal density in the Ni map.

The maps in Figure 3.50 once more show evidence of silica deposition, with the bright areas on the right side of the oxygen map matching those on the silicon map. At this magnification, it is also possible to see the distribution of yttrium and zirconium, which are the other major components of the anode in the form of yttria-stabilized zirconia. Areas with strong signals for yttrium and zirconium correspond to areas where the nickel signals are sparser. This shows that the anode is indeed comprised of nickel (II) oxide and yttria-stabilized zirconia, though the distribution of these metal oxides does not appear uniform throughout the anode. The cluster map in Figure 3.51 shows the distribution of three different oxides on the anode surface.

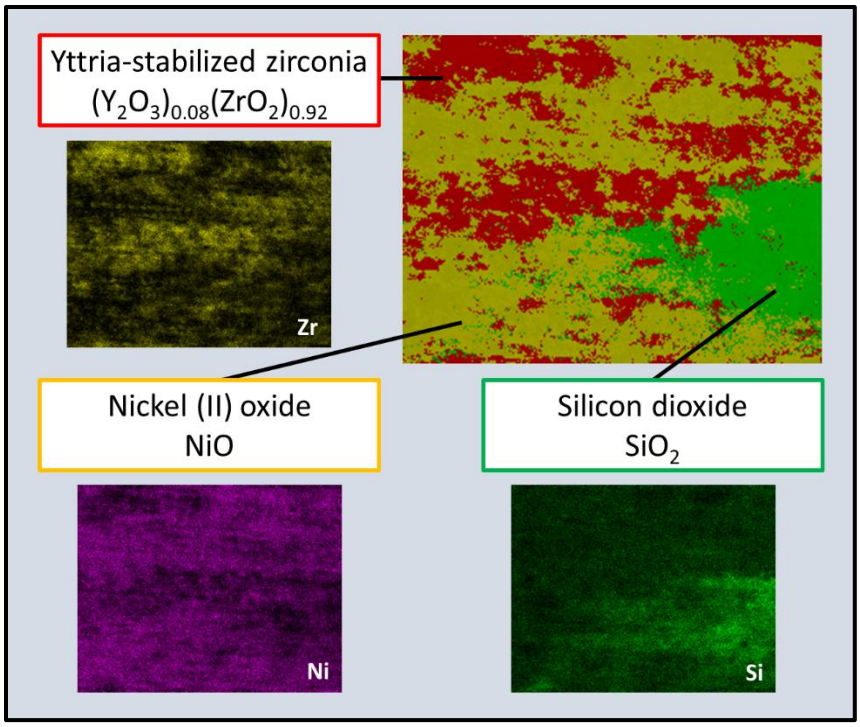

Figure 3.51: EDS cluster map for Cell #5 at 2000x magnification; each of the three clusters identified contains oxygen.

The EDS software generates the cluster map by combining overlapping element signals, indicating that the elements are forming a compound. In each of the three clusters shown in the map in Figure 3.51, oxygen is present, so each cluster is an oxide. Based on the location of high signal density in the silicon map (Figure 3.50), the cluster shown in green is silica. Note that the location of this cluster corresponds to areas of fewer signals for yttrium, nickel, and zirconium. Areas with strong nickel signals match up with areas of weak yttrium and zirconium signals, indicating that the cluster shown in yellow is nickel (II) oxide. Finally, strong yttrium signals correspond to strong zirconium signals, indicating that the third cluster, shown in red, is yttria-stabilized zirconia.

Based on the EDS spectra and elemental maps for the anode of Cell #5, deposited silica was the compound responsible for the observed decline in voltage output. Cell #4,

which experienced a comparable voltage decrease, also had silicon detected on the anode. The high-temperature deposition of silica occurred when D5 reacted with water produced at the anode of the cell.

Cell #6

Cell #6 was operated on 25 mL/min of humidified Mahoning Landfill gas and 50 mL/min of air at a load of 99 Ω. During the 6 hours of operation before the cell cracked, the voltage and current output steadily declined. Figure 3.52 is an SEM image of the anode of Cell #6 at 75x magnification. The photograph of the cell itself shows that the anode has a color gradient across its surface, possibly due to uneven current distribution.

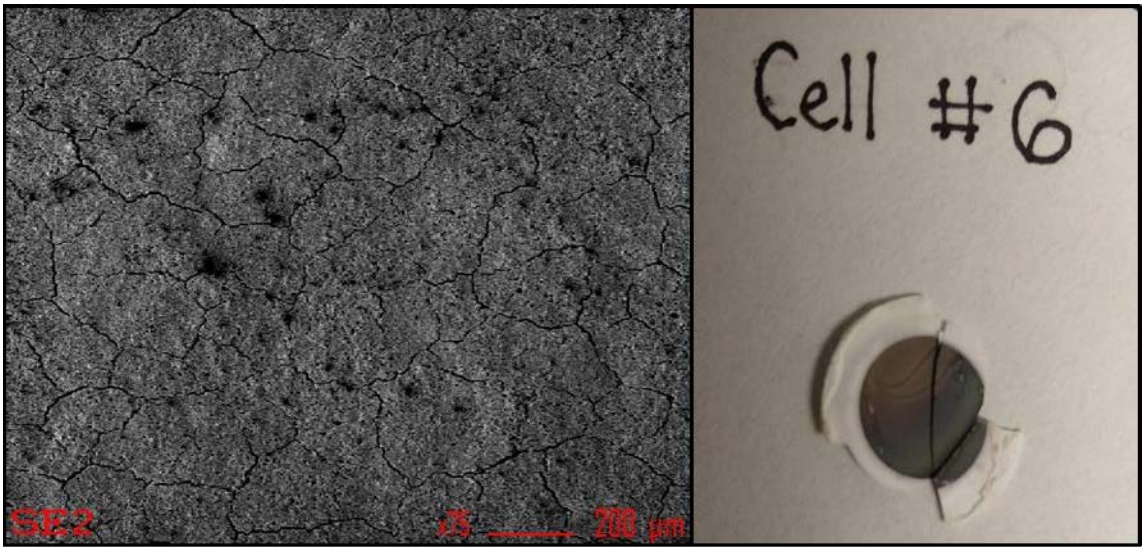

Figure 3.52: SEM image of Cell #6's anode at 75x magnification (left) and a picture showing the appearance of the cell (right); note the color gradient across the anode.

The EDS results for Cell #6 are reported in Figure 3.53 and Table 3.10.

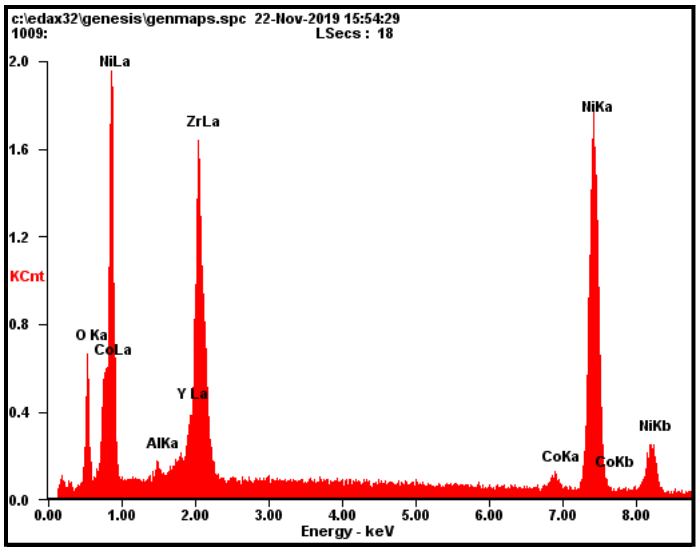

Figure 3.53: EDS spectrum of the Cell #6 anode (75x magnification)

Table 3.10: Weight and atomic percentages of elements in EDS spectrum of the Cell #6 anode (75x magnification)

Element	Weight %	Atom %
O_K	12	37
Al_K	<1	1
Y_L	5	3
Zr_L	28	15
Co_K	2	2
Ni_K	53	43
Matrix Correction		*ZAF*

The EDS data shown above does not provide an explanation for the cell's decline in performance; although small amounts of aluminum and cobalt were detected, they are components of the cell anode, according to the MSDS for the Ni-YSZ/Hionic™/LSM button cell.[43] A second analysis was performed at a magnification of 500x, the results of which are shown in Figure 3.54 and Figure 3.55.

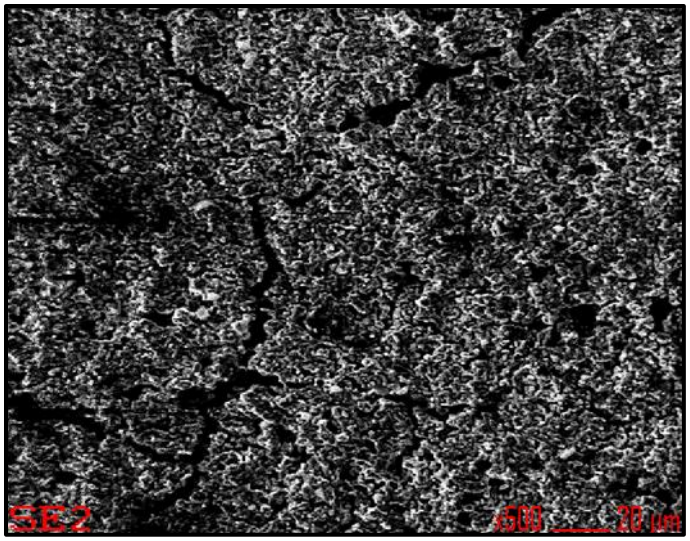

Figure 3.54: SEM image of Cell #6's anode at 500x magnification

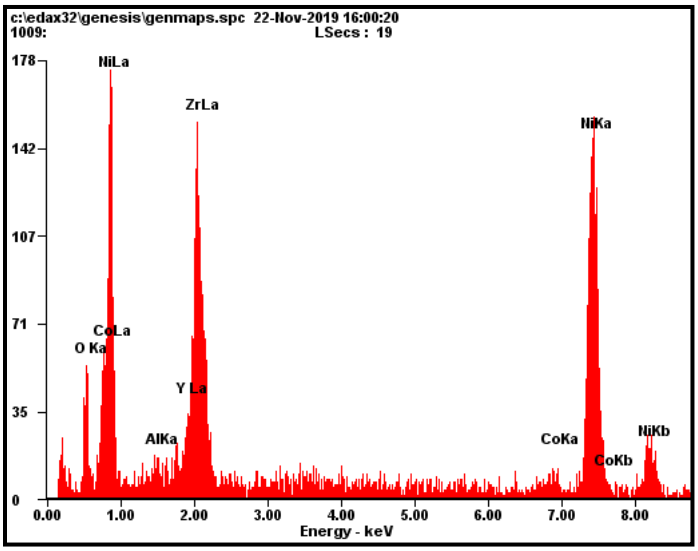

Figure 3.55: EDS spectrum of the Cell #6 anode (500x magnification)

The elements detected in Figure 3.55 are quantified in Table 3.11.

Table 3.11: Weight and atomic percentages of elements in EDS spectrum of the Cell #6 anode (500x magnification)

Element	Weight %	Atom %
O_K	12	37
Al_K	1	2
Y_L	6	3
Zr_L	27	14
Co_K	3	3
Ni_K	51	42
Matrix Correction		*ZAF*

As with the previous analysis, the EDS probe did not find evidence of deposits that could be responsible for the cell's decline in voltage and current output. A third analysis was performed at 2000x magnification, shown in Figure 3.56 and Figure 3.57. The quantities of each element detected are given in Table 3.12.

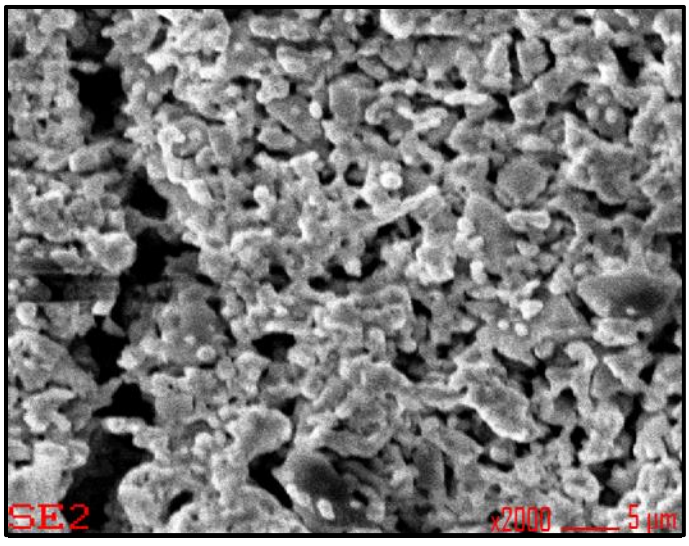

Figure 3.56: SEM image of Cell #6's anode at 2000x magnification

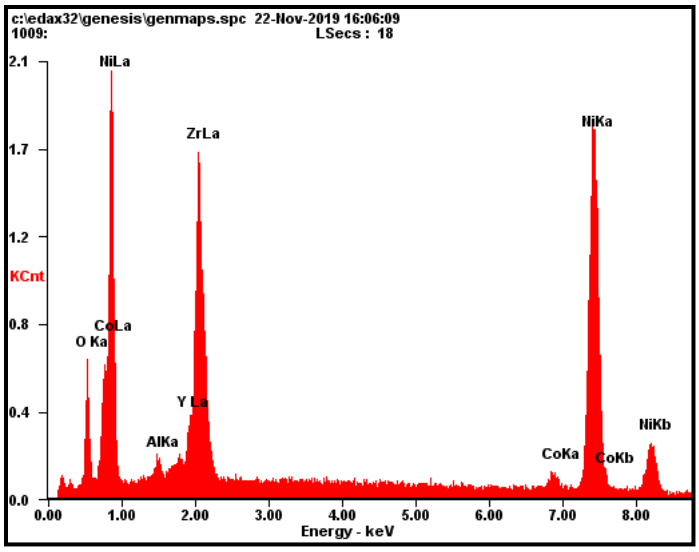

Figure 3.57: EDS spectrum of the Cell #6 anode (2000x magnification)

Table 3.12: Weight and atomic percentages of elements in EDS spectrum of the Cell #6 anode (2000x magnification)

Element	Weight %	Atom %
O_K	12	36
Al_K	1	2
Y_L	5	3
Zr_L	27	14
Co_K	2	2
Ni_K	52	43
Matrix Correction		*ZAF*

SEM and EDS analysis of Cell #6 did not explain the cause of the cell's decreasing performance over the six hours that data was collected. The elemental composition of the anode remained consistent across the different magnification levels, reinforcing the reliability of the results. It is possible that the lower voltage and current outputs of Cell #6, when compared to cells operated on humidified methane under the

same load, are due to landfill gas not being as fuel rich as pure methane. Additionally, the steadily decreasing outputs may represent the cell taking an unexpectedly long time to reach a steady state.

Cell #7

Cell #7 was reduced under hydrogen before it was operated on 25 mL/min of Mahoning Landfill gas and 50 mL/min of air at 750°C. After the voltage and current declined under these conditions, the temperature was increased to 900°C to test if carbon deposition was responsible for the performance loss. Because the outputs did not continue to increase, the operating temperature was restored to 750°C, and the fuel gas was switched to 50 mL/min of hydrogen. A photograph and micrograph of Cell #7's anode is shown in Figure 3.58.

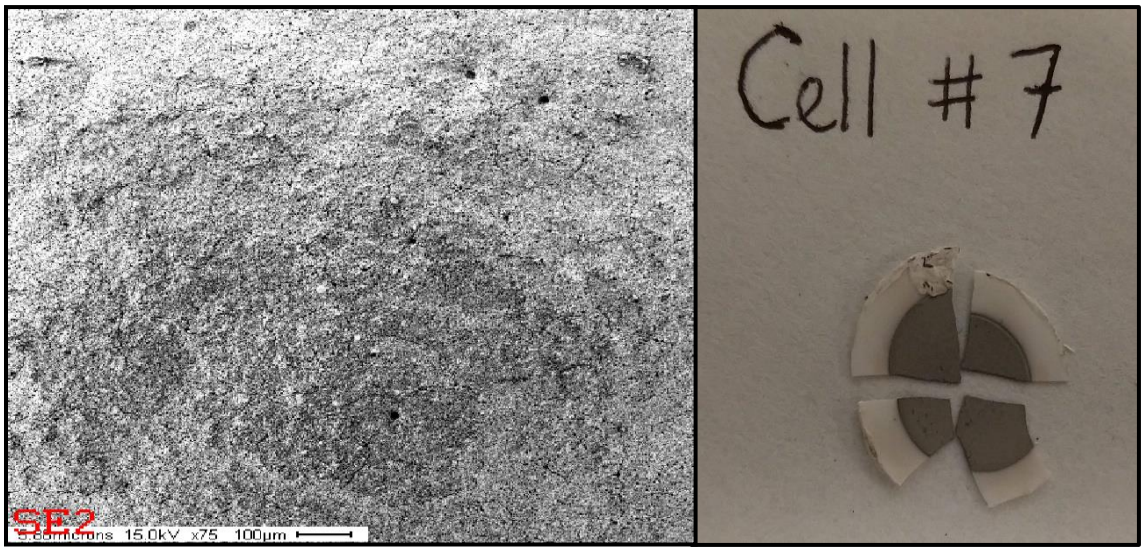

Figure 3.58: SEM image of Cell #7's anode at 75x magnification (left) and a picture showing the appearance of the cell (right)

The EDS results for Cell #7 at 75x magnification are reported in Figure 3.59 and Table 3.13.

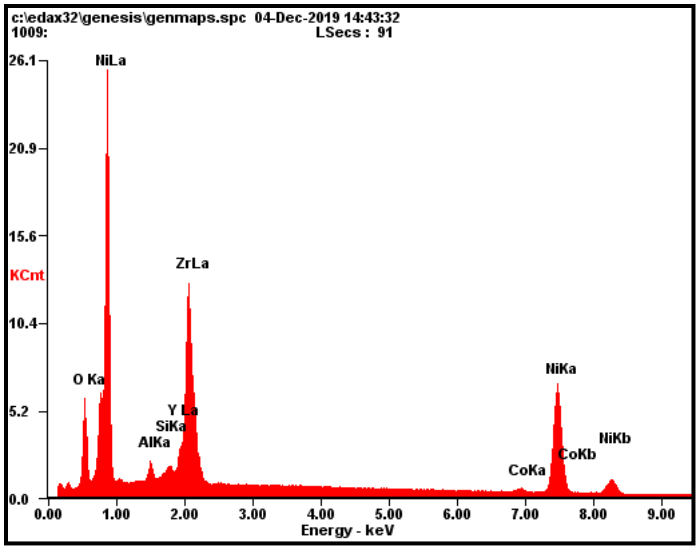

Figure 3.59: EDS spectrum of the Cell #7 anode (75x magnification)

Table 3.13: Weight and atomic percentages of elements in EDS spectrum of the Cell #7 anode (75x magnification)

Element	Weight %	Atom %
O_K	11	33
Al_K	1	2
Si_K	<1	1
Y_L	5	2
Zr_L	27	14
Co_K	2	1
Ni_K	54	45
Matrix Correction		*ZAF*

Unlike Cell #6, Cell #7's anode contained a detectable amount of silicon, possibly from the siloxanes in Mahoning Landfill gas. Although previous experiments with

humidified methane spiked with D5 showed that siloxane decomposes before reaching the anode, several factors may have affected siloxane decomposition in the Mahoning Landfill gas experiment. The highest concentration of D5 used in the previous experiments was 100 ppm for approximately three hours. For the actual landfill gas, the total siloxane concentration is unknown; at higher concentrations, silica could have coated the ProboStat™, not leaving a surface other than the anode for silica deposition. Furthermore, while D5 did not result in silica deposition on the anode, other siloxanes present in the landfill gas may behave differently based on their properties. Another analysis of the anode was done at 500x magnification, shown in Figure 3.60 and Figure 3.61.

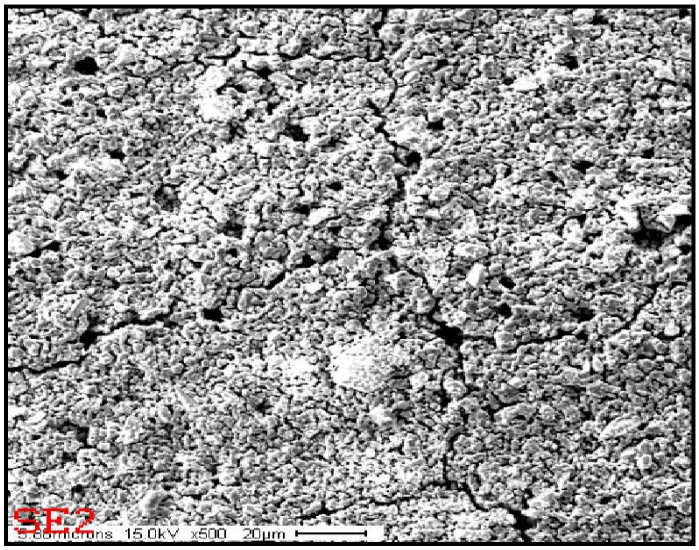

Figure 3.60: SEM image of Cell #7's anode at 500x magnification

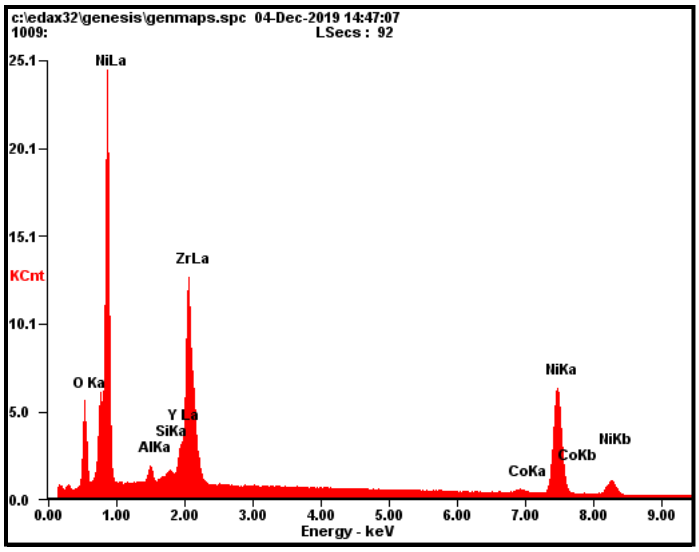

Figure 3.61: EDS spectrum of the Cell #7 anode (500x magnification)

The spectrum shown in Figure 3.61 is quantified in Table 3.14.

Table 3.14: Weight and atomic percentages of elements in EDS spectrum of the Cell #7 anode (500x magnification)

Element	Weight %	Atom %
O_K	11	33
Al_K	1	2
Si_K	<1	1
Y_L	5	3
Zr_L	27	15
Co_K	2	1
Ni_K	54	45
Matrix Correction		*ZAF*

As with the anode at 75x magnification, the analysis at 500x magnification showed a trace amount of silicon. A micrograph and EDS spectrum of the anode at 2000x magnification is given in Figure 3.62 and Figure 3.63.

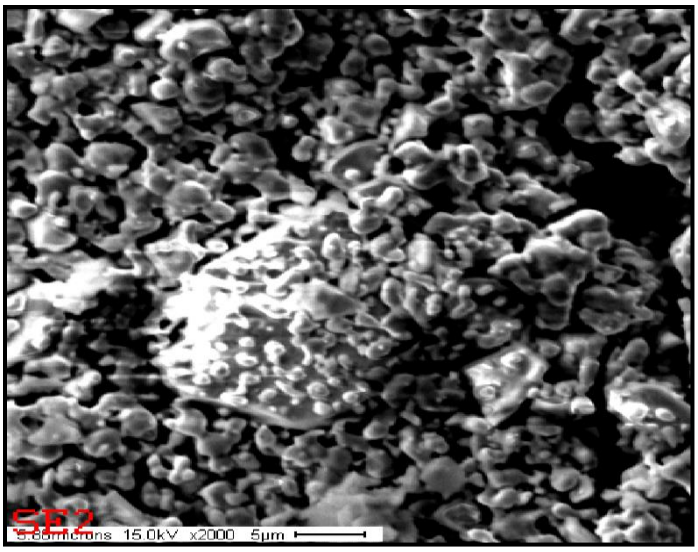

Figure 3.62: SEM image of Cell #7's anode at 2000x magnification

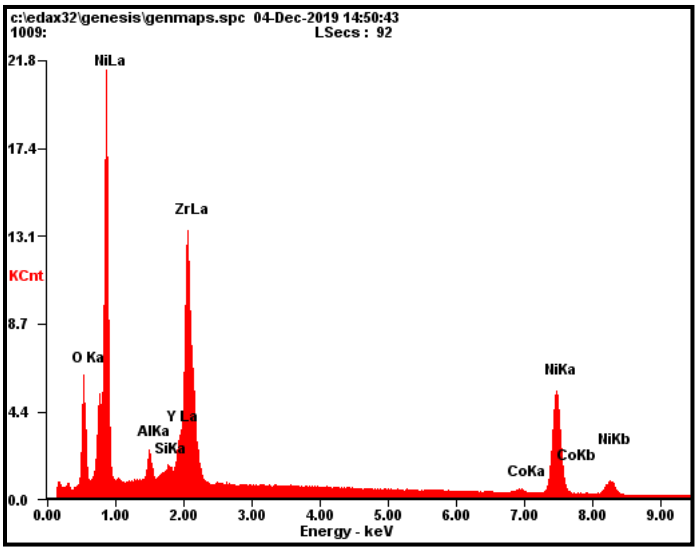

Figure 3.63: EDS spectrum of the Cell #7 anode (2000x magnification)

The weight and atomic percentages of elements found in the EDS spectrum at 2000x magnification, shown in Table 3.15, are comparable to those at 75x and 500x magnification.

Table 3.15: Weight and atomic percentages of elements in EDS spectrum of the Cell #7 anode (2000x magnification)

Element	Weight %	Atom %
O_K	12	37
Al_K	2	3
Si_K	<1	1
Y_L	5	3
Zr_L	30	16
Co_K	1	1
Ni_K	48	39
Matrix Correction		*ZAF*

The region in the center of Figure 3.62 was examined at 6000x magnification, and the results are given in Figure 3.64 and Figure 3.65.

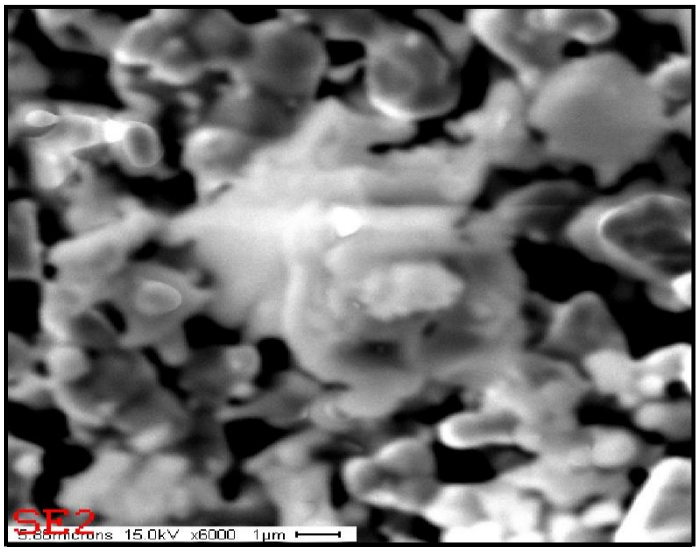

Figure 3.64: SEM image of Cell #7's anode at 6000x magnification

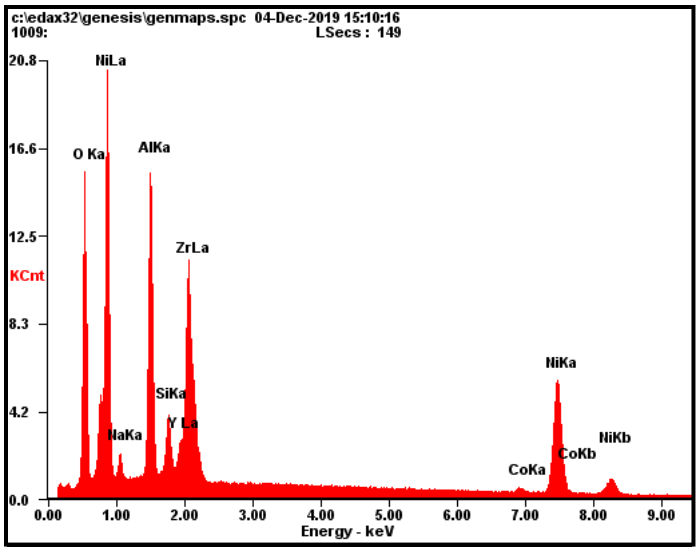

Figure 3.65: EDS spectrum of the Cell #7 anode (6000x magnification)

The spectrum shown above is quantified in Table 3.16.

Table 3.16: Weight and atomic percentages of elements in EDS spectrum of the Cell #7 anode (6000x magnification)

Element	Weight %	Atom %
O_K	21	45
Na_K	2	2
Al_K	13	17
Si_K	3	3
Y_L	3	1
Zr_L	19	7
Co_K	1	<1
Ni_K	38	23
Matrix Correction		*ZAF*

At a magnification of 6000x, a signal for sodium appeared. At this magnification, the percentages of aluminum and silicon present on the anode was higher. It is unclear whether the sodium is due to contamination, or if it was deposited from the landfill gas.

To get a better idea of the distribution of the different elements detected by EDS analysis, an elemental map, shown in Figure 3.66, was generated.

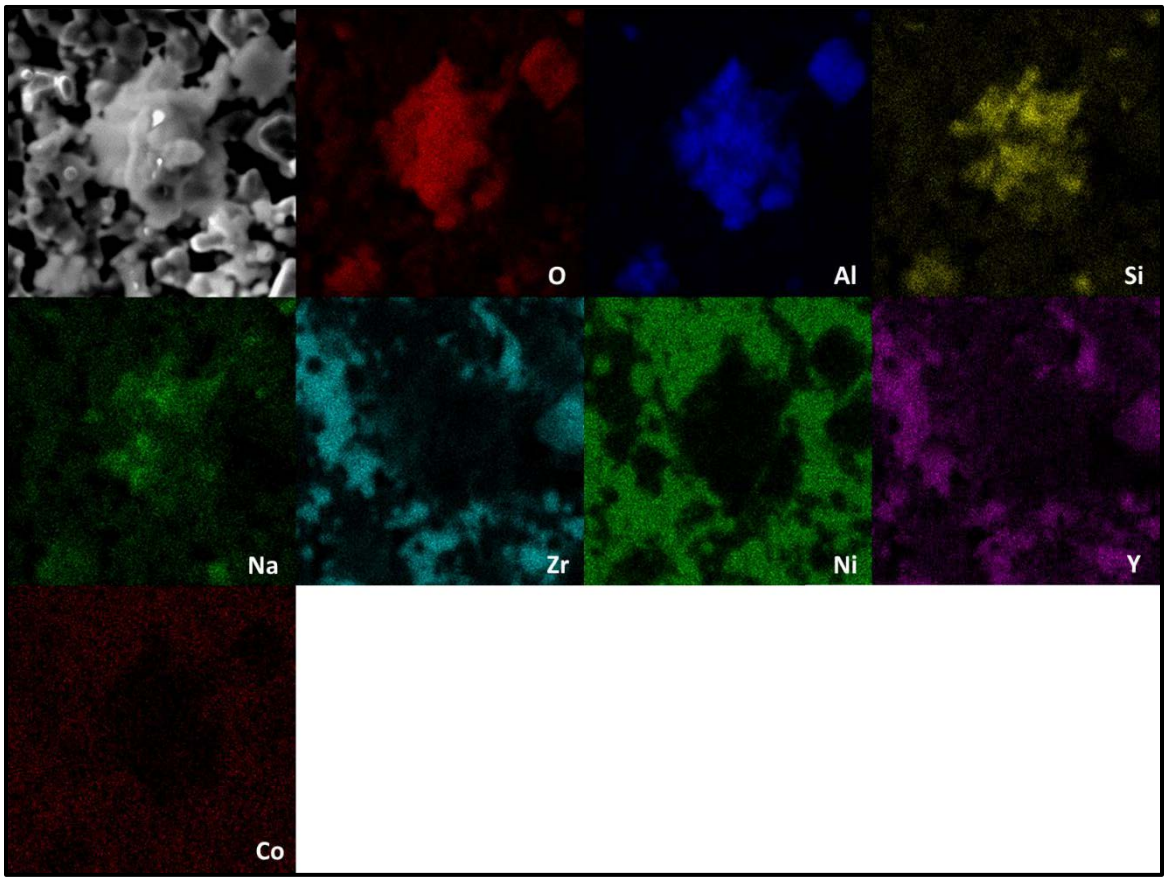

Figure 3.66: EDS elemental map for Cell #7 at 6000x magnification; clusters of high signal density in the O map match those in the Al, Si, and Na maps. These also match areas of low signal density in the Ni, Zr, Y, and Co maps.

In the elemental map above, signals for oxygen, aluminum, silicon, and sodium overlap, suggesting that the deposited material may be a silicate compound. The cluster map, shown in Figure 3.67, further supports this hypothesis.

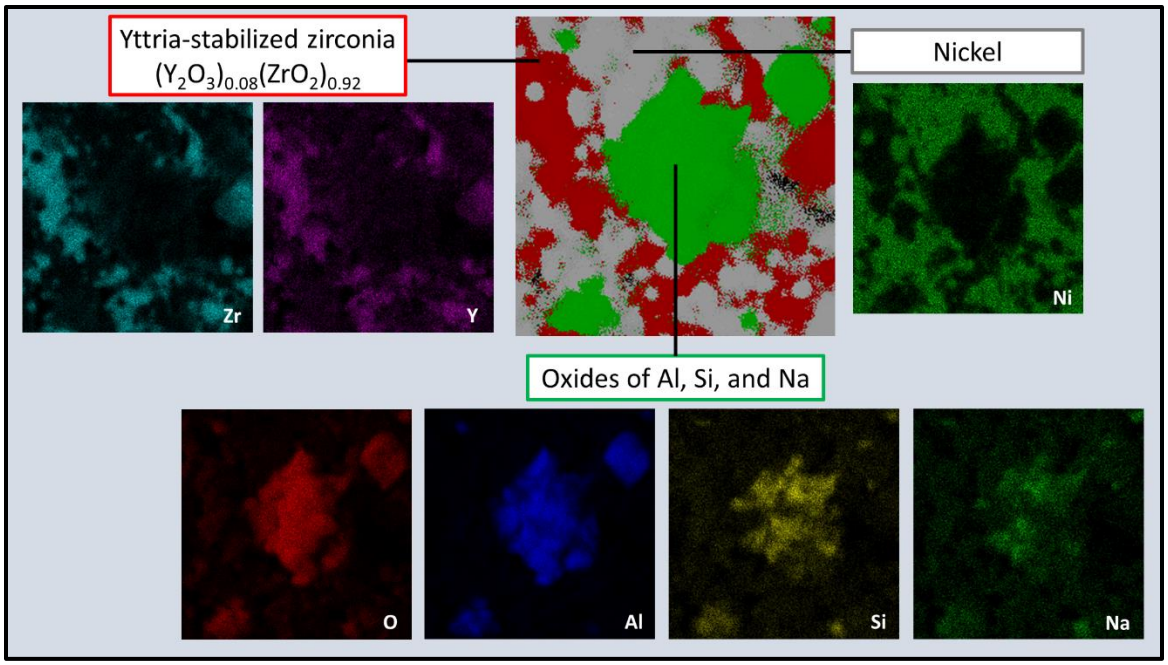

Figure 3.67: EDS cluster map for Cell #7 at 6000x magnification; two of the clusters contain oxygen, while the nickel oxide in the anode appears to have been completely reduced.

It is possible that the green cluster shown in Figure 3.67 is a silicate. Like silica, related silicates create glassy coatings on surfaces, so it is expected that the deposition of such a compound on the anode of a solid oxide fuel cell would have the same negative effect on performance as the deposition of silica has.

SEM/EDS Analysis of the Mahoning Landfill CAT 3516 Spark Plug Deposit

The presence of aluminum and sodium on the anode surface was unexpected. To explain these results, an SEM/EDS analysis of the gray deposit found on the spark plug obtained from the Mahoning Landfill (see Figure 1.9) was performed. The SEM micrograph and EDS spectrum of the spark plug deposit are shown in Figure 3.68 and Figure 3.69. The EDS data is quantified in Table 3.17.

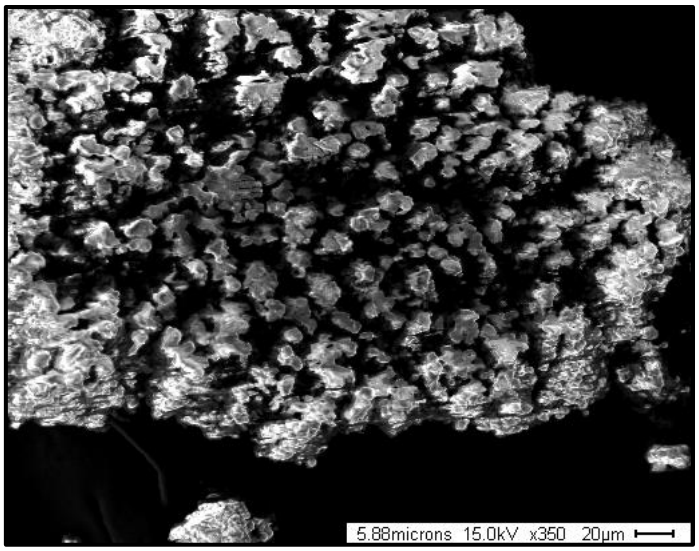

Figure 3.68: SEM image of the Mahoning Landfill spark plug deposit at 350x magnification

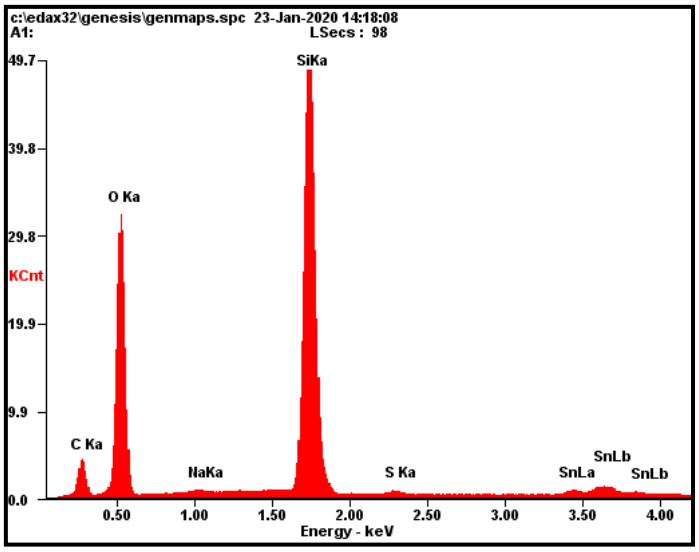

Figure 3.69: EDS spectrum of the Mahoning Landfill spark plug deposit at 350x magnification

Table 3.17: Weight and atomic percentages of elements in EDS spectrum of the Mahoning Landfill spark plug deposit (350x magnification)

Element	Weight %	Atom %
C_K	20	29
O_K	46	50
Na_K	<1	<1
Si_K	32	20
S_K	<1	<1
Sn_L	2	<1
Matrix Correction		*ZAF*

Based on the SEM/EDS results, the gray deposit found on the Mahoning Landfill spark plug is silica. As a result, these findings do not explain the decreased voltage and current output of the cells operated on humidified Mahoning Landfill gas; the SEM/EDS analysis of the Cell #7 anode found evidence of aluminum and sodium deposits, while an aluminum signal was notably absent from the EDS spectrum of the spark plug scrapings. It is possible that the alumina signals resulted from contamination with Ceramabond, which contains an alumina filler.[28] To determine the likelihood that Ceramabond was responsible for the sodium and aluminum signals present on the anode of Cell #7, an X-ray fluorescence spectrometry (XRF) analysis of Ceramabond was completed.

XRF Analysis of Ceramabond

Ceramabond was cured and fired according to the manufacturer's instructions and pulverized into a powder for XRF analysis. The results of the XRF analysis of Ceramabond are shown in Figure 3.70.

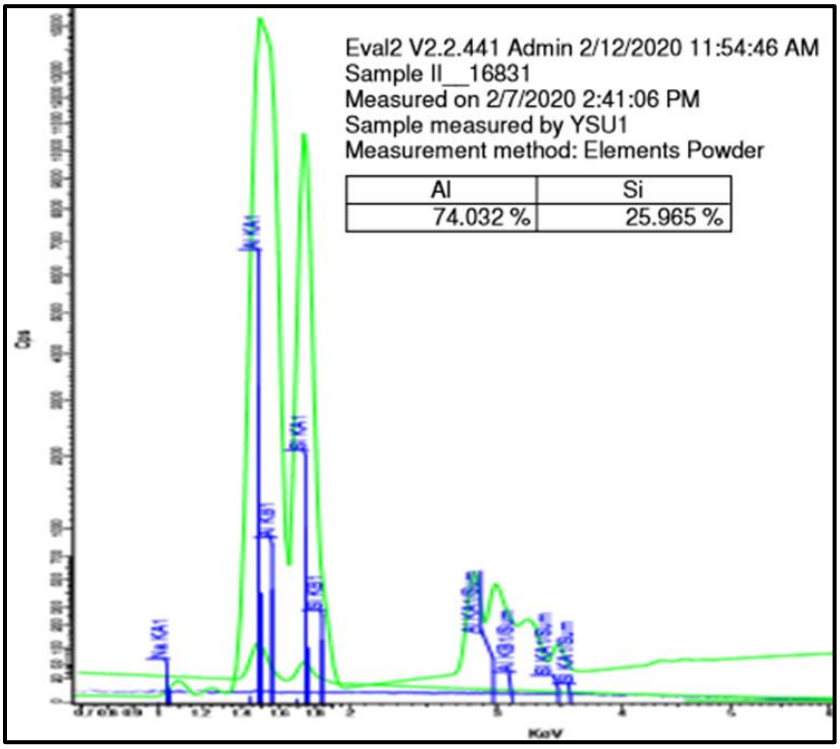

Figure 3.70: XRF spectrum for Ceramabond

According to the XRF analysis, Ceramabond contains approximately 74% aluminum and 26% silicon. The MSDS for Ceramabond gives its composition as "aluminum oxide and silicate solution."[44] Recall that XRF is unable to detect elements lighter than sodium, so the oxygen content was not quantified. Similarly, the spectrum shows a peak for sodium, but it too was not quantified by the instrument. Based on these results and the cluster map shown in Figure 3.67, it is likely that the silicate solution mentioned in the Ceramabond MSDS is sodium silicate. The XRF data reported above raised concerns about

Ceramabond contamination on the anode of Cell #7. To examine this possibility, the Cell #7 anode was reanalyzed using SEM/EDS.

Cell #7: Cleaned Anode

The Cell #7 anode was analyzed using SEM/EDS. It was then cleaned with several bursts of compressed air and reanalyzed. Figure 3.71 and Figure 3.72 show the SEM micrograph and EDS spectrum of the Cell #7 prior to cleaning. The results are quantified in Table 3.18.

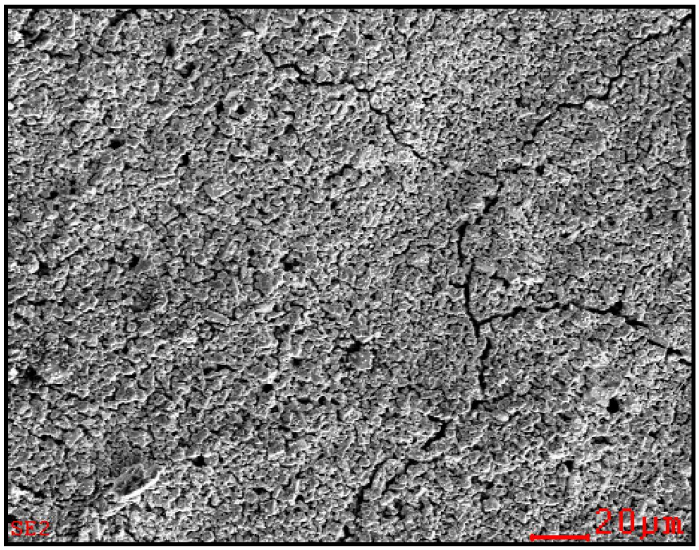

Figure 3.71: SEM image of the Cell #7 anode at 500x magnification (before cleaning with compressed air)

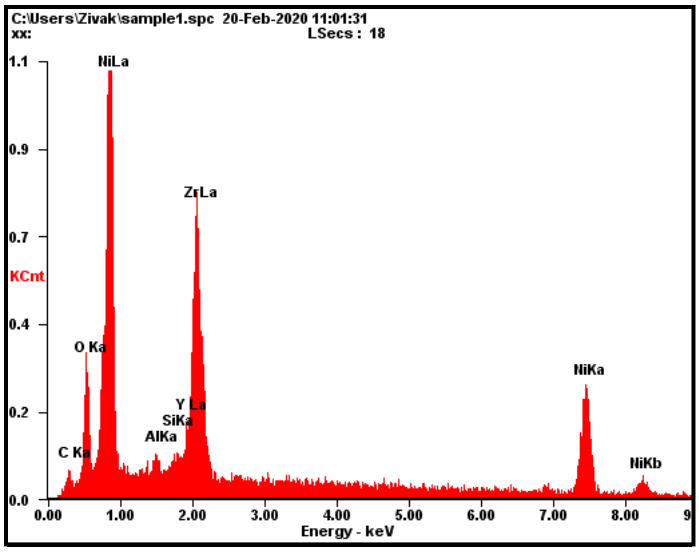

Figure 3.72: EDS spectrum of the Cell #7 anode at 500x magnification (before cleaning with compressed air)

Table 3.18: Weight and atomic percentages of elements in EDS spectrum of the Cell #7 anode at 500x magnification (before cleaning with compressed air)

Element	Weight %	Atom %
C_K	8	23
O_K	16	35
Al_K	1	1
Si_K	<1	1
Y_L	6	2
Zr_L	29	12
Ni_K	41	25
Matrix Correction		*ZAF*

Figure 3.73 and Figure 3.74 show the SEM micrograph and EDS spectrum of the Cell #7 anode after it was cleaned with compressed air. The results are quantified in Table 3.19.

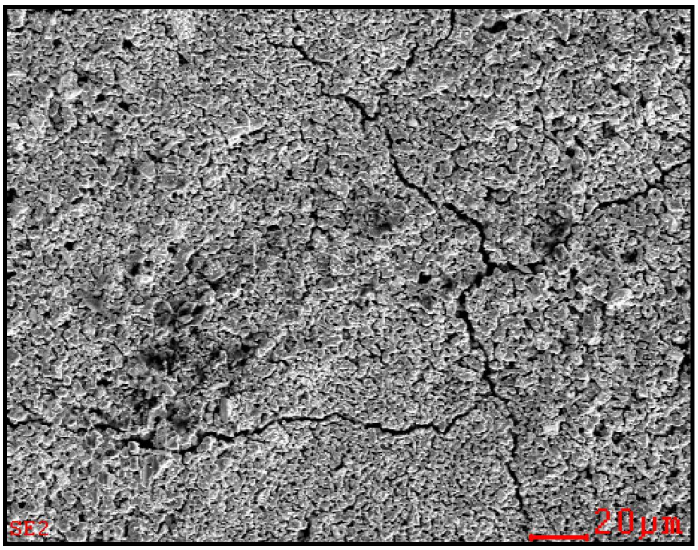

Figure 3.73: SEM image of the Cell #7 anode at 500x magnification (after cleaning with compressed air)

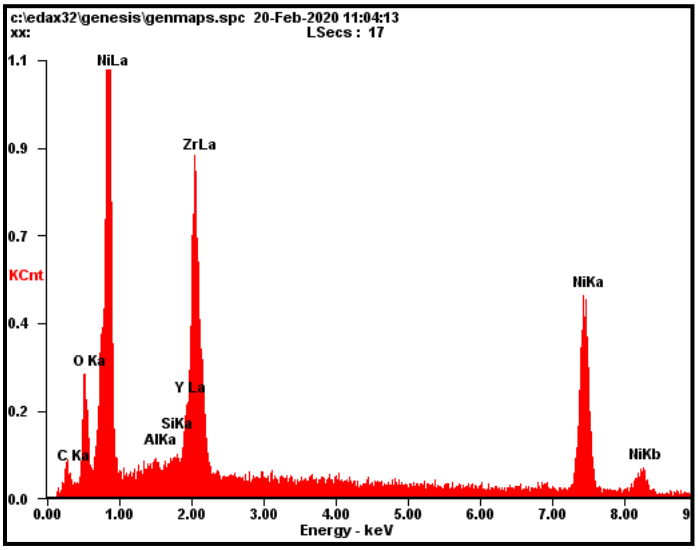

Figure 3.74: EDS spectrum of the Cell #7 anode at 500x magnification (after cleaning with compressed air)

Table 3.19: Weight and atomic percentages of elements in EDS spectrum of the Cell #7 anode at 500x magnification (after cleaning with compressed air)

Element	Weight %	Atom %
C_K	8	28
O_K	10	24
Al_K	<1	1
Si_K	<1	<1
Y_L	5	2
Zr_L	25	11
Ni_K	50	34
Matrix Correction		*ZAF*

Compared to the original EDS analysis of the Cell #7 anode at 500x magnification reported in Table 3.14, the second analysis of the anode, reported in Table 3.18, showed a decreased amount of aluminum and silicon. This suggests that Ceramabond was indeed responsible for the aluminum and silicon signals, as the residue was probably removed while the cell was handled between analyses. Additionally, the analysis after the anode was cleaned with compressed air, reported in Table 3.19, shows a further decrease in aluminum and silicon content. Based on the SEM/EDS data for Cell #7 prior to and after cleaning with compressed air, the aluminum and silicon signals previously found on the Cell #7 anode resulted from Ceramabond contamination, likely during the process of removing the cell from the ProboStat™ using a Dremel tool. Because contaminants found on the anode of the cell operated on Mahoning Landfill gas were due to Ceramabond, the reason for the cells' worsened performance remains unexplained by SEM and EDS techniques.

CHAPTER 4: CONCLUSIONS

The long-term goal of this research project was to see if a Ni-YSZ/Hionic™/LSM solid oxide fuel cell could be operated on Mahoning Landfill gas. Other studies had concentrated on the effects of carbon deposition and sulfide poisoning on the cells' nickel-based anode, but this project sought to examine the effect of silica deposition due to siloxanes present in landfill gas. This goal was accomplished in four stages. In the first stage, voltammetric experiments were used to verify that the button cells used in the study could be mounted on the ProboStat™ and successfully operated. Tests using hydrogen and humidified methane demonstrated that the cells achieved open circuit voltage outputs that agreed with literature values. These experiments also confirmed that, in the case of humidified methane, a humidification level of 67% sufficiently prevented carbon deposition.

In the second stage of research, cells were operated on humidified fuel gas intentionally spiked with known concentrations of decamethylcyclopentasiloxane (D5), a representative siloxane present in most landfills. When the cell was operated on humidified methane spiked with D5 in concentrations of 1-100 ppmv, there was no loss in cell performance, as measured by voltage and current output over time. Scanning electron microscopy and energy-dispersive X-ray spectroscopy did not detect the presence of silica on the cell anodes; however, X-ray diffraction analysis of a deposit scraped from the ProboStat™ revealed that crystalline silica had deposited on the instrument itself. This discovery suggested that in the presence of water, siloxanes decompose to form silica before reaching the anode. As a result, siloxanes should not affect cell performance if a sacrificial surface for silica deposition is available.

When the cells were operated on dry hydrogen spiked with 1-10 ppmv D5, the siloxane did not encounter water until it reached the anode, where water is a product of the electrochemical reaction. Consequently, the decomposition of siloxane into silica occurred on the anode. In these experiments, a significant decrease in cell performance was observed. A cell operated on hydrogen that contained 1 ppmv D5 showed a 3% loss in voltage output after 3 hours, and when the D5 concentration was increased to 5 ppmv, the cell experienced a 7% loss in voltage output after 3 hours, for a 10% decrease in voltage output after 6 hours. A second cell, operated on hydrogen containing 10 ppmv D5, lost 13% of its initial voltage output after 6 hours. SEM and EDS analysis detected silica on the anode. The results of these experiments show that the deposition of silica on the cell anode has a negative effect on the cell's output.

In the third stage, cells were operated on humidified Mahoning Landfill gas. A humidification level of 67% prevented carbon deposition, and pretreatment with a chemisorbent filter appeared to sufficiently remove hydrogen sulfide from the gas sample, at least below a 1 ppm detection limit. However, despite eliminating the effects of carbon deposition and sulfide poisoning, the cells achieved lower voltage and current outputs than expected based on the results of the humidified methane experiments. The fourth stage of research sought to identify the compounds responsible for the degraded performance. From the results obtained from SEM/EDS analysis, although silica was previously shown to have a damaging effect on the output of SOFCs, it cannot be confidently stated that the siloxanes present in Mahoning Landfill gas were the definitive reason why the cells operated on Mahoning Landfill gas did not reach the expected level of performance established during experiments with humidified methane. For one,

although Cell #6 was operated on Mahoning Landfill gas and showed subpar voltage and current output, EDS did not detect the presence of silica on its anode. Similarly, the second cell operated on Mahoning Landfill gas, Cell #7, performed worse than expected. However, while EDS identified signals for silicon, a cluster analysis suggested that the silicon was present in a compound also containing aluminum and sodium rather than in silica. Unlike the contaminants found on the surface of the Cell #7 anode, an EDS analysis of the deposit scraped from the spark plug of an engine operated on Mahoning Landfill gas identified the deposit as silica. This indicates that something other than Mahoning Landfill gas is responsible for the deposition of an aluminum compound.

An XRF analysis of Ceramabond, the material used to affix button cells to the ProboStat™, revealed that it contains aluminum oxide and silicate salts, raising the possibility of Ceramabond contamination.[44] A second analysis of the Cell #7 anode, in which the anode was cleaned with compressed air, showed a marked decrease in aluminum and silicon content, suggesting that the contaminants found in the first analysis were indeed due to Ceramabond residue. The SEM/EDS results, combined with the behavior of siloxanes in the experiments with D5-spiked humidified methane, imply that when operating a solid oxide fuel cell on Mahoning Landfill gas, silica deposition is not a concern. If the fuel gas is sufficiently humidified and there is a sacrificial surface for silica deposition, siloxane removal prior to feeding the gas into the cell is unnecessary.

Future Directions

While the effect of siloxanes on solid oxide fuel cell performance was observed, future studies examining the operation of these cells on Mahoning Landfill gas are needed. Voltammetric experiments showed that the effects of carbon deposition and

hydrogen sulfide poisoning were successfully mitigated, and surface analysis techniques did not show the presence of silica resulting from siloxane decomposition. Despite these positive results, fuel cells operated on humidified Mahoning Landfill gas performed worse than the analogous fuel cells operated on humidified methane, suggesting that other compounds capable of causing decreased cell performance are present in Mahoning Landfill gas.

SEM/EDS analysis of the SOFC anodes could not provide an answer as to which substances, other than siloxanes, may have led to a loss of anode function. Perhaps more surface-specific techniques of anode analysis, such as X-ray photoelectron spectroscopy (XPS), could better detect compounds present on the anode surface, especially if very thin layers of contaminants are deposited. Additionally, it may be necessary to develop a reliable technique for identifying the many parts per million level components present in Mahoning Landfill gas itself. For example, an analysis of the landfill gas itself using a sensitive gas chromatography instrument would be beneficial for identifying possible contaminants of interest. Once contaminants of interest are identified, experiments can be designed to individually examine and mitigate their effects on the anode.

Although it is unrelated to contaminants in landfill gas, a significant obstacle to studying fuel cell performance became obvious. Due to the design of the ProboStat™, water condenses inside the instrument during operation on humidified gases, leading to a repeated buildup and release of pressure, eventually causing the formation of cracks in the cell. Once the cell cracks, the flows of gases to the anode and cathode are no longer separated, and the effects are erratic voltage and current readings. Thus, prolonged voltammetric experiments could not be performed. Perhaps if the cells could be operated

for several days instead of hours, contaminants would build up on the anode in a layer thick enough to be studied using SEM/EDS techniques. The issue of cell cracking due to condensation must be resolved, potentially by modifying the ProboStat™ or developing a new apparatus for testing button cell performance.

CHAPTER 5: SUPPLEMENTAL – TESTS WITH PLANAR NI-YSZ/HIONIC™/LSM CELLS

Part I: Introduction

Initially, the goal of this project was to scale the button cell experiments up to a 28 cm^2 planar cell made of the same materials. Because of its greater active electrode area, the planar cell was expected to have greater fuel utilization and gas turnover than the button cell. These factors would allow for the collection of gas chromatography data, which is not feasible with the button cell. However, one key failure mode, discussed in this chapter, prevented the completion of the proposed experiments.

While the planar cell could be operated on hydrogen gas and give voltammetric data in agreement with literature values, the introduction of humidified gases into the system caused the cell to crack. The successful hydrogen tests and the attempts to troubleshoot and resolve the cracking issue will be discussed in this supplemental chapter.

Part II: Materials, Instrumentation, and Methods

Planar Cell Operation

The general apparatus and procedure for operating a planar cell on a fuel gas, whether it is dry hydrogen or humidified methane, is described below.

Planar Cell

Planar electrolyte-supported cells consisting of a Ni-YSZ anode, Hionic™ electrolyte, and LSM cathode were purchased from Fuel Cell Materials in Lewis Center,

Ohio. These planar cells measure 10 cm by 10 cm, with an active anode/cathode area of 28 cm^2. Figure 5.1 is a diagram of a planar cell, showing both the anode side and the cathode side.

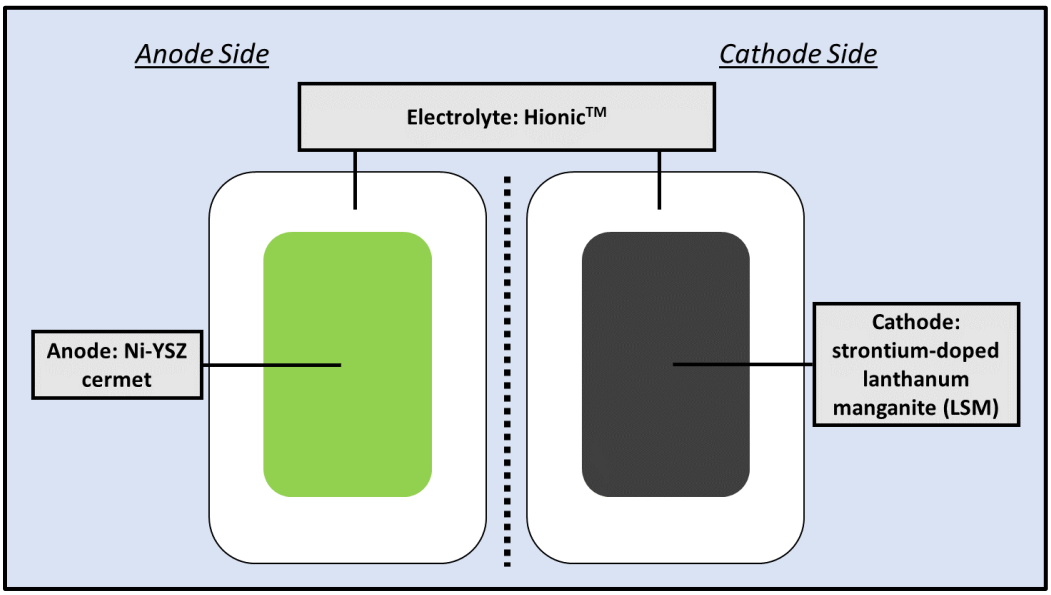

Figure 5.1: Diagram showing both the anode side and the cathode side of a planar Ni-YSZ/Hionic™/LSM cell

The setup for using the planar cell consists of the cell sandwiched between two Crofer manifolds, with each manifold having a gas inlet, a gas outlet, and gas flow channels. Crofer is an alloy of iron and chromium, used in SOFCs because of its stability at the elevated temperatures required for SOFC operation and its high electrical conductivity.

The cells were prepared according to the operating instructions.[45] An alumina felt seal was applied to each manifold and saturated with a slurry of aluminum oxide. The active area of the anode manifold was painted with nickel ink, and a piece of nickel mesh trimmed to fit the active area was placed on the manifold. The anode itself was also painted with nickel ink, and the cell was placed on the manifold, taking care to align the

anode with the active area of the anode manifold. The cathode of the cell was painted with LSM ink, a piece of silver mesh was placed on top of the cathode, and a layer of LSM ink was applied on top of the silver mesh. The cathode manifold was then placed on the cell. The cell was placed in the box furnace, compressed using a weight system, and conditioned by heating to 750°C at a rate of 1°C/minute. A diagram of the Crofer manifolds is shown in Figure 5.2.

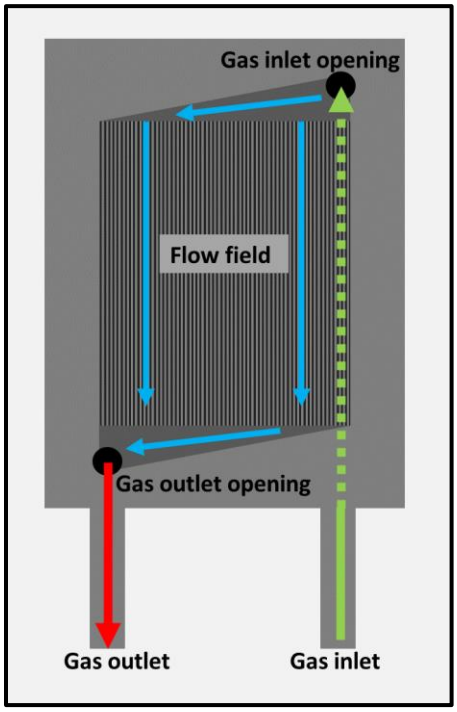

Figure 5.2: Diagram of gas flow in a Crofer manifold plate

In Figure 5.2, gas enters the Crofer manifold through the gas inlet, passes through the inside of the manifold plate where it is heated to the operating temperature of the cell, and then reaches the cell through the gas inlet opening. The gas reacts with the active electrode of the cell while passing across the flow field of the manifold plate, eventually exiting the manifold through the gas outlet opening and the gas outlet. Figure 5.3 shows the planar cell sandwiched between two Crofer manifold plates.

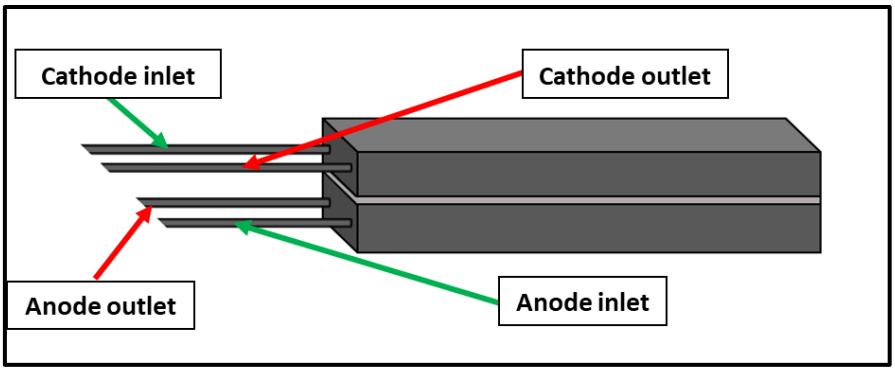

Figure 5.3: Diagram of the Crofer manifold/planar cell assembly

Box Furnace

A Lindberg/Blue box furnace model BF51748A-1 modified to accommodate the Crofer manifolds was used for holding the planar cell at operating temperatures. The furnace has four openings at its back panel, through which the gas inlet and outlet of each manifold protrude. The support bar for the weight system is placed through the exhaust vent at the top of the furnace. This furnace model includes a programmable temperature controller.

Weight System

A weight system is necessary to apply pressure on the manifolds, providing a seal that minimizes gas mixing within the manifolds and prevents gas from escaping through the sides of the manifolds. Weight plates totaling 65 pounds are placed on a support bar that is placed through an opening at the top of the furnace, providing a pinch pressure of 4.9 psi on the cell. The weight bar rests on a custom-made Crofer piece that fits on the manifolds and distributes pressure to the edges of the manifolds, reducing the risk of cracking the cell. The weight system is isolated from the circuit with a layer of alumina

felt placed between the weight bar and the Crofer manifold. Figure 5.4 is a photograph of the box furnace with the manifolds inside, also showing the weight system.

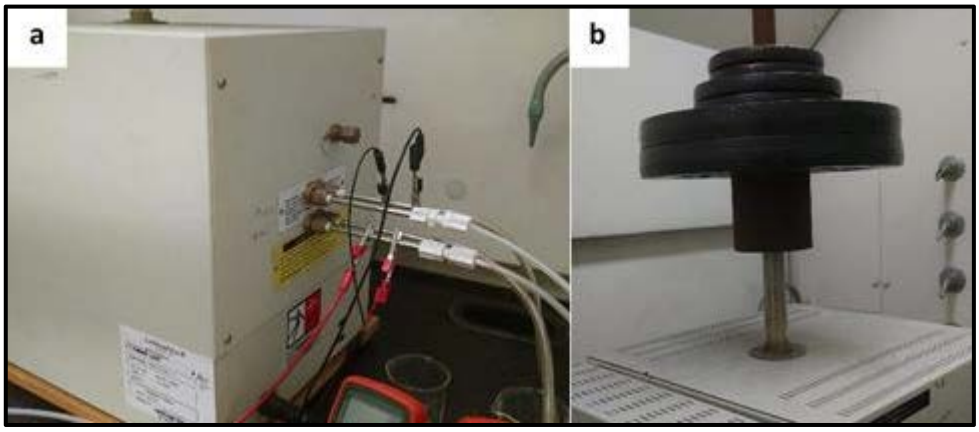

Figure 5.4: Picture of a) the manifolds protruding from the back of the box furnace and b) the weight system on top of the box furnace

Mass Flow Controller

Model FMA5400/5500 mass flow controllers, manufactured by Omega Engineering, capable of delivering up to 1 L/minute of gas were used to supply fuel gas and air to the cell.

Multimeters

Extech EX430 11-Function True RMS Professional MultiMeters were used to measure voltage and current outputs at variable loads.

Circuit Setup

Voltammetric data was collected with the planar cell operating on several fuel gases. First, the cell was run on hydrogen to verify that the setup did not leak and that the

cell had acceptable current and voltage outputs. As with the button cell discussed in Part I, when hydrocarbon fuels were used, humidifying the fuel gas was necessary to avoid carbon deposition. The same humidification system was used when operating the planar cell. Voltammetric measurements on the planar cell were performed using an ammeter and a voltmeter, set up as shown in the circuit diagram in Figure 5.5.

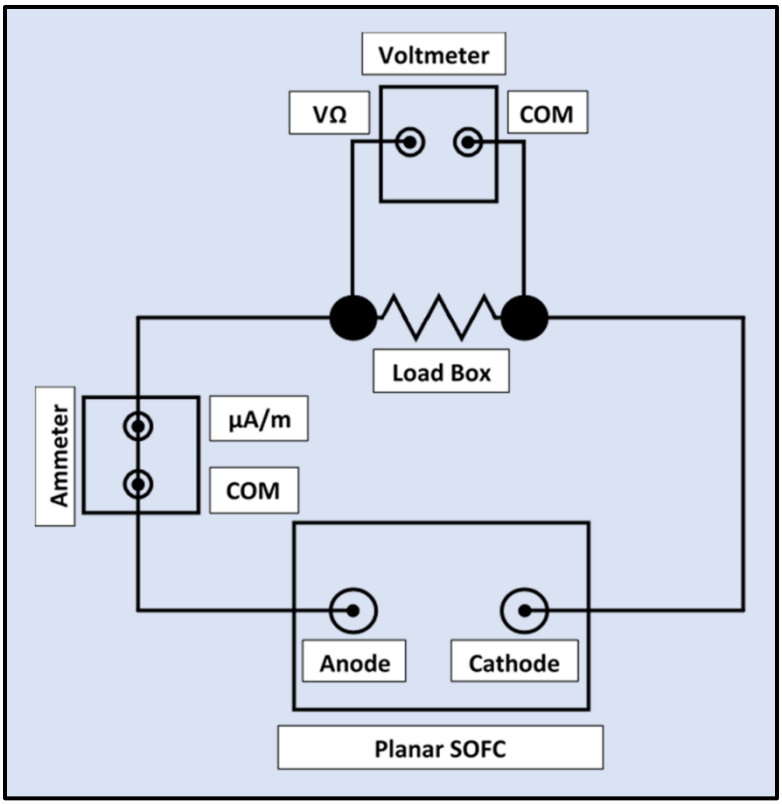

Figure 5.5: Circuit diagram for current-voltage measurements of planar cell

Part III: Results and Discussion

Planar Cell Operated on Hydrogen

The planar cell was operated on hydrogen gas to ensure that the system did not leak and could deliver voltage and current outputs close to the literature values of 0.9 V

to 1.1 V.[46] For these experiments, the cell was set up as described in Part II of Chapter 2, but because operating the cell on hydrogen does not carry the risk of carbon deposition, the humidification assembly was not used. The cell was operated at 750°C, while the flow rates of hydrogen to the anode and air to the cathode were varied. Equation 1.4 described the overall reaction for a cell operating on hydrogen as

$$2H_2 + O_2 \rightarrow 2H_2O \qquad (1.4)$$

Because air is only 20% oxygen, a 2:5 ratio of H_2 to air was maintained. Figures 5.6 through 5.9 show the resulting polarization curves. This data was collected as the load box was used to decrease, then increase, the resistance from 9999 Ω to 999 Ω to 99, from 99 Ω to 19 Ω in 10-Ω increments, and from 19 Ω to 1 Ω in 1-Ω increments.

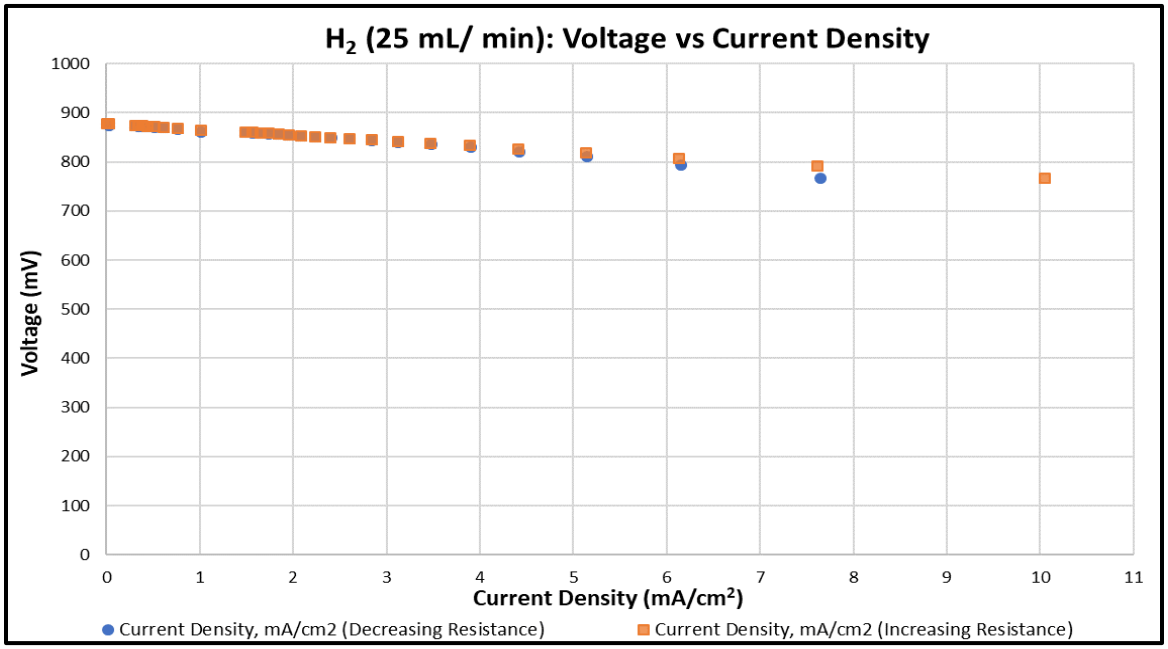

Figure 5.6: Polarization curve for the Ni-YSZ/Hionic™/LSM planar cell operated on 25 mL/min H_2 and 63 mL/min air at 750°C

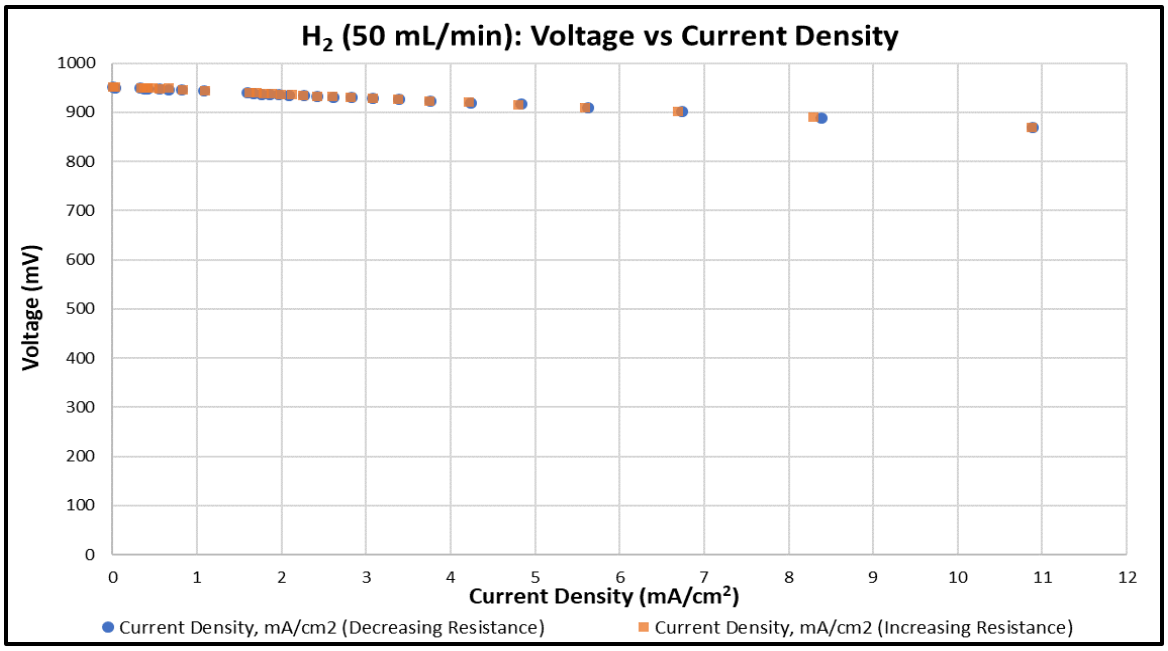

Figure 5.7: Polarization curve for the Ni-YSZ/Hionic™/LSM planar cell operated on 50 mL/min H_2 and 125 mL/min air at 750°C

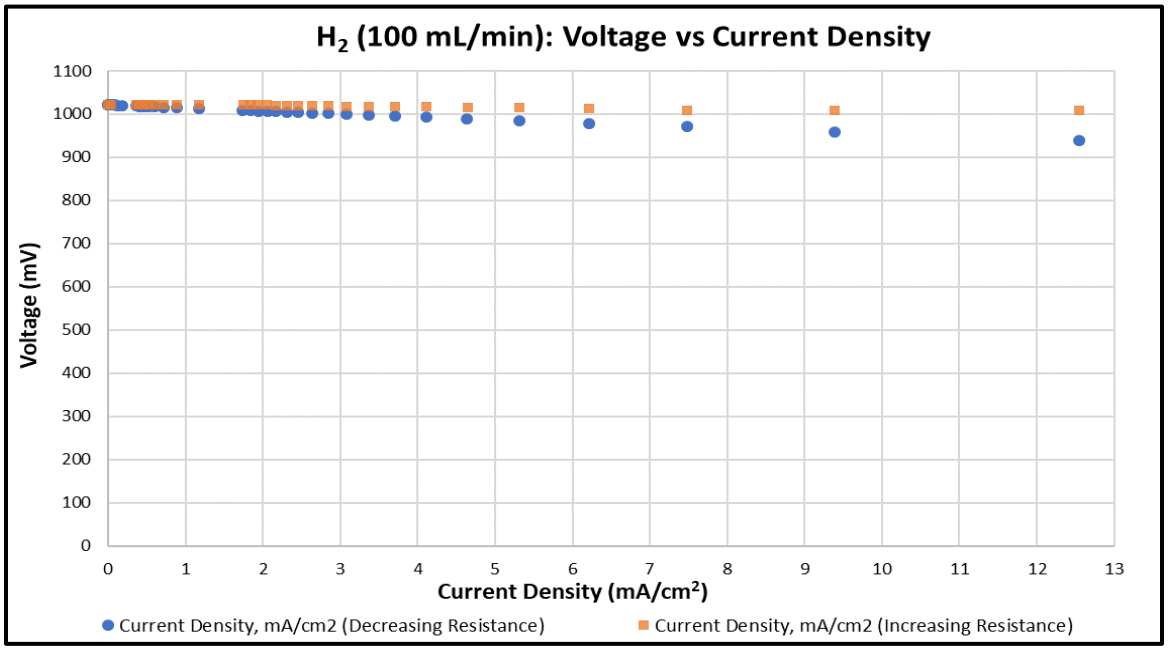

Figure 5.8: Polarization curve for the Ni-YSZ/Hionic™/LSM planar cell operated on 100 mL/min H_2 and 250 mL/min air at 750°C

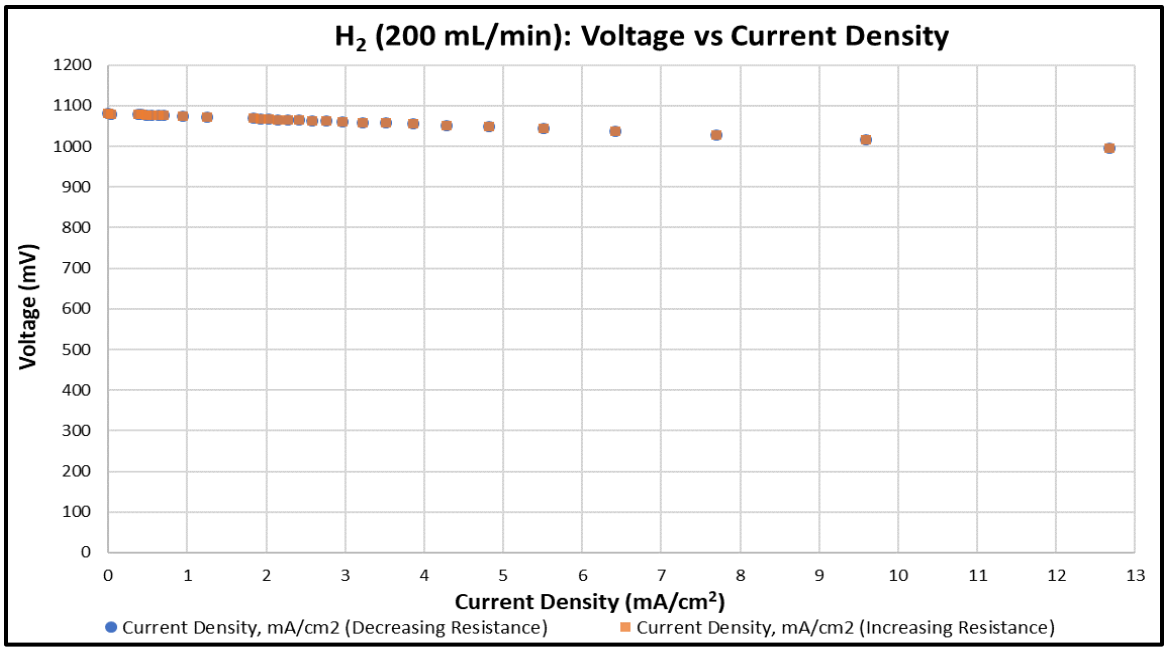

Figure 5.9: Polarization curve for the Ni-YSZ/Hionic™/LSM planar cell operated on 200 mL/min H_2 and 500 mL/min air at 750°C

The polarization curves for the Ni-YSZ/Hionic™/LSM planar cells operated on hydrogen gas exhibit similar behavior to those for the button cell operated on hydrogen and humidified methane. As with the button cell polarization curves, there is no activation loss region visible in the curves shown in Figures 5.6 through 5.9, but this is expected. When the cell is operated at a high load and the voltage output is high, the current output is very small. The ammeter used for the voltammetric experiments cannot reliably measure currents less than 0.1 mA, so one should not anticipate seeing the activation loss region in the polarization curves because the reading is limited by the sensitivity of the instruments.

In the polarization curves in Figures 5.6 through 5.9, the linear region makes up the entirety of the polarization curves. This region corresponds to the ohmic losses due to the cell resistance. Like in the previous polarization curves, the concentration loss region

due to mass transport is not apparent in Figures 5.6 through 5.9. Concentration losses occur when reactants are depleted at the electrodes, causing the concentration of reactants to fall below the bulk concentration and reducing the current and voltage output of the cell. This effect is undesirable; however, for investigational purposes, the flow rates of hydrogen and air were reduced to verify that mass transport can be observed. The polarization curve given in Figure 5.10 shows the mass transport region.

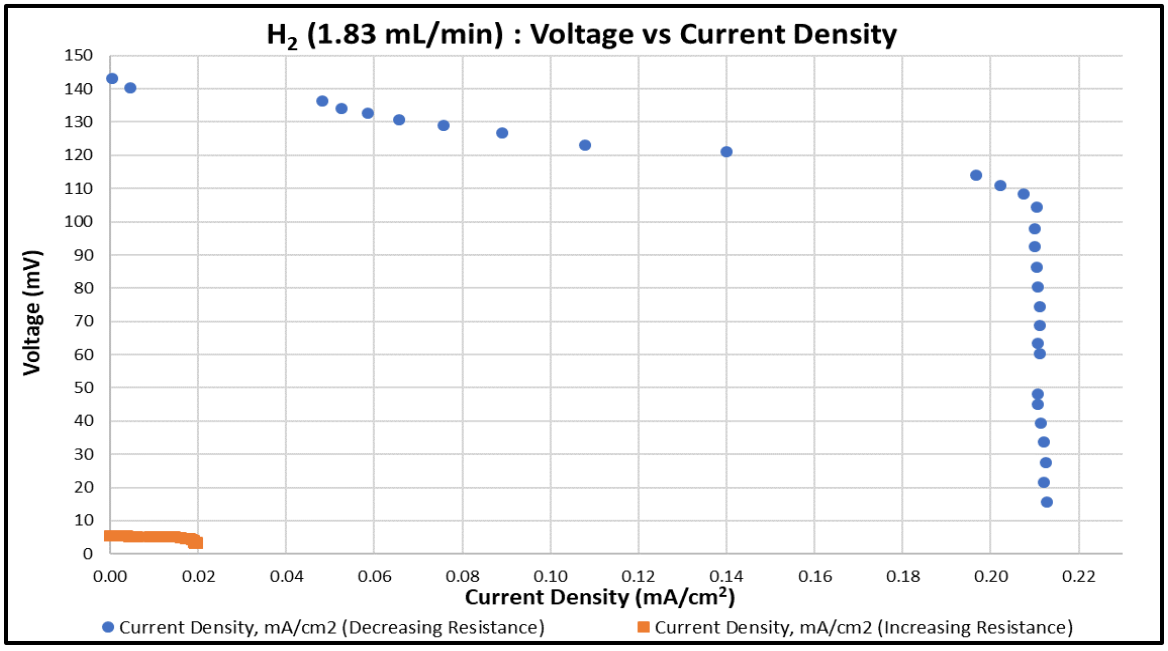

Figure 5.10: Polarization curve showing mass transport; Ni-YSZ/Hionic™/LSM planar cell operated on 1.83 mL/min H_2 and 4.58 mL/min air at 750°C

The figure above shows a steep decline in voltage and what appears to be a limit in the current density, representing the region where mass transport dominates the flow of current through the cell. Assuming the reaction coefficient for the reaction described by Equation 1.4 is sufficiently large, the amount of current flowing through the cell can be predicted by the concentration of reactants at the electrode surface. In this case, the current output of the cell was controlled by limiting the concentration of reactants

available at the electrode surfaces, which was achieved by slowing the flow rates of hydrogen and air into the cell.

Planar Cell Operated on Humidified Methane

In Chapter 1, Equation 1.10 gave the overall reaction for a solid oxide fuel cell operating on methane as

$$CH_4 + 2O_2 \rightleftarrows CO_2 + 2H_2O \qquad (1.10)$$

where one mole of methane requires two moles of oxygen. Because air is 20% oxygen, the desired flow rate ratio of methane to air is 1:10. While this stoichiometric ratio could be ignored when operating the button cell, the planar cell was expected to have higher fuel utilization; as a result, the 1:2 ratio of methane to oxygen was maintained. As with the button cell operating on methane, methane was fed through a humidification system, blending it with 89°C water vapor. A diagram of the experimental apparatus is given in Figure 5.11.

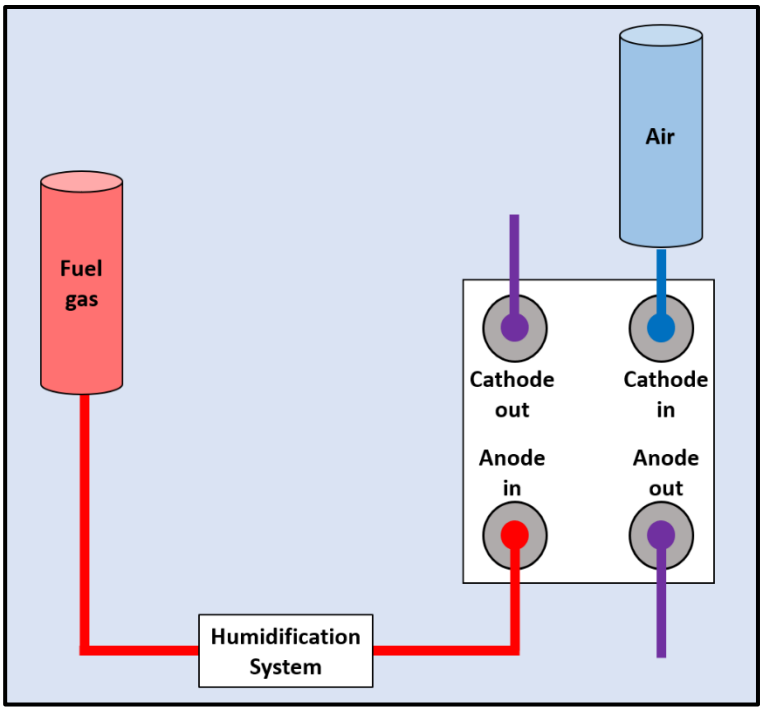

Figure 5.11: Apparatus for running the planar cell on humidified gas

The cell was operated at 750°C, and the load box resistance was varied as described for the planar cell operated on hydrogen, resulting in the polarization curve given in Figure 5.12.

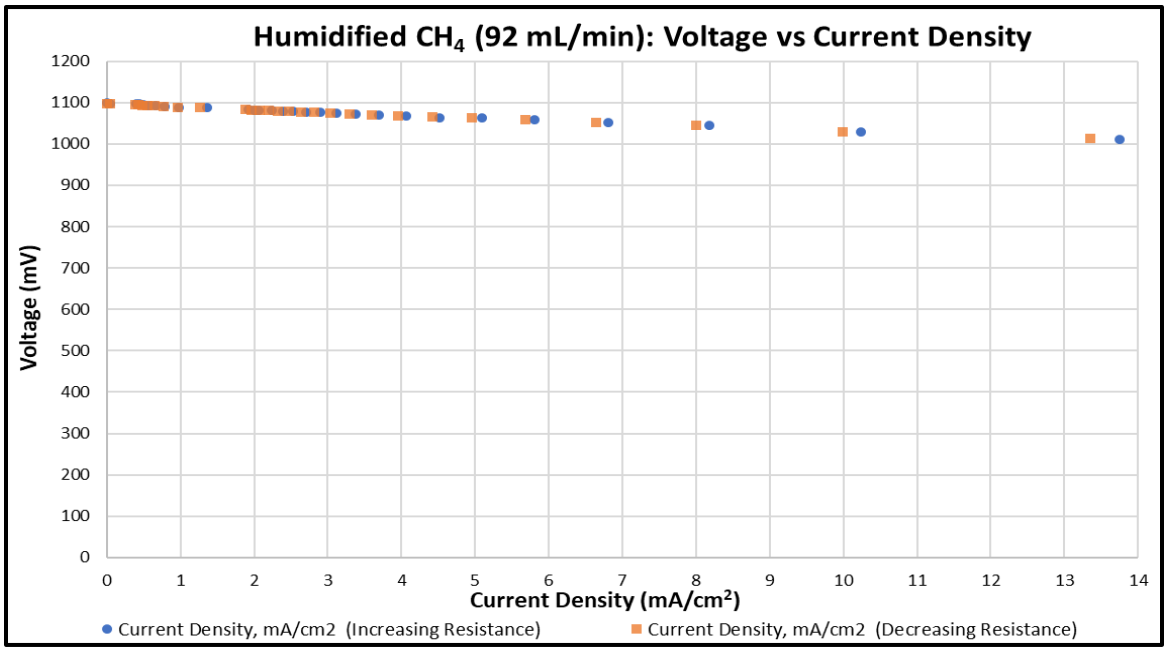

Figure 5.12: Polarization curve for the Ni-YSZ/Hionic™/LSM planar cell operated on 92 mL/min humidified CH_4 and 1000 mL/min air at 750°C

The cell ran successfully, achieving an open circuit voltage of approximately 1.1 V, as shown in the figure above. Using Equation 3.2,

$$E° = \frac{-\Delta G}{nF} \tag{3.2}$$

the theoretical maximum voltage for a cell operating on methane at standard conditions of 1 atm and 298 K is approximately 1.27 V.[47] At an operating temperature of 750°C, the theoretical value is expected to be lower, as the Gibbs free energy associated with the reaction decreases as the temperature increases. Furthermore, irreversibility in the system means that the experimental open-circuit voltage will not reach the calculated theoretical maximum voltage, which assumes ideal conditions. Therefore, the experimental open-circuit voltage of 1.1 V is an acceptable value.

Addressing Cell Cracking During Operation

The planar cells operated as expected on hydrogen, without complications. When humidified gases were introduced into the system, the planar cells cracked, making it necessary to investigate this problem before further data could be collected.

As received from the manufacturer, the planar cells were too wide to fit into the furnace, so 2 cm were trimmed from each side of the cell using a tungsten carbide scoring tool. The initial hypothesis was that the process of trimming the cells created small fractures along the edge of the cell that would worsen during operation. To prevent this issue, the opening of the furnace was widened, making trimming unnecessary. However, this did not prevent the cells from cracking. Based on the results obtained when cell trimming was ceased, the cracking was not due to existing microfractures. Furthermore, the observation that the cracking only occurred when humidified gases were used pointed toward other causes.

Examining the Effects of Gas Flow Configurations

Figure 5.13 shows a crack in Cell #2, corresponding to the cathode inlet area of the manifold. Cell #1 is excluded, as it cracked during the trimming process and was not used. Cell #2 was successfully used to collect voltammetric data with hydrogen as the fuel gas but failed during operation on humidified methane. Cell #2 was operated at 750°C, and the temperature of the humidification flask was kept at 89°C, for a humidification level of 67%. The crack shown in Figure 5.13 occurred while Cell #2 was running on 50 mL/min methane and 500 mL/min air.

Figure 5.13: Crack at the cathode inlet area of Cell #2

Figure 5.14 describes the configuration of gas flow through the Crofer manifolds for Cell #2.

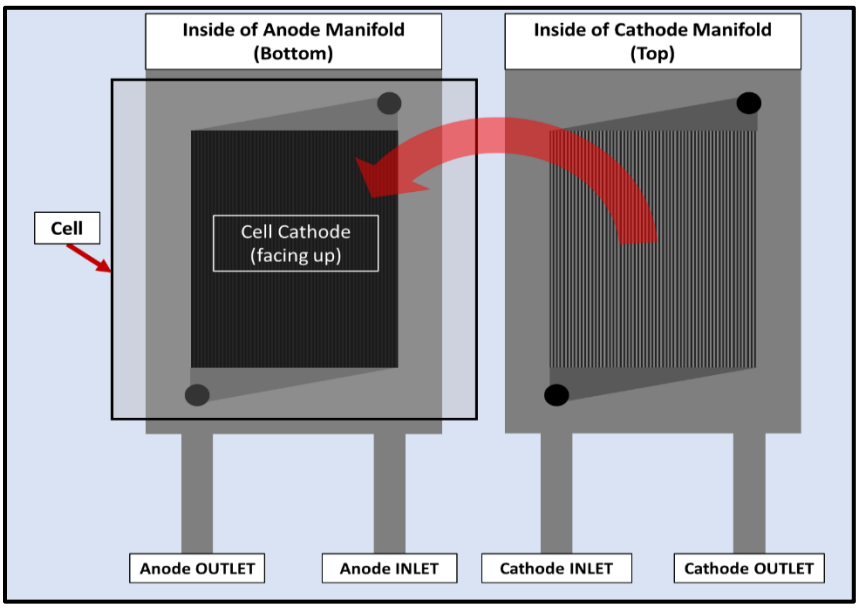

Figure 5.14: Gas flow configuration for Cell #2

In the configuration illustrated in Figure 5.14, the anode gas flows through the length of the Crofer manifold before it reaches the cell, while the cathode gas reaches the cell

without passing through the length of the manifold. In this case, the anode gas has more time to reach the cell temperature of 750°C while the cathode gas (air) enters the cell immediately.

Cell #3, shown in Figure 5.15, suffered a more severe crack than Cell #2, with pieces of the electrolyte apparently blown out. Again, the cell cracked in the region corresponding to the cathode inlet, where air first encounters the cell.

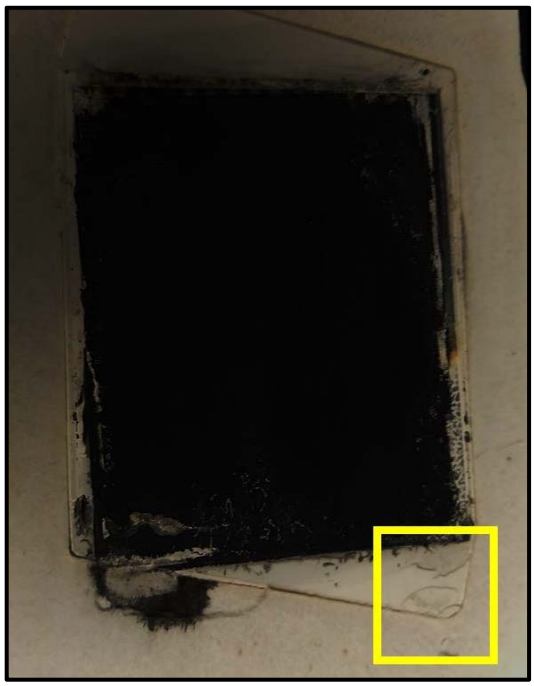

Figure 5.15: Chips in the electrolyte of Cell #3, at cathode inlet

This cell was operated under the same temperature and humidification conditions as the previous cell, but the flow of gases into the Crofer manifold was changed to the configuration shown in Figure 5.16. This cell never saw fuel gas, instead cracking during purging with 100 mL/min of humidified nitrogen and 100 mL/min air.

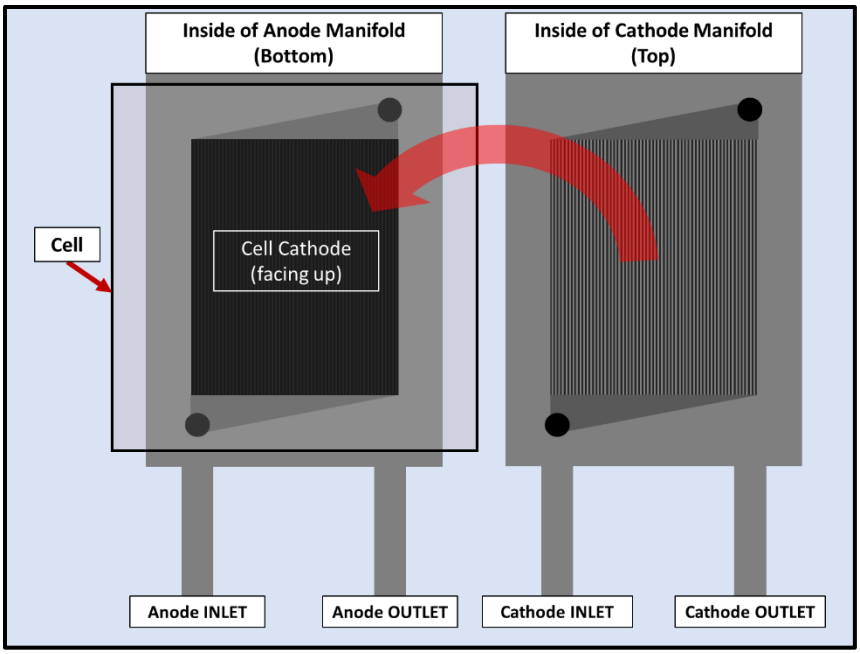

Figure 5.16: Gas flow configuration for Cells #3 and #4

In the configuration shown above, both the anode and cathode gases enter the flow field at the front of the manifold and exit at the back. This same gas flow configuration was used for Cell #4.

Cell #4 was successfully operated on dry hydrogen at mass transport conditions, but later cracked during purging with 100 mL/min of humidified nitrogen and 100 mL/min of air. For this cell, the temperature of the water in the humidification flask was increased to 92°C to ensure carbon deposition is completely avoided, resulting in a water vapor pressure of 567 torr and 75% humidification. Like the previous two cells, Cell #4 cracked in the region corresponding to the cathode inlet, and as with Cell #3, pieces of the electrolyte were blown out. This is shown in Figure 5.17.

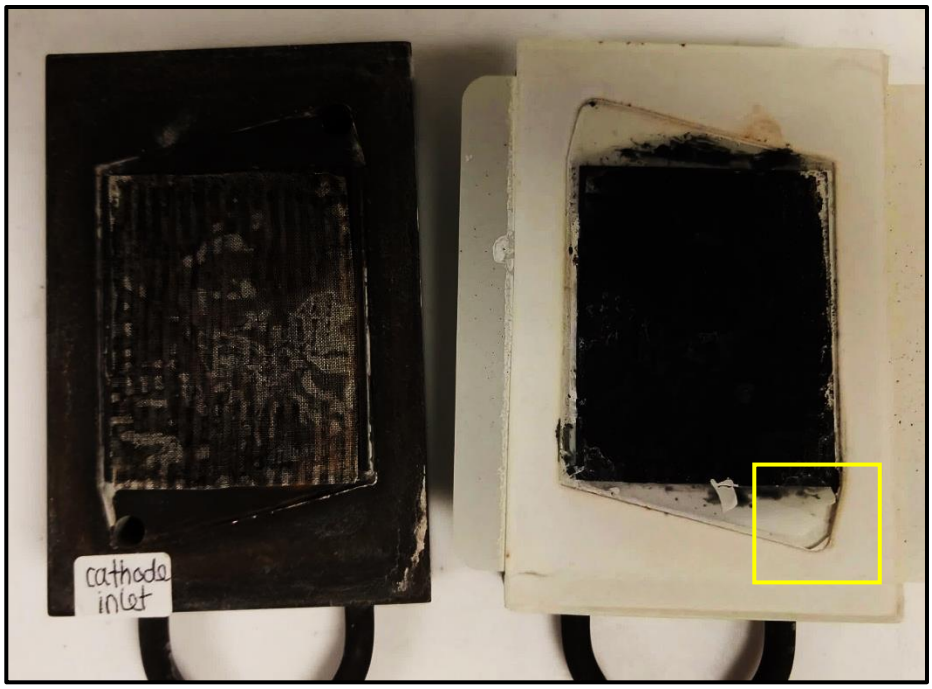

Figure 5.17: Chips in the electrolyte of Cell #4, at cathode inlet

In Cells #2 through #4, the gas flow configurations were varied, but in each case, there was at least one gas that entered the flow field at the front of the manifold. This could potentially mean that the gases did not have enough time to reach the operating cell temperature before encountering the cell itself, creating cool spots on the cell surface. Therefore, these configurations could have led to the cells cracking because of a temperature gradient. To remove this potential cause of cell failure, the gas flow configuration for Cell #5 was altered to the configuration shown in Figure 5.18.

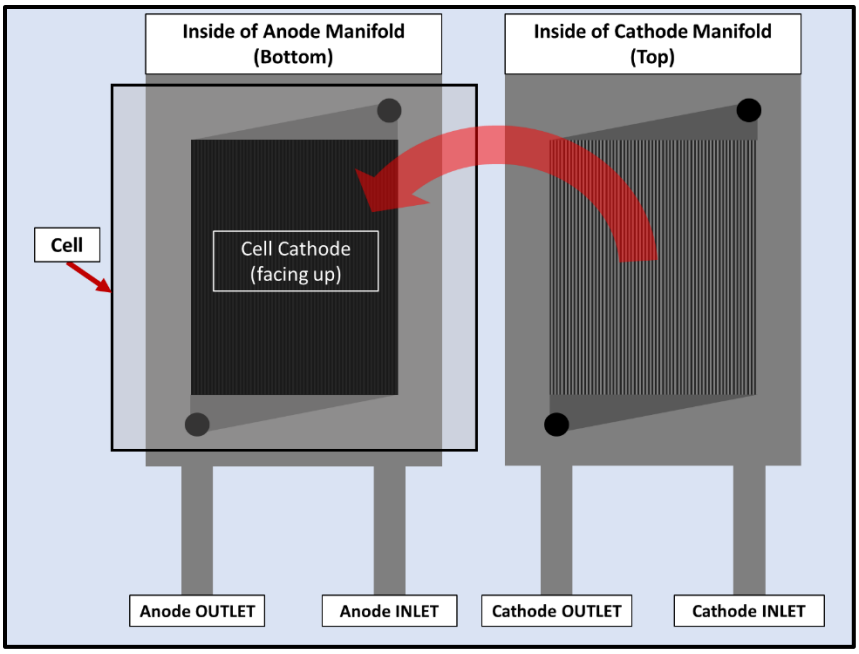

Figure 5.18: Gas flow configuration for Cell #5

In the configuration shown in Figure 5.18, both the anode and cathode gases enter the flow field at the rear of the manifold, meaning they must travel through the inside of the manifold before encountering the cell. This configuration was chosen to allow the gases more time to heat up to the cell's temperature of 750°C rather than potentially reaching the cell while they are at lower temperatures (humidification flask temperature for the anode gas and ambient temperature for the cathode gas). However, this modification failed to prevent the cell from cracking, as shown in Figure 5.19 and Figure 5.20.

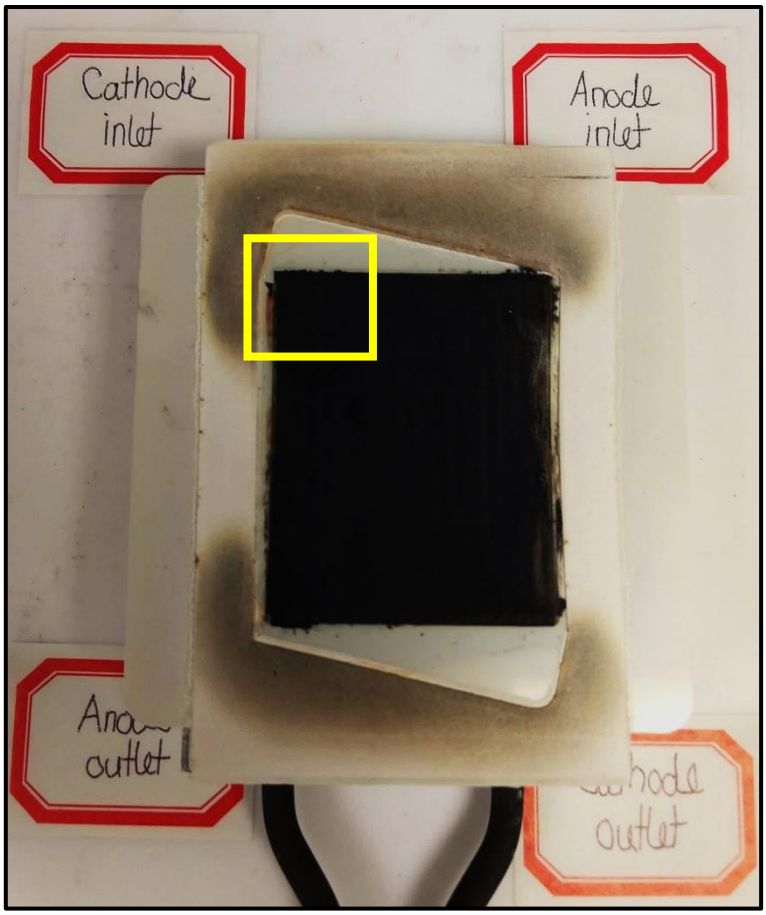

Figure 5.19: A chip and a crack in the electrolyte at the cathode inlet of Cell #5

Figure 5.20: Closeup of the chip/crack in Cell #5

Figure 5.19 and Figure 5.20 show the outcome when Cell #5 was operated under the gas flow configuration shown in Figure 5.18. Cell #5 survived purging with 100 mL/min of humidified nitrogen (humidification flask temperature of 92°C for 75% humidification) and 250 mL/min air, as no leak was detected after this purging process. The cell was then fed 25 mL/min of humidified methane and 250 mL/min of air, and voltage and current readings were monitored to determine that the cell reached a steady operating state. Because the readings fluctuated, the gas flows were increased to 50 mL/min of humidified methane and 500 mL/min of air to stabilize the readings by ensuring the anode was receiving a steady supply of fuel gas. However, the voltage and current readings continued to fluctuate greatly, indicating the presence of a leak in the cell. When consulted, engineers at Fuel Cell Materials confirmed that the gas flow configuration described in Figure 5.18 is the optimal one, so the same configuration was tested again with Cell #6.

Cell #6 was purged with 100 mL/min of humidified nitrogen, again at a humidification flask temperature of 92°C, and 100 mL/min of air. This purging process lasted approximately two hours, during which the rates of the gases exiting through the anode and cathode outlets were monitored. This was done by attaching flexible ¼" tubing to the anode and cathode outlets of the manifold and placing the ends in equal volumes of water to observe bubbling. Initially, the system did not leak; when only the cathode inlet received gas, bubbles were only seen at the cathode outlet, and vice versa. After some time, a leak was apparent, as only the anode outlet experienced bubbling even when both inlets were fed gases. Opening the manifold showed there were no cracks or chips present in Cell #6, as shown in Figure 5.21.

This suggests that the leak was likely due to the alumina felt seals in the manifold failing. These experiments indicated that something other than a temperature gradient due to gas flow was responsible for the cells cracking.

Figure 5.21: Despite a significant leak, there was no cracking in Cell #6.

Examining the Effects of Condensation in the Manifolds

Despite varying the paths that the anode and cathode gases take before encountering the cell, each attempt still resulted in the electrolyte of the cell cracking in the region corresponding to the cathode gas inlet. For each of the cells, the flow of gases coming from the anode and cathode outlets was monitored during the experiment, as described for Cell #6. Until a leak developed, the flow of air from the cathode outlet matched the flow of air into the cathode inlet. The gas flow across the anode side of the cell, on the other hand, was more complicated.

The steady bubbling, matching the set flow rate of anode gas, in the humidification flask indicated there was no leak between the anode gas cylinder and the humidification system. The bubbling at the anode outlet, on the other hand, was irregular. For a short time, there was steady bubbling at the anode outlet. It then tapered off until bubbling at the anode outlet ceased. After some time, a sudden and forceful burst of bubbles appeared at the anode outlet, and the process repeated. These observations suggested that there was a buildup of pressure somewhere in the system.

Furthermore, because the portions of the Crofer manifold protruding from the furnace remained cool to the touch even when the furnace was at 750°C, the condensation of water vapor from the humidified gas was thought to be the cause of this pressure buildup. As the humidified gas flowed out of the humidification flask and into the anode inlet of the Crofer manifold, cool spots along the line could have caused the water vapor in the humidified gas to condense and block the gas flow. This would cause the bubbling rate seen at the anode outlet to slow down and eventually stop until enough gas pressure built up in the line to force the condensation out. In turn, this buildup and sudden release of pressure may have caused the cells to crack or the alumina felt seals to fail. The experimental apparatus shown in Figure 5.11 received several modifications to prevent water condensation.

Originally ¼" Teflon tubing wrapped with heating tape set to 100°C delivered humidified gas from the humidification flask to the anode inlet. This was replaced with ¼" stainless steel tubing wrapped with heating cord set to at least 130°C. Because stainless steel conducts heat better than Teflon and because the heating cord allows for tighter wrapping of the gas tubing than heating tape does, this was expected to prevent

water from condensing in the tubing on its way to the anode inlet. Furthermore, all four sections of the Crofer manifold protruding from the furnace were also wrapped with heating cord, also set to at least 130°C. A thermocouple was used to verify that the temperature of all these components remained above 120°C, which should have prevented water from condensing. Figure 5.22 shows the apparatus described here.

Figure 5.22: Stainless steel tubing and heating cord added to prevent condensation

Cell #7 was set up in the same configuration shown in Figure 5.18. When the cell was purged and leak tested with humidified nitrogen and air, a leak was immediately apparent. When 100 mL/min of air were fed into the cathode inlet, the rate of bubbling at the cathode outlet was much slower. Additionally, even when only the cathode inlet was receiving gas, there was bubbling at the anode outlet. After approximately one hour of purging the cell with 100 mL/min of air into the cathode and 100 mL/min of humidified nitrogen into the anode, a significant leak was noticed because gases were only exiting at

the anode outlet. Disassembling the cell revealed that it did not crack, so the source of the leak was likely the alumina felt seals failing. Figure 5.23 shows Cell #7.

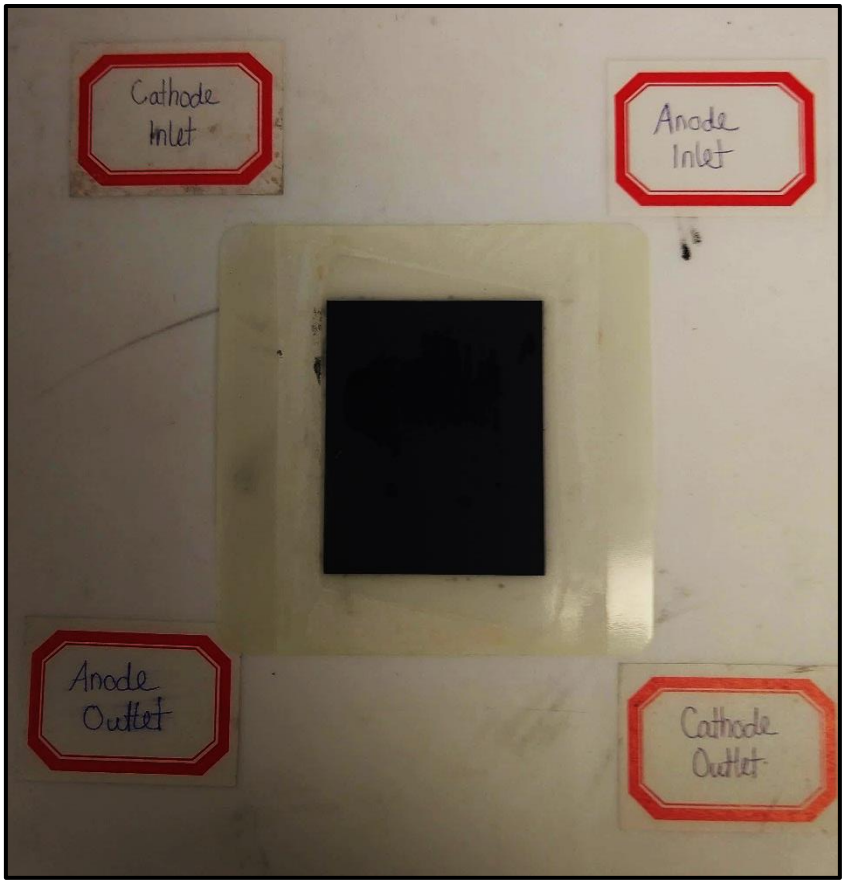

Figure 5.23: Cell #7 did not crack, suggesting that leaks were caused by the alumina felt seals failing.

PART IV: Conclusions

Even with the gas flow configuration suggested by the manufacturer and the modifications made to prevent pressure buildup due to condensation, the planar cells continued leaking when humidified gases were used. Observations about the bubbling rate at the anode outlet still pointed toward a buildup and release of pressure existing somewhere between the exit of the humidification flask and the anode outlet. The strong

potential for cell failure due to cracking or the alumina felt seals failing ultimately made the planar cells a poor choice for any sort of lengthy operation, including the life tests that were planned. Furthermore, at $305 per cell,[48] the planar cells were too expensive to continue troubleshooting. For these reasons, the initial plan of collecting data using planar cells was abandoned in favor of button cells, which were less expensive and did not suffer from the leaking and cracking issues that caused the planar cells to fail.

Future Directions

Time constraints and expenses prevented further research into running planar solid oxide fuel cells on landfill gas, but the project should be continued by future students in the research group. Based on previous attempts, observations, and discussions with the manufacturers, condensation of water vapor is a likely culprit of cell failure. Therefore, more work is needed to identify where the condensation is occurring and how to prevent it. Another source of cell failure was gas leakage through the alumina felt seals, so a different method of sealing the cells in the manifold, such as using Ceramabond in place of or in conjunction with the alumina seals, should be tested. Alternately, if the condensation problem cannot be overcome, it is always possible to externally reform and dehumidify landfill gas prior to feeding it into the cell.

REFERENCES

[1] Höök, M.; Tang, X. Depletion of fossil fuels and anthropogenic climate change – A review. *Energy Policy*. [Online] **2013**, *52*, 797-809. https://doi.org/10.1016/j.enpol.2012.10.046 (accessed Nov 30, 2017).

[2] World Energy Council. *World Energy Resources 2013 Survey* [Online]; London, U.K., 2013. https://www.worldenergy.org/wp-content/uploads/2013/09/ Complete_WER_2013_Survey.pdf (accessed Nov 30, 2017).

[3] Bruckner T.; Bashmakov, I.A.; Mulugetta, Y.; Chum, H.; de la Vega Navarro, A.; Edmonds, J.; Faaij, A.; Fungtammasan, B.; Garg, A.; Hertwich, E.; Honnery, D.; Infield, D.; Kainuma, M.; Khennas, S.; Kim, S.; Nimir, H.B.; Riahi, K.; Strachan, N.; Wiser, R.; and Zhang, X. Energy Systems. In: *Climate Change 2014: Mitigation of Climate Change: Contribution of Working Group III to the Fifth Assessment Report of the Intergovernmental Panel on Climate Change* [Online]; Cambridge University Press: New York, 2014; pp 511-597. https://www.ipcc.ch/pdf/assessment-report/ar5/wg3/ ipcc_wg3_ar5_chapter7.pdf (accessed Nov 30, 2017).

[4] *Monthly Energy Review August 2019* [Online]*;* DOE/EIA-0035(2019/8); U.S. Energy Information Administration, U.S. Department of Energy, U.S. Government Printing Office: Washington, DC, 2019. https://www.eia.gov/totalenergy/data/monthly/ archive/00351908.pdf (accessed Aug 27, 2019).

[5] Shafiee, S.; Topal, E. When will fossil fuel reserves be diminished? *Energy Policy* [Online] **2009**, *37*, 181-189. https://doi.org/10.1016/j.enpol.2008.08.016 (accessed Nov 30, 2017).

[6] NASA. Global Climate Change: Vital Signs of the Planet: Carbon Dioxide. http://climate.nasa.gov/vital-signs/carbon-dioxide (accessed Feb 13, 2020).

[7] [Cubasch, U., Wuebbles, D.; Chen, D.; Facchini, M.C.; Frame, D.; Mahowald, N.; and Winther, J.G. Introduction. In: *Climate Change 2013: The Physical Science Basis. Contribution of Working Group I to the Fifth Assessment Report of the Intergovernmental Panel on Climate Change* [Online]; Cambridge University Press: New York, 2013; pp 119-158. https://www.ipcc.ch/pdf/assessment-report/ar5/wg1/ WG1AR5_Chapter01_FINAL.pdf (accessed Nov 30, 2017).

[8] Duerr, M.; Gair, S.; Cruden, A.; McDonald, J. Hydrogen and electrical energy from organic waste treatment. *Int. J. Hydrogen Energy* [Online] **2007**, *32*, 705-709. https://doi.org/10.1016/j.ijhydene.2006.08.006 (accessed Nov 30, 2017).

[9] *Landfill Gas Energy Project Development Handbook* [Online]; Landfill Methane Outreach Program, U.S. Environmental Protection Agency, U.S. Government Printing Office: Washington, DC, 2017. https://www.epa.gov/sites/production/files/2016-11/documents/pdh_full.pdf (accessed Nov 30, 2017).

[10] *Environmental Quality: Landfill Gas Collection and Treatment Systems: Engineer Manual* [Online]; EM 200-1-22; U.S. Army Corps of Engineers, U.S. Government Printing Office: Washington, DC, 2013. https://www.publications.usace.army.mil/ Portals/76/Publications/ EngineerManuals/EM_200-1-22.pdf?ver=2013-09-05-152155-217 (accessed Nov 30, 2017).

[11] Milewski, J.; Lewandowski, J. Solid oxide fuel cell fuelled by biofuels. *ECS Trans.* [Online] **2009**, *25* (2), 1031-1040. http://ecst.ecsdl.org/content/25/2/1031.full.pdf+html (accessed Nov 30, 2017).

[12] Prakash, B.S.; Kumar, S.S.; Aruna, S.T. Properties and development of Ni/YSZ as an anode material in solid oxide fuel cell: A review. *Renewable Sustainable Energy Rev*. [Online] **2014**, *36*, 149-179. https://doi.org/10.1016/j.rser.2014.04.043 (accessed Nov 30, 2017).

[13] Fuel Cell Materials. NextCell Electrolyte Supported Button Cell. https://fuelcellmaterials.com/products/cells/nextcell-electrolyte-supported-button-cell/ (accessed Nov 30, 2018).

[14] Papurello, D.; Lanzini, A.; Leone, P.; Santarelli, M.; Silvestri, S. Biogas from the organic fraction of municipal solid waste: Dealing with contaminants for a solid oxide fuel cell energy generator. *Waste Manag*. [Online] **2014**, *34* (11), 2047–2056. http://dx.doi.org/10.1016/j.wasman.2014.06.017 (accessed Oct 5, 2018).

[15] Kan, H.; Hyun, S.H.; Shul, Y.G.; Lee, H. Improved solid oxide fuel cell anodes for the direct utilization of methane using Sn-doped Ni/YSZ catalysts. *Catal. Commun.* **2009**, *11*, 180-183. http://dx.doi.org/10.1016/j.catcom.2009.09.021 (accessed Nov 30, 2017).

[16] Mermelstein, J.; Millan, M.; Brandon, N. The impact of steam and current density on carbon formation from biomass gasification tar on Ni/YSZ and NI/CGO solid oxide fuel cell anodes. *J. Power Sources* [Online] **2010**, *195*, 1657-1666. https://doi.org/10.1016/j.jpowsour.2009.09.046 (accessed Nov 30, 2017).

[17] Khan, F. Effect of Hydrogen Sulfide in Landfill Gas on Anode Poisoning of Solid Oxide Fuel Cells. M.S. Thesis, Youngstown State University, Youngstown, OH, May 2012.

[18] *Control of Odorous Gas at Massachusetts Landfills* [Online]; Bureau of Waste Management, Executive Office of Energy and Environmental Affairs, Massachusetts Department of Environmental Protection: Boston, MA, 2007. https://www.mass.gov/ files/ documents/2016/08/sm/lfgaspol.pdf (accessed Aug 19, 2018).

[19] Eastern Research Group. *Background Information Document for Updating AP42 Section 2.4 for Estimating Emissions from Municipal Solid Waste Landfills* [Online]*;* EPA/600/R-08-116; Office of Research and Development, U.S. Environmental Protection Agency, U.S. Government Printing Office: Washington, DC, 2008. https://www3.epa.gov/ttn/chief/ap42/ch02/draft/db02s04.pdf (accessed Aug 19, 2018).

[20] Turco, M.; Ausiello, A.; Micoli, L. *Treatment of Biogas for Feeding High Temperature Fuel Cells: Removal of Harmful Compounds by Adsorption Processes* [Online]; Green Energy and Technology; Springer: Switzerland 2016. https://link.springer.com/content/pdf/10.1007%2F978-3-319-03215-3.pdf (accessed Oct 2, 2018).

[21] Haga, K.; Adachi, S.; Shiratori, Y.; Itoh, K.; Sasaki, K. Poisoning of SOFC anodes by various fuel impurities. *Solid State Ionics* [Online] **2008**, *179*, 1427–1431. https://doi.org/10.1016/j.ssi.2008.02.062 (accessed Oct 5, 2018).

[22] Storey, J. M.; Theiss, T. J.; Kass, M. D.; Finney, C. E. A.; Lewis, S.; Kaul, B. C.; Besmann, T. M.; Thomas, J. F.; Rogers, H.; Sepaniak, M. *Fuel Flexibility: Landfill Gas Contaminant Mitigation for Power Generation* [Online]; ORLN/TM-2014/44; Oak Rifge National Laboratory: Oak Ridge, TN, 2014. https://doi.org/10.2172/1130430 (accessed Nov 26, 2018).

[23] Soreanu, G.; Béland, M.; Falletta, P.; Edmonson, K.; Svoboda, L.; Al-Jamal, M.; Seto, P. Approaches concerning siloxane removal from biogas - A review. *Can. Biosyst. Eng. / Le Genie des Biosyst. au Canada* [Online] **2011**, *53*, 8.1-8.18. http://www.csbe-scgab.ca/docs/journal/53/C0815.pdf (accessed Oct 5, 2018).

[24] Gaj, K. Applicability of selected methods and sorbents to simultaneous removal of siloxanes and other impurities from biogas. *Clean Technol. Environ. Policy* [Online] **2017**, *19* (9), 2181–2189. https://doi.org/10.1007/s10098-017-1422-1 (accessed Oct 5, 2018).

[25] Sigot, L.; Ducom, G.; Benadda, B.; Labouré, C. Adsorption of octamethylcyclotetrasiloxane on silica gel for biogas purification. *Fuel* [Online] **2014**, *135*, 205–209. https://doi.org/10.1016/j.fuel.2014.06.058 (accessed Oct 5, 2018).

[26] *Landfill Gas Energy Project Data: Currently Opperational Projects.* Landfill Methane Outreach Program, U.S. Environmental Protection Agency, July 2019 [Online]. https://www.epa.gov/sites/production/files/2019-07/opprjslmopdata-detailed.xlsx (accessed Oct 24, 2019).

[27] Renewable Energy. *City of Oberlin Climate Action Plan 2019* [Online]. City of Oberlin Climate Action Committee: Oberlin, OH, September 2019. https://www.cityofoberlin.com/wp-content/uploads/2019/09/2019-Climate-Action-Plan-Update.pdf (accessed Oct 24, 2019).

[28] *High Temperature Ceramic & Graphite Adhesives* [Online]. Technical Bulletin A2; Aremco Products, Inc.: Valley Cottage, NY, April 2015. https://www.aremco.com/wp-content/uploads/2015/04/A02_15.pdf (accessed Dec 2, 2017).

[29] *ProboStat™ Manual: Version A-6* [Online]; Norwegian Electro Ceramics AS: Oslo, Norway, January 2007. http://www.norecs.com/index.php?page=Manuals (accessed Dec 2, 2017).

[30] Lemmon, E.W.; McLinden, M.O.; and Friend, D.G. Thermophysical Properties of Fluid Systems. In *NIST Chemistry WebBook, NIST Standard Reference Database Number 69* [Online]; Linstrom, P.J., Mallard, W.G., Eds.; National Institute of Standards and Technology: Gaithersburg, MD, 2017. https://webbook.nist.gov/chemistry/fluid/ (accessed Aug 20, 2018).

[31] Pierce, J. L. Siloxane sampling, analysis and data reporting recommendations on standardization for the biogas utilization industry. Presented at the 14th Annual EPA LMOP Conference, Baltimore, MD, Jan 18-20, 2011. https://www.epa.gov/sites/ production/files/2016-06/documents/pierce.pdf (accessed Oct 5, 2018).

[32] National Center for Biotechnology Information. PubChem Compound Database. CID=10913 https://pubchem.ncbi.nlm.nih.gov/compound/ decamethylcyclopentasiloxane#section=Top (accessed Oct 20, 2018).

[33] Youngstown State University. Single Crystal X-Ray Diffractometers. https://ysu.edu/academics/science-technology-engineering-mathematics/facilities/chemistry-facilities/single-crystal (accesed Dec 14, 2019).

[34] *Gas Detection Tubes and Sampling Handbook,* 2nd ed [Online]; RAE Systems, Inc., 2013. https://www.raesystems.com/sites/default/files/content/resources/eBook-gas-detection-tube-and-sampling-handbook.pdf (accessed Feb 2, 2018).

[35] Youngstown State University. Electron Microscopes. https://ysu.edu/academics/science-technology-engineering-mathematics/facilities/chemistry-facilities/electron-microscopes (accessed Dec 4, 2018).

[36] Youngstown State University. S2 Ranger. https://ysu.edu/academics/science-technology-engineering-mathematics/facilities/chemistry-facilities/S2-ranger (accessed Feb 6, 2020).

[37] Pistorius, C.W.F.T.; Sharp, W.E. Properties of water. Part VI. Entropy and Gibbs free energy of water in the range 10–1000°C and 1–250,000 bars. *Amer. J. Sci.* [Online] **1960**, *258*, 757-768. https://htracyhall.org/ocr/HTH-Archives/ Cabinet%208/Drawer%204%20(MP- OL)/ (Pistorius,%20C.W.F.T.)%20(linked)/(Pistorius,%20C.W.F.T.)-594_OCR.pdf (accessed Feb 28, 2018).

[38] *Proceedings of the Conference on High Temperature Solid Oxide Electrolytes Aug 16-17, 1983: Volume I – Anion Conductors*; BNL-51728; Brookhaven National Laboratory: Upton, NY, 1983.

[39] Huang, X.; Zhang, Z.; Jiang, J. Fuel cell technology for distributed generation: an overview. In *IEEE ISIE Conference* [Online], Proceedings of the International Symposium on Industrial Electronics, Montréal, Canada, July 9 – 12, 2006. https://doi.org/10.1109/ISIE.2006.295713 (accessed Feb 16, 2018).

[40] *Spectral Database for Organic Compounds*; National Institute of Advanced Industrial Science and Technology: Tokyo, JP, 1999; SDBS-IR-NIDA-39730 (IR spectrum of decamethylcyclopentasiloxane). https://sdbs.db.aist.go.jp/sdbs/cgi-bin/landingpage?spcode=IR-NIDA-39730 (accessed Feb 2, 2019).

[41] Hepburn, C.A.; Vale, P.; Brown, A.S.; Simms, N.J.; Mcadam, E.J. Development of on-line FTIR spectroscopy for siloxane detection in biogas to enhance carbon contactor management. *Talanta* [Online] **2015**, *141*, 128–136. https://doi.org/10.1016/j.talanta.2015.03.063 (accessed Feb 4, 2019).

[42] *Nickel Oxide – YSZ*; MSDS No. NT-009 [Online]; Nexceris, LLC: Lewis Center, OH, Oct 1, 2015. https://fuelcellmaterials.com/wp-content/uploads/2015/12/NiYSZ-US.SDS_.pdf (accessed June 3, 2019).

[43] NextCell; MSDS No. NT-014 [Online]; Nexceris, LLC: Lewis Center, OH, Nov 13, 2015. https://fuelcellmaterials.com/wp-content/uploads/2016/01/NextCell.SDS_.pdf (accessed June 3, 2019).

[44] Ceramabond 552; MSDS [Online] Aremco Products, Inc.: Valley cottage, NY, 2012. http://graphitestore.com/core/media/media.nl?id=9433&c=4343521&h=1ac14cf697a87c57859a (accessed Feb 12, 2020)

[45] *28 cm^2 Test Fixture Manual* [Online]*;* Fuel Cell Materials: Lewis Center, OH, 2007. https://fuelcellmaterials.com/wp-content/uploads/28-cm2-cell-kit-instructions.pdf (accessed Nov 10, 2017).

[46] Janardhanan, V. Internal reforming of biogas in SOFC: A model based investigation. *J. Solid State Electrochem.* [Online] **2015**, *19*, 2981-2990. https://doi.org/10.1007/s10008-015-2909-5 (accessed Feb 16, 2018).

[47] Tuyen, N.D.; Fujita, G. Modelling a SOFC Power Unit Using Natural Gas Fed Directly. In *Advances in Natural Gas Technology* [Online]; Al-Megren, H., Ed.; InTech: Rijeka, Croatia, 2012; pp 497-524. https://doi.org/10.5772/36376 (accessed Feb 16, 2018).

[48] Fuel Cell Materials. NextCell Electrolyte Supported Planar Cell. https://fuelcellmaterials.com/products/cells/nextcell-electrolyte-supported-planar-cell/ (accessed Dec 14, 2018).